Developing Self-Catalysed GaAsP Nanowires on Silicon Substrates for High-Efficiency Solar Cells

Yunyan Zhang

A thesis submitted to University College London for the degree of Doctor of Philosophy.

Department of Electronic and Electrical Engineering,

University College London

June 2015

Dedication

To:

My family for giving me love, support, and encouragement.

Acknowledgments

During my PhD study, I got great help and support from a lot of people. I would like to express my sincere appreciation to them.

First, I would like to thank my supervisor Prof. Huiyun Liu, who gives me instructions on research in my study period with his well-disciplined attitude. At the same time, he is a good friend in my life, who helps me to overcome the defects in my personalities and gives me suggestions on my everyday life, with great patience and concern. Along with Huiyun, I also need to thank my second supervisor Dr Martin Aagesen, who gave me a lot of instructions. He is a nanowire expert with extensive knowledge, and always offers me practical suggestions on my experiment. During the study, I also get a lot help from my colleagues, Mr Kevin Lee, Dr Jiang Wu, Dr Sabina Hatch, Dr Qi Jiang, Dr Siming Chen, Mr Phu Lam, Mr Mingchu Tang, Miss Pamela Jurczak, Mr Dongyoung Kim and Mr Arthur Onno. They helped me to get used to the new environment when I first got here. During these years, they also offered great patience to discuss with me about my research and provide me sincere friendship to overcome the sadness, frustration and homesickness that sometimes attacked me. For the research, I would also like to show my appreciation to all the technicians and all the cooperating groups. They facilitate and quicken my research by providing various help, such as Suguo Huo for SEM (London Centre for Nanotechnology, University College London), Ana M. Sanchez, Richard Beanland, Thomas Ward, (Department of Physics, University of Warwick) Stephanie K Haywood, Sarfraz Ali (University of Hull) for TEM and Xiulai Xu (Institute of Physics Chinese Academy of Sciences), David Mowbray, Jon Orchard (The Univ. of Sheffield) for optical measurement. My appreciation also needs to be given to some other

people, such as Professor R. R. LaPierre (Department of Engineering Physics, Centre for Emerging Device Technologies, McMaster University), Professor Erik Garnett (FOM Institute AMOLF), and Professor Anna Fontcuberta i Morral (Ecole Polytechnique Fédérale de Lausanne). They offered me kind help and suggestions to understanding some difficult theories, which greatly facilitated my research.

Contents

List of Papers, Patent and Conference Talks

Papers:

"Self-Catalyzed GaAsP Nanowires Grown on Silicon Substrates by Solid-Source Molecular Beam Epitaxy", **Zhang Y**, Aagesen M, Holm J V, Jørgensen H I, Wu J, and Liu H 2013 Nano Letters 13 3897

"Self-Catalyzed Ternary Core–Shell GaAsP Nanowire Arrays Grown on Patterned Si Substrates by Molecular Beam Epitaxy", **Zhang Y**, Wu J, Aagesen M, Holm J, Hatch S, Tang M, Huo S, and Liu H 2014 Nano Letters 14 4542

"Polarity-Driven Quasi-3-Fold Composition Symmetry of Self-Catalyzed III-V-V Ternary Core-Shell Nanowires", **Zhang Y**, Sanchez A M, Wu J, Aagesen M, Holm J V, Beanland R, Ward T, and Liu H 2015 Nano Letters 15 3128

"III-V Nanowires and Nanowire Optoelectronic Devices", **Zhang Y**, Wu J, Aagesen M, Liu H 2015 Topical review invited by Journal of Physics D: Applied Physics 48 463001

"Wafer-scale fabrication of self-catalyzed 17 eV GaAsP core–shell nanowire photocathode on silicon substrates", Wu J, Li Y, Kubota J, Domen K, Aagesen M, Ward T, Sanchez A, Beanland R, **Zhang Y,** Tang M Hatch S, Seeds A, Liu H 2014 Nano Letters 14 2013

"InAs/GaAs quantum dot lasers monolithically grown on Si, Ge, and Ge-on-Si substrates

(Invited)", Lee A D, Jiang Q, Tang M, **Zhang Y,** Seeds A J, Liu H 2013 IEEE Journal of Selected Topics in Quantum Electronics 19 1901107

Conference Talks:

1 Self-catalysed GaAsP nanowires (NW) and solar cells Grown on Si(111) by Solid-Source MBE, **Zhang Y**, Aagesen M, Holm J V, Jørgensen H I, Wu J, and Liu H 2013, UK Semiconductors, Sheffield (UK),

2 Self-catalysed GaAsP nanowires (NW) and solar cells, **Zhang Y**, Aagesen M, Holm J V, Jørgensen H I, Wu J, and Liu H, 2013, The Defence Science and Technology Laboratory (Dstl) conference, UCL (UK, London),

3 High-efficiency Solar Cells fabricated by Self-catalyzed GaAsP Nanowires, **Zhang Y**, Aagesen M, Holm J V, Jørgensen H I, Wu J, and Liu H, 2014, Quantum Dot Day, Sheffield (UK)

4 Self-Catalyzed GaAsP Nanowires (NW) and Solar Cells by Solid-Source Molecular Beam Epitaxy, **Zhang Y**, Aagesen M, Holm J V, Jørgensen H I, Wu J, and Liu H, 2014, Compound Semiconductor Week, Montpellier (**France)**

5 Research of Ternary GaAsP NW Growth and Its Application in High-Efficiency Solar Cells , **Zhang Y**, Aagesen M, Holm J V, Jørgensen H I, Wu J, and Liu H, 2014, Semiconductor and Integrated Optoelectronics, Cardiff (UK Wales)

6 Self-Catalyzed Ternary Core-Shell GaAsP Nanowires Grown on Patterned and Unpatterned Silicon Substrates by Molecular Beam Epitaxy, **Zhang Y**, Wu J, Aagesen M, Holm J, Hatch S, Tang M, Huo S, and Liu H, 2014, UK Semiconductors, Sheffield (UK),

7 Self-Catalyzed High-Quality GaAsP Nanowires Grown on Patterned and Un-Patterned Si Substrates, **Zhang Y**, Wu J, Aagesen M, Holm J, Hatch S, Tang M, Huo S, and Liu H, 2014, Nanowire Workshop, Eindhoven (**Holland**)

8 Growth Mechanisms of Self Catalyzed High-Quality Core-Shell Nanowires on Si Substrates, **Zhang Y**, Wu J, Aagesen M, Holm J, Hatch S, Tang M, Huo S, and Liu H, 2015, Semiconductor and Integrated OptoElectronics (SIOE), Cardiff (UK Wales)

9 Polarity-Driven Quasi-3-Fold Composition Symmetry for Novel Nanowire Structure design, **Zhang Y**, Sanchez A M, Wu J, Aagesen M, Holm J V, Beanland R, Ward T, and Liu H 2015, UK Semiconductors, Sheffield (UK)

10 Growth and applications of self-catalyzed high-quality core-shell GaAsP nanowires on patterned and unpatterned Si, **Zhang Y**, Wu J, Aagesen M, and Liu H 2016 SPIE OPTO San Francisco, California United States (accepted)

Abstract

GaAsP nanowires (NWs), with a bandgap that can cover wavelengths ranging from green (550 nm) to near infrared (860 nm), are highly promising for photovoltaics (PVs). Moreover, their special nano−scale one−dimensional columnar structure can provide the PV devices with significantly enhanced light−matter interactions, enlarged absorption cross-section, good antireflection, superior light trapping, and efficient charge separation and carrier collection. Due to these advantages, GaAsP NW PV devices can achieve high efficiency but only need a small amount of expensive III-V materials compared with the thin film devices. Thus, a self-catalyzed GaAsP NWs growth technique has been developed, with an aim to achieve high-quality core-shell NWs for solar cells.

In this thesis, research on self-catalyzed GaAsP NWs was carried out first on un-patterned Si substrates. The nucleation differences between As and P in the NW growth were studied and P showed much stronger nucleation ability compared with that of As. To achieve the GaAsP NW growth, the influence of the V/III flux ratio, growth rate and growth temperature were investigated. Despite the small temperature window, GaAsP NWs with good morphology and crystal quality have been achieved over a large growth rate range by adjusting the V/III flux ratio. The P content of these NWs can be adjusted between 10% and 75%. Moreover, the study of the NW doping indicated that Be can build up the concentration in the droplet, which can change the droplet surface energy and lead to sidewall wetting of the droplets. After the NW growth, a fast temperature decrease during the droplet consumption was found to be beneficial to achieving good tip morphology. In addition, the uniformity control was studied by changing the chemical potential of the vapour phase. A length deviation ranging

from 5% to 22% has been demonstrated.

The GaAsP shell growth on the core NWs was then investigated. A slow shell growth rate was found to be beneficial to achieving good shell morphology due to sufficient adatom diffusion. In addition, the study of the ternary shell found, for the first time in the world, a quasi-3-fold compositional symmetry in the cross section of the core-shell GaAsP NWs. This phenomenon is believed to be related to the sidewall surface chemical potential and polarity-related adatom bonding energies. To passivate their surface, the core-shell GaAsP NWs were covered with a thin layer of InGaP. A four-time enhancement in PL intensity has been demonstrated, when compared with the un-passivated ones.

Based on all the results obtained from the un-patterned growth, research was further carried out on patterned Si substrates. The presence of Si oxide inside the patterned holes was found to be the reason that caused long-term low-yield and low-repeatability issue in the patterned growth. In order to remove the oxide, a high-temperature deoxidization step was introduced, which was shown to be very effective. However, the large nucleation area in the holes caused by the high-temperature cleaning can suppress the formation of the catalyst droplets. Therefore, a Ga pre-deposition step was used to assist the droplet formation. With these two techniques, the patterned NW growth achieved high yield and repeatability. The influence of the droplet size on the NW morphology was also studied. The results suggest that the catalyst droplet size should not be smaller than the patterned hole size, otherwise it will affect the NW growth due to the parasitic VS growth at the bottom of the NWs. Following the core growth, a lattice-matched high-quality shell was grown and demonstrated room-temperature PL emission.

The research in this thesis covers some important aspects of NWs. The knowledge of the influence of V/III flux ratio, growth rate and temperature on the NWs is crucial for growing high-quality NWs. Understanding the nucleation differences between As and P is very helpful for the compositional tuning and hence the bandgap control of the GaAsP NWs. The discoveries of novel phenomena about NW doping, droplet consumption, and shell growth are important for the construction of advanced NW device structures. Especially, the theory about the appearance of the quasi-3-fold compositional symmetry in the NW shell growth opens a new way to building a more detailed structure inside the NWs, which is different from the axial and core-shell junction growths. The successful solution to the long-term low-yield and low-repeatability issue of growing NWs on patterned Si substrates can achieve high-level NW growth control and greatly facilitate the device design and fabrication.

Chapter 1:

Introduction

1.1 Nanowires and their Basic Structure Features

In the epitaxy of thin film semiconductor materials, it is required that the substrates have small or even no lattice and thermal expansion coefficient mismatch relative to the epitaxial layers. This significantly limits material integration and hence device structure design. In 1964, Ellis and Wagner presented a brand-new 1-dimensional (1D) structure: "silicon nanowhiskers".[1] This column-shaped structure was called "nanowire" (NW) later on and opened a new world in the material science. It possesses several new features compared with traditional structures.[2-5] Many limitations of traditional material science can be solved with the help of this 1D structure, therefore it has gained great attention. [6-8]

The NWs have a columnar shape with diameter ranging from several to hundreds of nanometres. As demonstrated by Yang *et al*.[9], InSb NWs with a diameter as small as 4.5nm can be achieved. Yao *et al*.[10] reported that their GaAs NWs can be thicker than 300 nm. In contrast, the length of NWs can be as long as tens of micrometres. Avit *et al*.[11] showed that

their GaN NWs can be longer than 60 μm. Ramdani *et al.*[12] even achieved GaAs NWs with a length as long as 130 μm. Therefore, NWs allow carriers, photons and phonons to propagate freely along the NW axis, but confine them in radial directions. For NWs with a sufficiently small diameter, carriers inside are subject to quantum confinement effects. As demonstrated by Gudiksen *et al*.,[13] the bandgap of InP NWs shifted to a higher value when the NW diameter was smaller than 30 nm (Fig. 1-1). Koblmüller *et al*. also reported similar results in their InAs NWs measurement (Fig. 1-2).[14] As illustrated in Figure 1-3, the 2D confinement results in these small-sized 1D NWs having different density of states compared with the 3D (bulk), 2D (quantum well) and 0D (quantum dot) structures.[15]

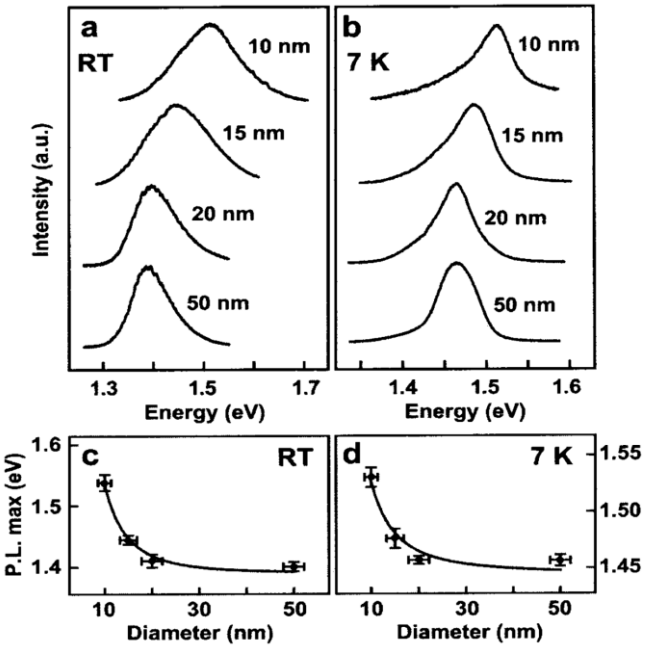

Figure 1-1. (a) (b) Single InP NW PL spectra and (c) (d) peak emission energy change along with the diameter. (a) (c) were measured at room temperature; while (b) (d) at 7 K. Reprinted with permission from Ref. 13. Copyright 2002 American Chemical Society.

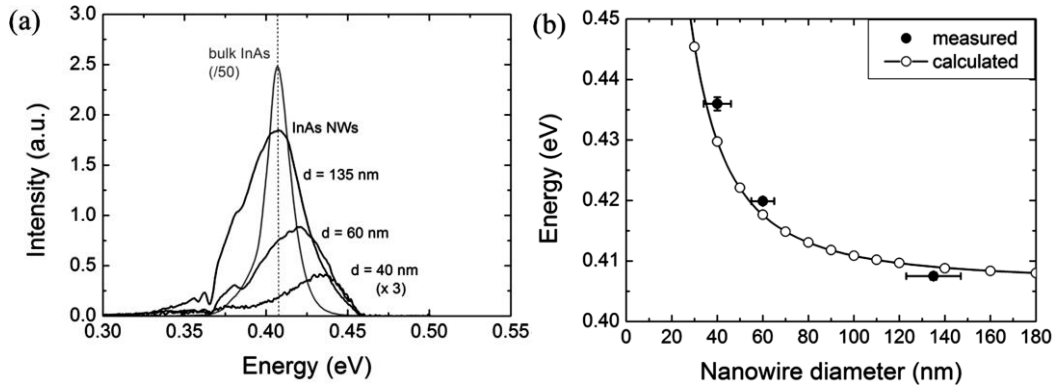

Figure 1-2. (a) PL spectra and (b) the peak emission energy change along with the InAs NW diameter. Reprinted with permission from Ref.14. Copyright 2012, AIP Publishing LLC.

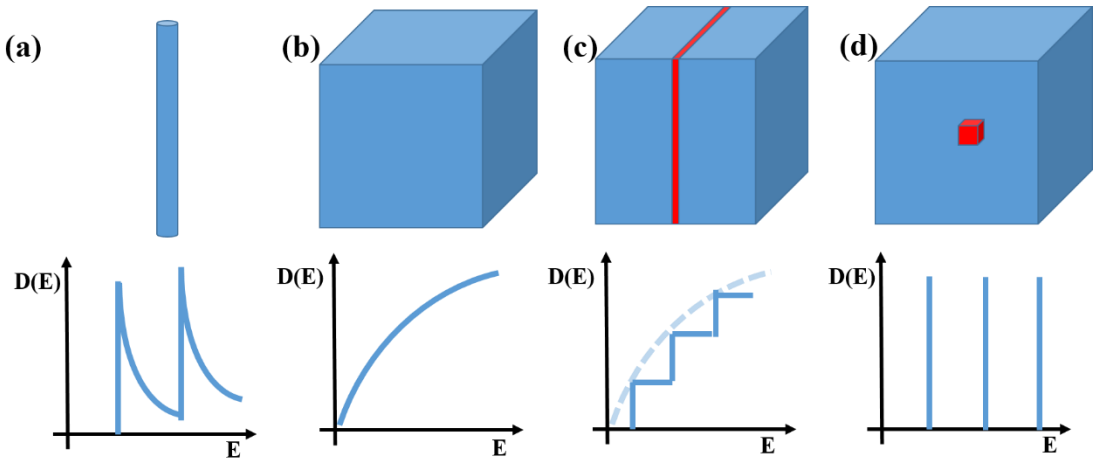

Figure 1-3. Density of states in semiconductors of (a) 1D (NW), (b) bulk (3D), (c) 2D (quantum well) and (d) 0D (quantum dot).[15]

1.2 Advantages and Disadvantages of III-V Nanowires

In the form of the NW structure, III-V materials can possess different properties compared with their thin film counterparts and can overcome a large number of limitations in the traditional thin film technology.[16,17]

Using the NW structure can facilitate material integration and increase substrate choice. Due to their small diameter, the interface between the NW and its substrate is small, which is

beneficial for strain relaxation. Materials with large lattice and thermal expansion coefficient mismatch can therefore be integrated. For example, Yoshimura *et al.*[18] reported that 90 nm InGaAs NWs, with a lattice mismatch of 2.1% relative to the GaAs substrate, can be grown without defects. But if the strain is large, the NW/substrate interface will introduce misfit dislocations to release the strain.[19] For example, misfit dislocations with a period of ~2.9 nm (Fig.1-4) and ~8.0 nm have been observed at the InAs/Si[20] (lattice mismatch 11.6%) and GaAs/Si[21] (4.1%) interfaces, respectively. However, even with the presence of the misfit dislocations, threading dislocations are not observed in most cases (Fig.1-4). This could be due to the layer-by-layer NW growth mode.[22] Therefore, the defects are confined at the NW/substrate interface, which can avoid degrading the performance of NWs. Therefore, III-V materials can be combined with non-III-V substrates to complement each other's advantages and circumvent their shortcomings.[23-25] For example, the integration between the III–V materials and the Si platform has been researched for more than 40 years.[26-29] III-V materials are expensive, but have a direct band-gap, high absorption coefficient, good carrier mobility and large solar spectrum coverage.[30] On the other hand, the Si platform is mature and cost-effective, but does not have good photonic properties due to its indirect bandgap. This integration would help to develop novel optoelectronics devices, such as high-performance silicon-based III-V lasers[31-34] and high-efficiency but cost-effective SCs.[35,36] In addition, the NWs can solve the antiphase domain issue for the III-V growth on non-polar substrates.[37] Therefore, the NWs technique is a new method for widening substrate choice. Apart from the single crystalline and polycrystalline[38] substrates, NW growths have also been demonstrated on graphene[39,40], carbon nanotube,[41] fiber-textured silicon thin film[42] and amorphous Si[43].

Some scientists even reported that glass[44] and indium tin oxide[45] could also be used to grow NWs. This can bring a revolution to the traditional techniques for epitaxy of semiconductors which require crystal substrates to provide lattice template. Therefore, III-V materials can be grown on a much wider variety of substrates, so that the devices can meet different kinds of requirements, such as transparency, flexibility and robustness. The ubiquity of NW devices can thus be greatly enlarged, for example by integrating NW solar cells (SCs) to buildings and fabric.

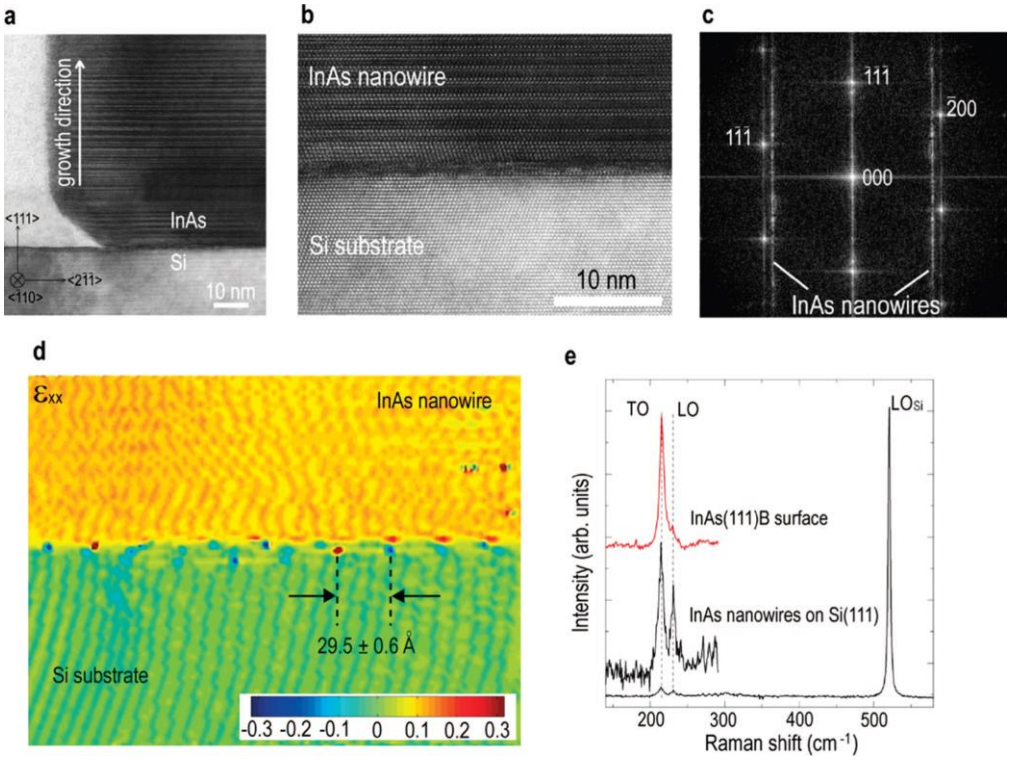

Figure 1-4. (a) and (b) TEM images of the interface between a InAs NW and Si substrate. (c) Fast Fourier transformation (FFT) pattern from (b). (d) ε_{xx} strain mapping of (b). (e) Raman spectra of InAs NW and substrate. Reprinted (adapted) with permission from Ref. 20. Copyright 2008 American Chemical Society.

Apart from the NW/substrate heterojunction, the NW structure is also beneficial for

fabricating axial NW heterojunctions. The small cross-section of NWs can distribute the strain across heterojunction interfaces,[46,47] which makes NWs highly efficient in relaxing the mismatch strain. For example, it was reported that InAs/InP and InAs/InSb heterojunctions can quickly and elastically relax the strain within a thickness of a few nanometres across the junctions. It was predicted that the axial heterojunction of NWs, depending on the lattice mismatch, has a critical diameter below which it can be dislocation-free despite the NW length,[48,49] which has been widely demonstrated, for instance in GaAs/GaP axial heterojunctions.[50] Only when the strain is large, such as for GaAs/GaSb and InAs/InSb heterojunctions,[51] the heterojunction will introduce misfit defects to release the strain. Due to these advantages, axial NW junctions with various material combinations have been demonstrated, such as GaAs/GaAsP,[52] InAs/InSb,[53] InAs/InSb,[54] and GaAs/GaAsSb[55]. The combinations can even cross different material systems, such as GaAs/Ge,[56] GaP/Si,[57] GaN/ZnO[58]. Compared with thin film structures, axial junctions of NWs have more freedom in band structure engineering and device structure design. For example, the growth of traditional Stranski–Krastanow QDs needs the assistance of strain,[59,60] while in the NW structure, QDs can be formed by simply stacking materials axially. This strain-free QD growth mode allows fabricating dots by using lattice-matched materials, which can significantly widen material choices for QDs. In addition, in the QD-in-NW structure, it is much easier to access each dot separately, which is beneficial for single dot research and application.

Lateral core-shell heterojunction NWs can also benefit from their columnar shape and small size. NWs have non-planar side facets, which is beneficial for relaxing strain elastically.

In addition, due to its small size, the core of NWs can share part of the strain with the shell, which can further reduce the strain in the shell.[61-64] For example, Skold *et al*.[65] covered the GaAs core NW with a GaInP shell. By changing the thickness and composition of the shell, they found that the strain can shift the energy bandgap of the core by up to 240 meV (Fig. 1-5a). Montazeri *et al*.[66] also reported similar results. They grew a 25-nm-thick GaP shell on GaAs core NWs and shifted the free exciton emission energy of the core by 260 meV (Fig. 1-5b). Therefore, the NW shell is superior in handling the strain compared with thin film structures. Depending on the lattice mismatch, there is a critical core radius, up to which the shell growth can be free from misfit defects, independently of the shell thickness.[67,68] If the core exceeds the critical radius, there exists a critical shell thickness, below which the shell can be defect-free.[67,68] Due to efficient strain relaxation ability, this critical shell thickness is much larger compared with that in the thin film growth. For example, Nazarenko *et al*.[69] grew GaAs/$In_{0.2}Ga_{0.8}As$ core/shell heterojunctions (lattice mismatch 2%) and found that their 160-nm shell can be defect-free. This is much thicker than their thin film counterpart with a critical thickness of only 10 nm. Similarly to thin film structures, QDs can be grown on the surface of the NWs through the strain-assisted Stranski-Krastanov mode.[70] However, because of the better relaxation ability, the thickness of the wetting layer for the QD formation is much thicker on NWs compared with that on planar substrates.[71,72] It was reported that InAs[73] and InGaAs[74] QD growths have been achieved on the {112} surfaces of NWs. For the {110} facets, the QD formation is not energetically favourable,[75,76] and some surface treatment technique is needed to solve this issue. For example, InAs QDs can be grown on {110} facets of GaAs NWs if the surface of the facets is covered with a thin layer of AlAs.[77]

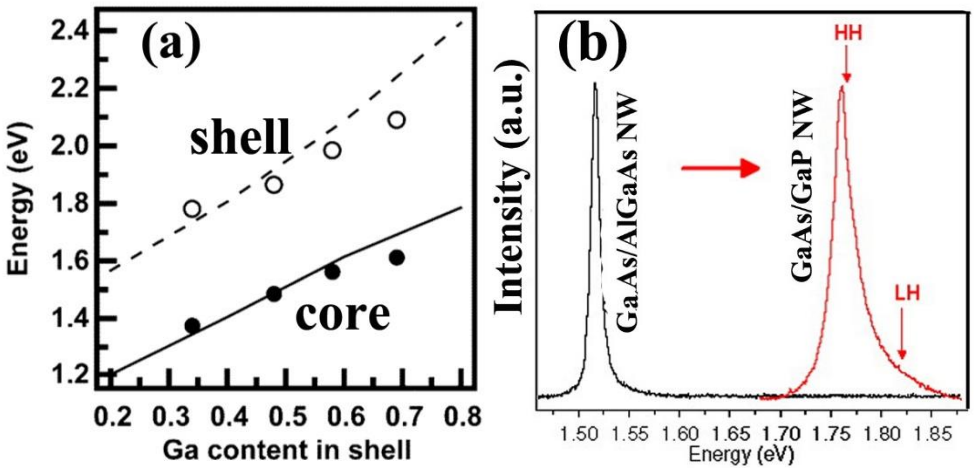

Figure 1-5. (a) Bandgap change of GaAs core and GaInP shell as a function of the Ga content in the shell. Reprinted with permission from Ref. 65. Copyright 2005 American Chemical Society. (b) PL spectrum shift of GaAs core NWs by changing the shell from AlGaAs to GaP. Reprinted with permission from Ref. 66. Copyright 2010 American Chemical Society.

Apart from heterojunctions, the NWs provide a novel method for band structure engineering. In the III-V NW growth, NWs can have zinc blende (ZB) or wurtzite (WZ) structure depending on the growth conditions. This is in stark contrast to the thin film growth, in which the nitrides have WZ structure while other III-V materials exhibit ZB phase. The band structure of the WZ and ZB phases are different. For example, it was reported that the energy bandgap of GaP can change from indirect to direct if its crystal structure is switched from ZB to WZ.[78] The band structure differences can change the photonic and electrical properties of NWs.[79] For example, the optical polarization in ZB structure is parallel to the NW axis, while it is perpendicular in WZ phase.[80,81] This feature is promising for fabricating polarization-sensitive photodectectors.[82] In most cases, the band alignment between the WZ and ZB phases is a type II structure, which can be used to fabricate phase QDs.[83-87] Moreover,

the stacking of WZ and ZB phases in NWs can cause spatial separation of electrons and holes, which could elongate the hot carrier lifetime. For example, it has been demonstrated that stacking faults can rapidly quench the direct-bandgap PL emission,[88] but the lifetime of the indirect-bandgap PL emission[89] and the electrical conductivity[88] are much longer. This could be beneficial to photovoltaic applications. On the other hand, stacking faults are adverse for electronic applications, because it can act as scattering centres for carriers and degrade device performance.[90-94] Parkinson *et al*.[95] reported that carrier mobility in their GaAs NWs could be decreased from 2250±70 to 1200 $cm^2/(Vs)$ by increasing the defect density. Moreover, the stack of ZB/WZ segments can act as traps for the electrons. As reported by Wallentin *et al*.,[96] the undoped InP NWs can trap electrons with a concentration as high as 4.6×10^{18} cm^{-3}, causing low conductivities and mobilities.

1.3 Fabrication Mode Development of III-V Nanowires

NWs fabrication methods can be divided into two main groups, namely top-down and bottom-up approach.

In the top-down fabrication, NWs are etched out of mask-covered bulk materials (Fig. 1-6).[97] The bulk materials can be III-V substrates on which some planar structures can be grown if necessary. Therefore, the well-established and optimized thin film epitaxy technique can be combined with the NW fabrication, which can help to avoid stacking faults and guarantee good NW/substrate interface quality. These attract great attention to the development of etched NWs.[98,99] It is common to use lithographic techniques and dry etching in the top-down NW fabrication. Therefore, the top-down method has limitations in producing

NWs with small diameters and long length, especially when the diameter is smaller than 10 nm. Besides, the top-down method needs to prepare the bulk structure before the etching of NWs. This results in a loss of the advantages in dealing with large lattice and thermal expansion coefficient mismatch. Moreover, because most of the material needs to be etched away, it is a big waste.

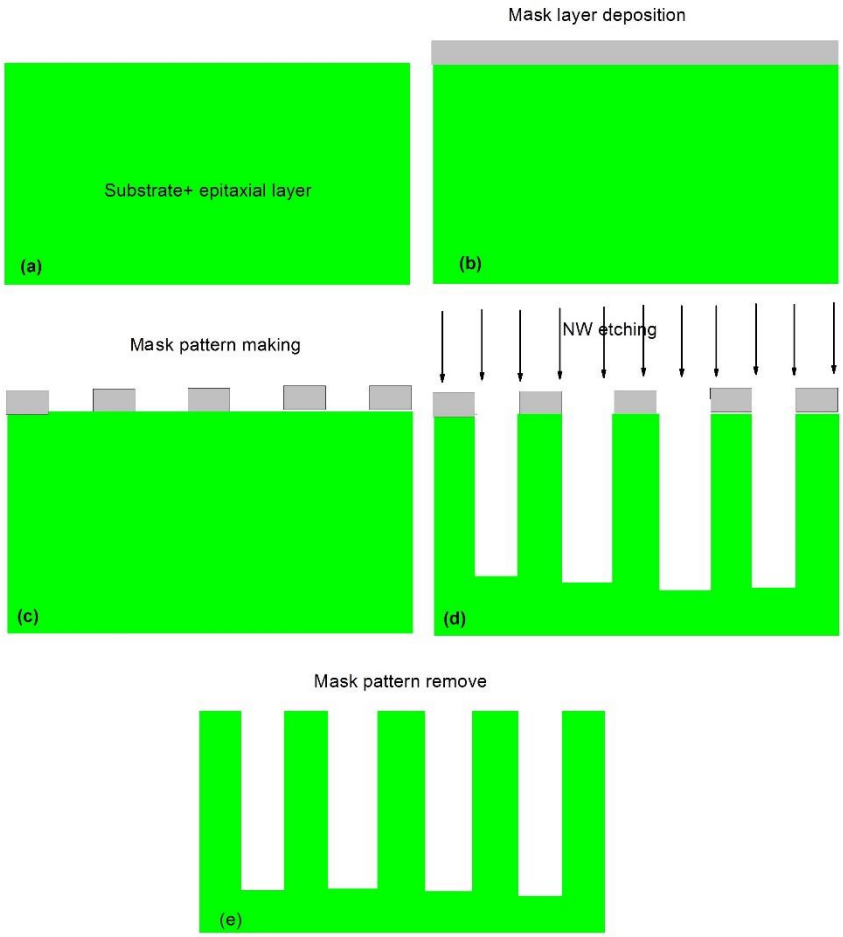

Figure 1-6. Illustration of top-down NW etching process.

The bottom-up method is beneficial for fabricating NWs with small diameters and long lengths. It also has good ability to handle strain. It can thus be used to integrate materials with large lattice and thermal expansion coefficient mismatch. The bottom-up NW fabrication can

be achieved by employing various fabrication methods, such as laser ablation, metal-organic vapour phase epitaxy, chemical beam epitaxy, and molecular beam epitaxy.[100-103] Roughly, they are divided into two groups: catalyst-free growth and catalytic growth.

The catalyst-free growth is a vapour-solid (VS) mode, which is the same as the thin film material growth. However, it needs to stabilize certain crystal facets (side facets) and enhance the growth in only one direction (NW axis). This anisotropic growth is usually achieved with the assistance of a mask. The 2D growth can thus be suppressed and the NWs grow out of mask openings. Therefore, this mode is also known as selective area growth and is beneficial for achieving very highly uniform NWs with good morphology, such as shown in Fig. 1-7. Moreover, the absence of catalytic droplets in the growth can circumvent the reservoir effect,[104,105] which is beneficial for achieving axial junctions with good sharpness. However, the difficult crystal structure control and the parasitic sidewall growth are two major drawbacks of this growth mode.[106,107]

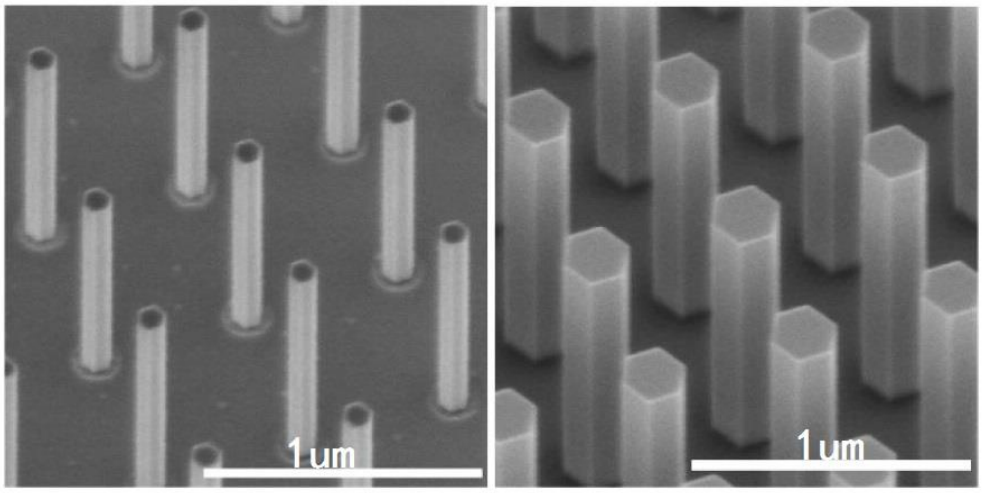

Figure 1-7. Selective area grown GaAs NWs. Reprinted with permission from Ref.10. Copyright 2014 American Chemical Society.

The catalytic growth is achieved with the assistance of nanometre-sized catalytic particles, such as in Ga-catalyzed GaAs NWs shown in Fig. 1-8 and 1-9. However, it is still debatable on the catalytic role of the particle.[108] During the growth, source materials are collected by the particle. When it is oversaturated, the materials precipitate out of the particle and start the NW growth. The particle size controls the NW diameter if the NW sidewall is free from radial growth. Depending on the catalyst particle material, this growth mode can be further divided into two categories of foreign metal catalyzed and self-catalyzed growths.[109]

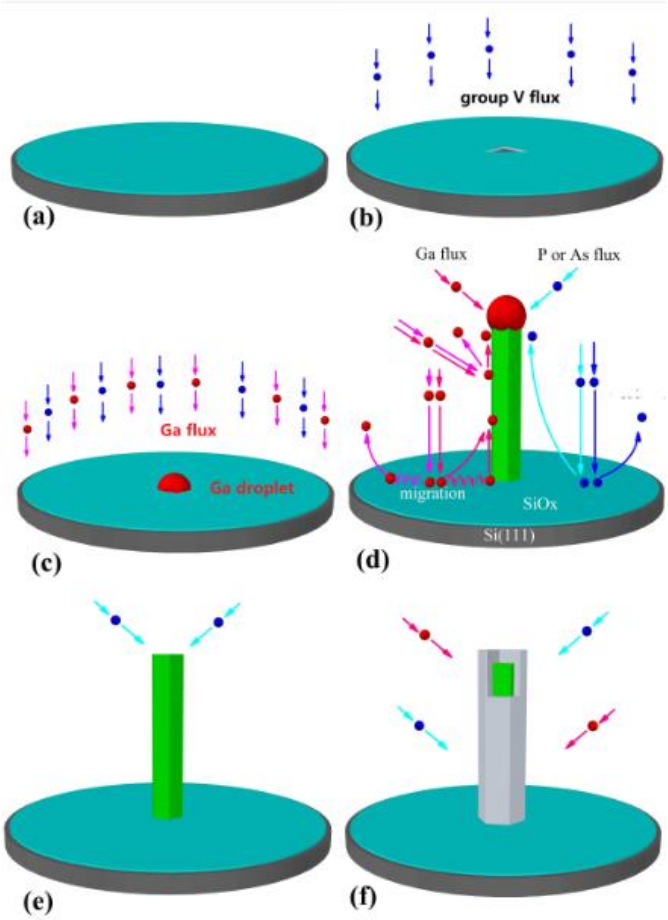

Figure 1-8. Illustration of the Ga droplet catalyzed NW growth procedures. (a) Native oxide formation on Si substrates. (b) Pinhole formation on the native oxide layer. (c) Ga droplet formation. (d) NW growth. (e) Ga droplet consumption. (d) NW shell growth.

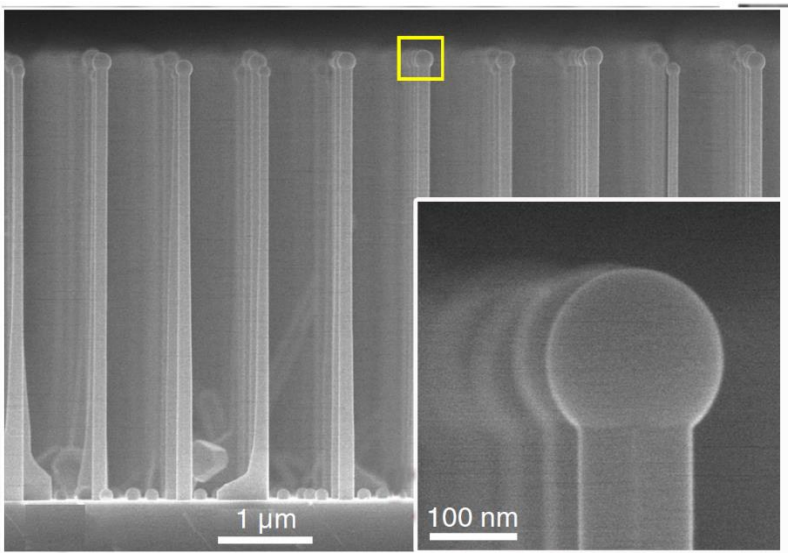

Figure 1-9. Droplet-catalyzed GaAs NWs. Adapted with permission from Ref.[110]. Copyright 2014 American Chemical Society.

In the foreign metal catalysed NW growth, a lot of metals can be used as the catalyst particle, such as gold, nickel, palladium, platinum, manganese, copper, silver, bismuth and iron.[111] Among them, Au is the most popular one. Its melting temperature is moderately low, which can facilitate formation of the low-melting alloys.[111] At the growth temperature, Au droplets are liquid and the NW growth follows the vapour-liquid-solid (VLS) mode.[112] The diffusion coefficients of group-III and V elements are quite high in the liquid Au alloy.[111] In addition, Au has good resistance to oxidation and other parasitic reactions, which can facilitate the growth preparation.[111] During growth, the Au droplet is un-consumable and its volume is almost unchanged, which endows the NW growth with a large growth window, especially the growth temperature and V/III flux ratio. Therefore, compared with other growth modes, it is easier to adjust the NW properties such as axial/radial selectivity, crystal phase, growth direction, and growth rate using the Au-catalysed growth. As presented by Joyce *et*

al.,[113] a two-step growth with a temperature difference larger than 100 ºC was used in their GaAs NW growth. With this technique, their NWs were purely ZB and had very high vertical yield. Besides, the large growth window of this mode is beneficial for the growth of NWs that contain more than one group-III element. For example, NWs composed of $Ga_xIn_{1-x}P$ $(0.2\leq x\leq 1)$[114], $Ga_xIn_{1-x}As$ $(0\leq x\leq 1)$[115,116] and $Ga_xIn_{1-x}Sb$ $(0.3\leq x\leq 1)$[117] have been demonstrated. Similarly, growth of axial group-III heterojunctions can also benefit from this mode and achieve a large composition change. For example, GaSb/InAs[118,120] and InP/GaAs[121] heterojunctions have been demonstrated with high-quality heterointerfaces. On the other hand, Au has a lot of drawbacks, which make it rather unpopular. When incorporated into Si it can form mid-gap energy states, which can affect the device performance.[122,123] Besides, the good solid diffusivity of Au makes it extremely hard to be removed from the exposed equipment. Therefore, the Au-catalysed growth is incompatible with the CMOS processing. In NWs Au can be incorporated with high concentrations. For example, it has been found that Au doping concentration in GaAs and InAs NWs is in the order of 10^{17} ~10^{18} /cm^3.[122,124] Breuer *et al*.[123] made a direct comparison between Au- and self-catalysed GaAs NWs and found that Au-catalysed NWs have lower photoluminescence intensity and shorter carrier lifetimes. However, some other researchers argue that the influence of Au on NWs is negligible, especially for the optical properties.[125,126] For the shell growth, presence of the Au particle can seriously degrade the shell morphology. The NW tip and the sidewalls are adopting VLS and VS growth modes, respectively.[127] This could cause different growth rates, composition profiles, and doping concentrations along the axial and radial directions.[126]

For the self-catalyzed growth, group-III metals with a low melting point and high boiling

temperature are normally used as the catalyst. Due to the low melting temperature of group-III metals, the self-catalysed growth follows the VLS growth mode. Because the material of catalyst droplets is also one component of the NW, it does not introduce extra contamination, which is diametrically different than the foreign metal catalyst. When the core NW growth is finished, the catalyst droplet can be consumed by group-V flux. Therefore, the VLS growth can be terminated, which is beneficial for achieving good shell morphology, such as in the self-catalyzed GaAsP core-shell NW shown in Fig. 1-10. On the other hand, the consumable feature of the catalyst droplet significantly limits the NW growth window because the dynamic balance between consumption and accumulation of group-III species in the droplet is extremely sensitive to the growth condition, especially the temperature and V/III ratio. As a result, it is difficult to make a large parameter change during the growth. This adds difficulty to the selective control of NW crystal structure. Moreover, the small growth window of this mode makes it difficult to grow NWs that contain more than two group-III elements. This is because different group-III elements have quite different optimum growth parameters, especially the growth temperature.[128,129] As reported by Paek *et al.*,[129] the In content in their InGaAs NWs was limited to 1~2% even if they were using a high In/Ga flux ratio. Heiss *et al.*[130] also encountered the same problem. They changed the growth temperature over a large range during the InGaAs NW growth, but the In composition was still limited to 3~5%. This issue can cause further problems with the fabrication of axial group-III heterojunctions. Although changing the growth condition could be a solution, the consumable feature of the catalyst droplets makes it difficult to be realized. As a result, the growth of self-catalysed heterojunctions prefers to switch group-V elements that are

comparatively less sensitive to the growth conditions, such as the GaAs/GaAsSb.[131]

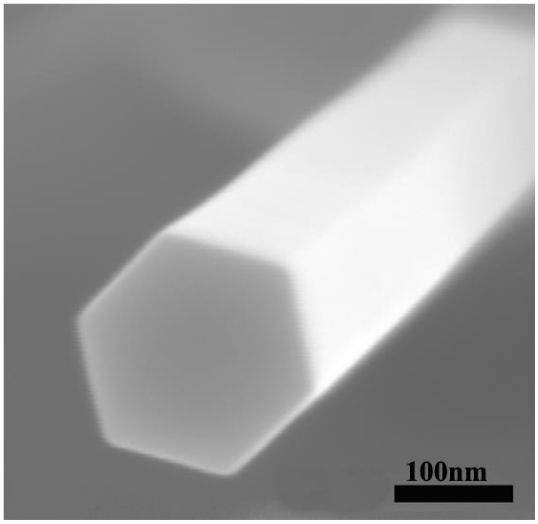

Figure 1-10. SEM image of a Self-catalyzed GaAsP core-shell NW.

1.4 Stacking Faults and Crystal Structure Control of III-V Nanowires

The crystal phase change between ZB and WZ structures happens when the material stacking is along the <111> crystal direction of the cubic cell or the <0001> direction of the hexagonal cell. The spacing of the third nearest-neighbour atoms in the WZ structure is shorter than that in the ZB phase, which causes a small energy difference of about 25 meV for each atomic pair.[132-134] Considering the physical origins, it is the competition between the Coulomb force and the steric hindrance that decides the crystal structure.[135] The Coulomb force increases with the ionicity and prefers to reduce the bond length between atoms, while the steric hindrance increases with the atom size and tends to increase the bond length.[136] This makes high-ionicity and small-steric-hindrance materials grow in WZ structure. That is the reason why in thin film growth nitrides tend to adopt WZ structure, while other III-V materials prefer ZB phase. In the NW growth, similar effects can be observed. Nitride NWs

still prefer WZ structure and antimonide NWs favour ZB. Avit *et al.*[11] fabricated GaN NWs and found that they are WZ and defect-free for a length as long as tens of micrometres (Fig. 1-11). Conesa-Boj *et al.*[137] found that ZB GaAsSb NWs can be defect-free even down to the first bilayer (Fig. 1-12). Yang *et al.* [9] fabricated ZB InSb NWs with a diameter as small as 4.5 nm (Fig. 1-13). However, other materials, with moderate ionicity and steric hindrance values, can adopt both ZB and WZ phases and hence have high stacking faults. As demonstrated in InAsSb NWs, increasing the Sb composition can change crystal structure from perfect WZ to perfect ZB phase.[138] Although there is no consensus on the crystal phase control mechanisms, scientists still found some parameters that can be used to repeatably control the crystal structure of NWs.

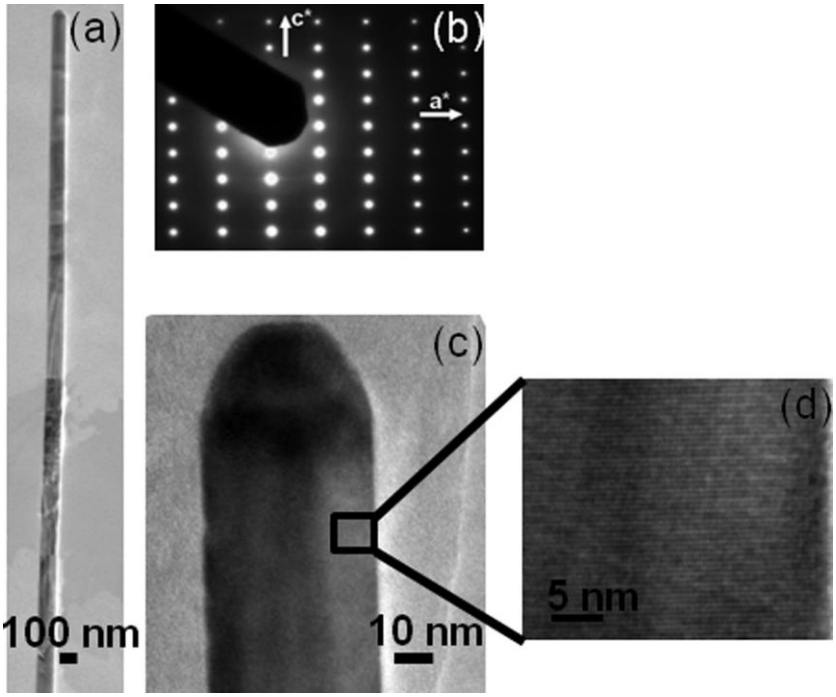

Figure 1-11. TEM image of (a) a whole GaN NW; (c) the tip of (a); (d) sidewall of (a). (b) Electron diffraction pattern from (a). Reprinted with permission from Ref. 11. Copyright 2014 American Chemical Society.

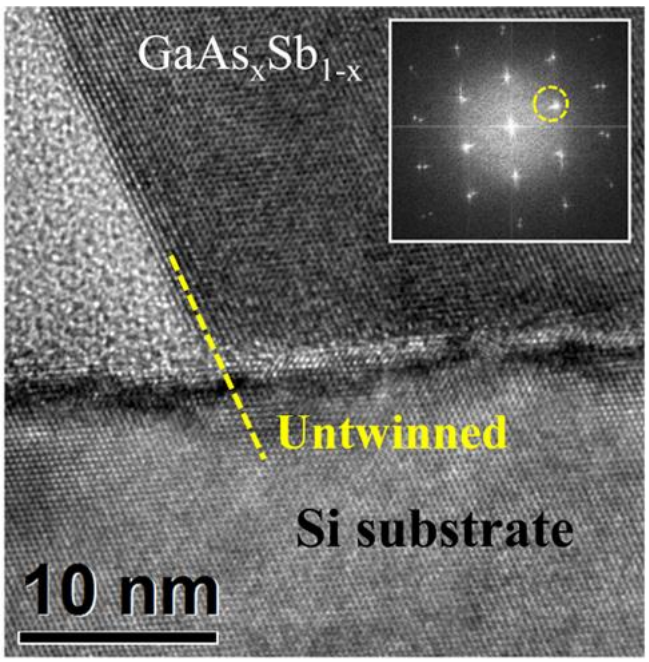

Figure 1-12. TEM image of the GaAsSb NW/Si substrate interface. [137]

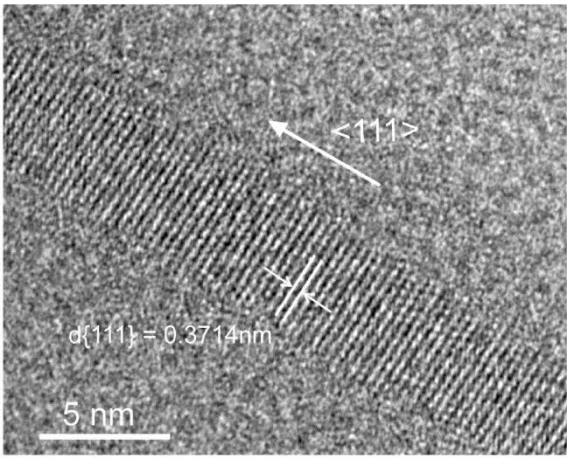

Figure 1-13. TEM image of a InSb NW. Reprinted with permission from Ref.9. Copyright 2010 American Chemical Society.

Because stacking faults occur in the <111>B or <0001> direction, avoiding these growth directions can effectively suppress the formation of stacking faults. This has been confirmed by pure-ZB defect-free NWs grown along the <100> (InP, InAs)[139-142], <110> (InAs, GaAs)[143,144] and <111>A (GaAs)[145] directions. But the <111>B or <0001> direction is the

most energetically favourable for NWs. The change of the NW growth direction away from these two directions is not easy. Krishnamachari *et al*.[141] demonstrated the importance of the substrate pre-treatment in growing Au-catalysed (100) InP NWs on InP (100) substrates (Fig. 1-14). They found that the initial high temperature annealing prior to the growth of NWs is detrimental for the (100) growth. This could be due to the etch of the substrate by Au droplets that can lead to the appearance of the (111)B facets. Wacaser *et al*. also observed similar phenomenon when growing <111>A GaAs NWs on GaAs (111)A substrates.[145] Moreover, the liquid−vapour interface energy is also an important parameter to control the growth direction of NWs. As demonstrated by Wang *et al*.,[146] the In composition in the Au droplet controls the liquid−vapour interface energy. With an increase of In content in the droplet, the yield of <100> InP NWs was increased from 27 ± 1% to 97 ± 1%. With this method, they also achieved the reversible switch of the growth direction between the <111>B and <100> (Fig. 1-15).

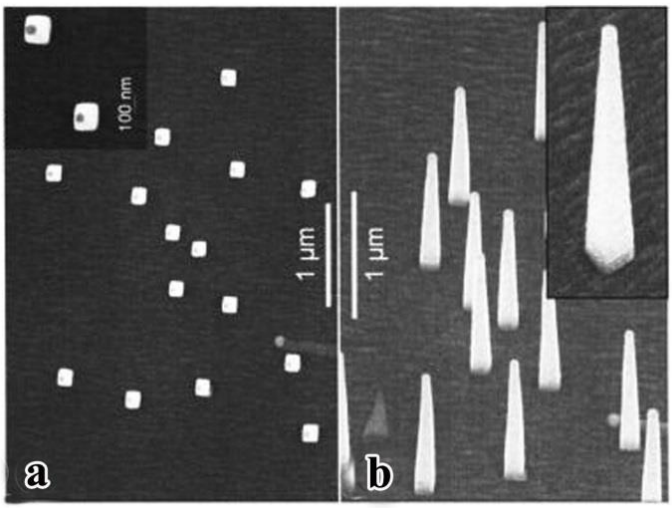

Figure 1-14. (a) SEM top view and (b) tilted view (30°) of Au-catalyzed InP NWs grown on InP(001). Reprinted with permission from Ref. 141. Copyright 2004, AIP Publishing LLC.

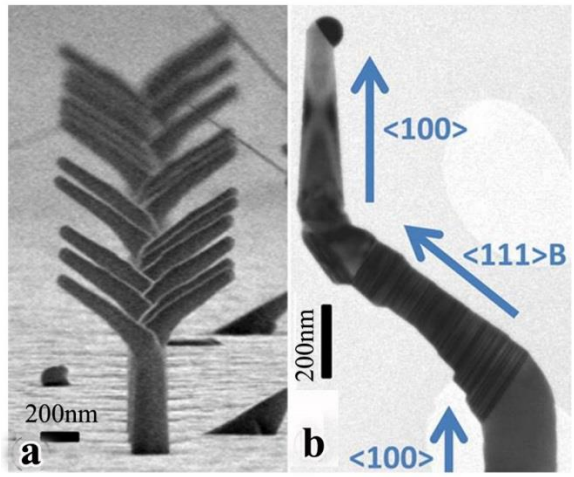

Figure 1-15. Reversible growth direction switch between <111>B and <100> of the Au-catalyzed InP NWs. Reprinted with permission from Ref. 146. Copyright 2013 American Chemical Society.

When the NW growth needs to be along the <111>B or <0001> directions, the crystal structure control is more complex. It was found that the crystal structure is related to the NW diameter. As demonstrated by Caroff *et al.*,[147] InAs NWs were WZ and almost stacking-fault-free when their radii were 24 nm, while when their radii increased to 110 nm they were pure ZB (Fig. 1-16). The thermodynamics reveals that the free energy of each atomic pair increases with the surface-to-volume ratio.[148] In addition, the WZ structure with a lower surface energy is preferable for reducing the free energy compared with the ZB phase. Therefore, there should be a critical radius below which NWs are more stable in the WZ structure.[149] As reported by Shtrikman *et al.*,[133] their GaAs and InAs NWs of the order of 10 nm are pure WZ and free of stacking faults. However, the critical radii predicted by thermodynamics are too small (e.g. 12–32 nm[133]): in practic NWs can have WZ phase with a much larger diameter (>50 nm) and they can also be ZB with a diameter as small as 5 nm.[9] Therefore, in addition to the thermodynamics, the nucleation kinetics needs to be taken into

consideration.[150]

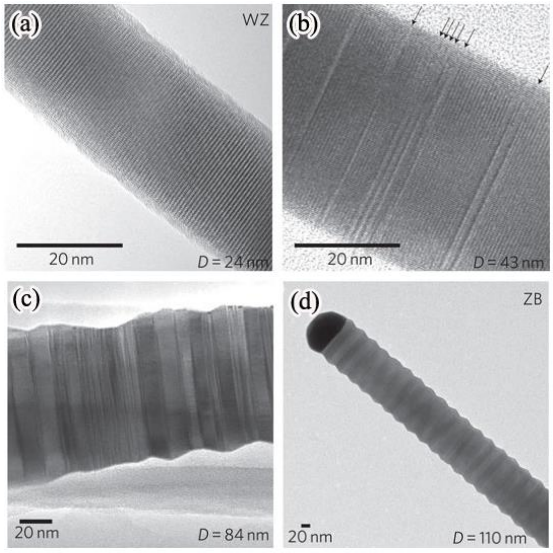

Figure 1-16. Change of InAs NW crystal structure from WZ to ZB by increasing diameter. Reprinted by permission from Macmillan Publishers Ltd: Nature Nanotechnology 147, copyright 2008.

For the droplet catalysed growth, the perimeter of the NW/droplet interface is the triple phase line (TPL), where vapour, liquid and solid phase meet. It is widely accepted that the nucleation at this TPL is energetically more favourable. The droplet supersaturation controls the nucleation structure, with the WZ nucleation probability increasing with supersaturation.[151,152] Johansson *et al*.[153] suggested that the supersaturation of droplets is linked directly to the Gibbs–Thomson effect that can have significant influence even at comparatively large diameters. Based on this, they calculated the critical radii for the ZB/WZ phase transition. These critical radii are much larger and more realistic (Fig. 1-17) than those suggested by thermodynamic calculations. Apart from the diameter, the growth conditions also have strong influence on the supersaturation. For example, the droplet supersaturation can increase with concentrations of the reactant inside.[154,155] As reported by Johansson *et al*.,[156] the reduction of Ga concentration and hence supersaturation of the Au droplets can

significantly increase the ZB structure percentage in GaP NWs (Fig. 1-18). Moreover, during the growth the temperature is also a key factor which can significantly influence the supersaturation.[147] It has been shown that the decrease of growth temperature can greatly increase the WZ structure percentage in InAs NWs. Caroff *et al*.[147] even demonstrated axial WZ/ZB phase superlattices by periodically tuning the growth temperature of InAs NWs (Fig. 1-19). Controlling the droplet supersaturation has been proved to be quite effective. However, for some extreme cases, it is still difficult to explain the nucleation phase by supersaturation. For example, some researchers found that the fast growth with a high droplet supersaturation can still produce high-quality ZB NWs.[157,158]

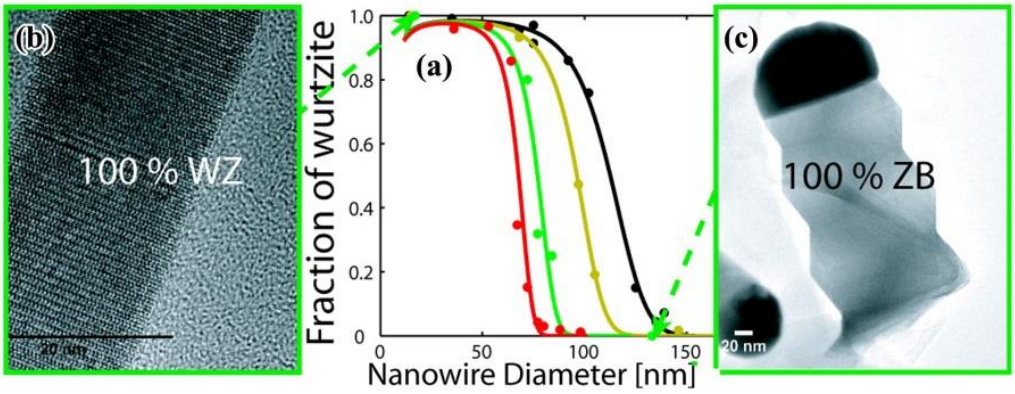

Figure 1-17. Diameter-dependent crystal structure change of InAs NWs. Reprinted with permission from 153. Copyright 2010 American Chemical Society

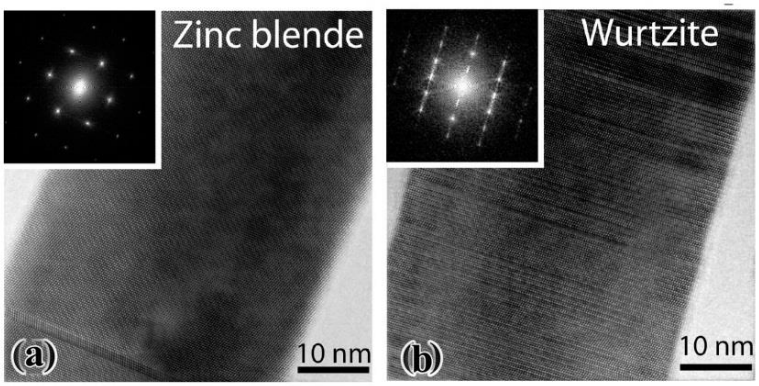

Figure 1-18. Crystal structure of GaP NWs grown with Au droplets of (a) low (plused Ga flux) and (b)

high (continuous Ga flux) supersaturation. Reprinted with permission from 156. Copyright 2009 American Chemical Society

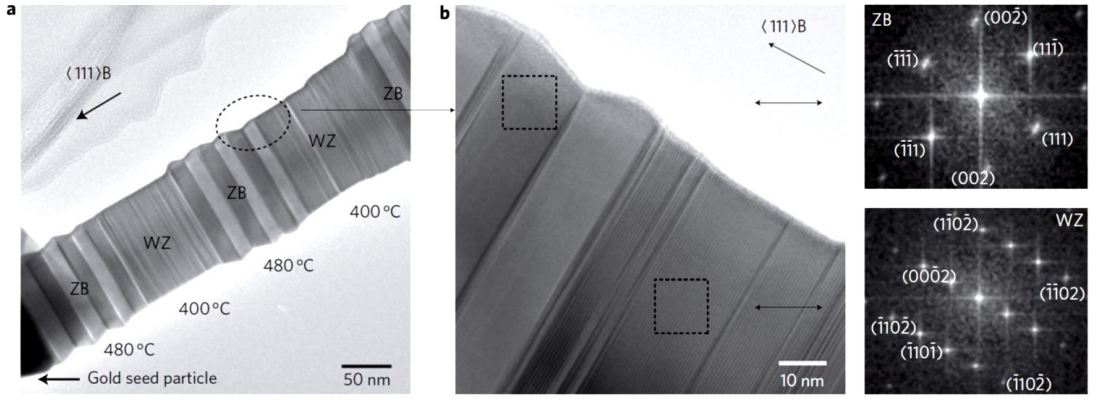

Figure 1-19. WZ–ZB phase superlattice in an InAs NW. Reprinted by permission from Macmillan Publishers Ltd: Nature Nanotechnology 147, copyright 2008.

The nucleation at the TPL can be suppressed by lowering the surface energies of the droplets.[159] If it is not at the TPL, the nucleation prefers ZB crystal structure.[152] The surface energy of Au droplets can be lowered by increasing the concentration of group-III elements inside. Dheeraj *et al.*[160] demonstrated changing of the crystal structure of GaAs NWs from WZ to ZB by increasing the Ga concentration in Au droplets. By controlling the Ga concentration, they also achieved high-quality WZ/ZB/WZ axial phase heterojunctions. Gil *et al.*[159] increased the Ga concentration in Au droplets over 0.62 during their GaAs NW growth and achieved pure ZB crystal structure for NWs with diameters as small as 5nm (Fig. 1-20). Apart from group-III elements, it is suggested that group-V elements also have similar effect. As demonstrated by Lehmann *et al.*,[161] the rapid increase of group-V fluxes to about 50−150 times higher can quickly change the crystal structure of Au-catalyzed GaP, GaAs, InP, and InAs NWs from WZ to ZB (Fig. 1-21). Joyce et al presented the combined effects of both

group-III and V elements.[158] They demonstrated that the rapid GaAs NW growth, by increasing both Ga and As fluxes, can achieve defect-free ZB crystal structure (Fig. 1-22). Apart from the group-III and V elements, some other elements are also believed to be able to affect the surface energy and hence control the crystal structure of nucleation. For example, Zn doping can promote ZB phase formation in the InP NW growth,[162,163] while S doping can induce WZ nucleation.[164,165] Apart from the surface energy of the droplets, the surface energy of the external vapour-nucleus facet can also affect the crystal structure of the nucleation. As demonstrated by Joyce *et al*.,[166] a high group-V flux can make vapour-nucleus facets become beneficial for ZB nucleation. In their InAs NW growth, a low (high) temperature and high (low) V/III ratio can produce pure ZB (pure WZ) crystal structure over a wide range of NW diameters (~30-100 nm) (Fig. 1-23).

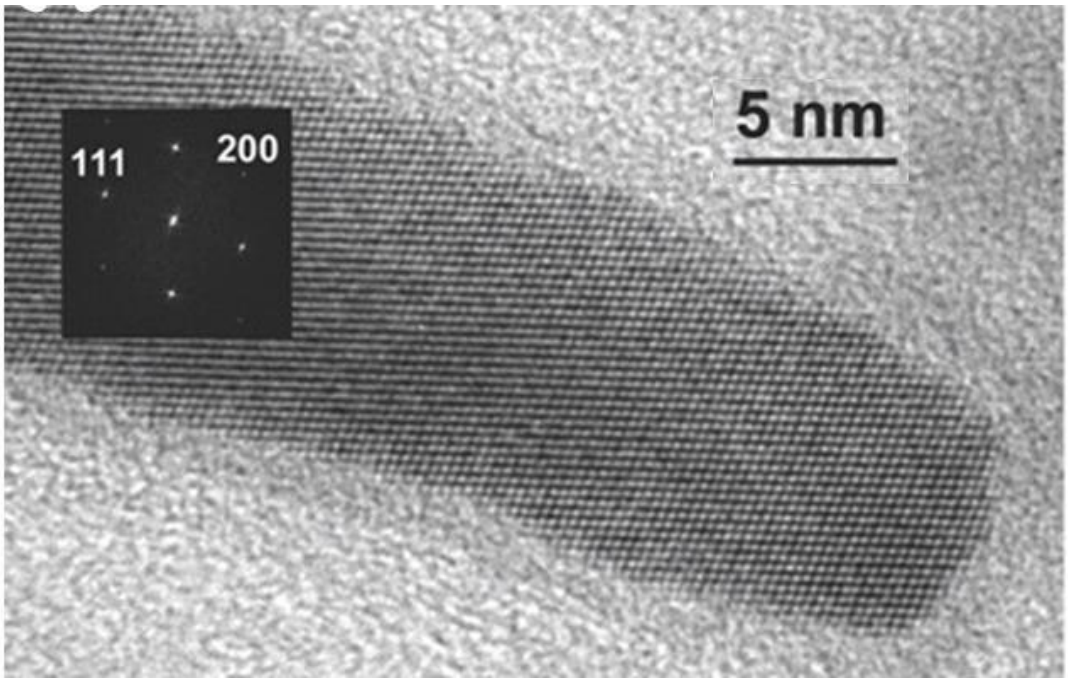

Figure 1-20. Pure ZB GaAs NW with a radius of 5−6 nm. Reprinted with permission from 159. Copyright 2014 American Chemical Society.

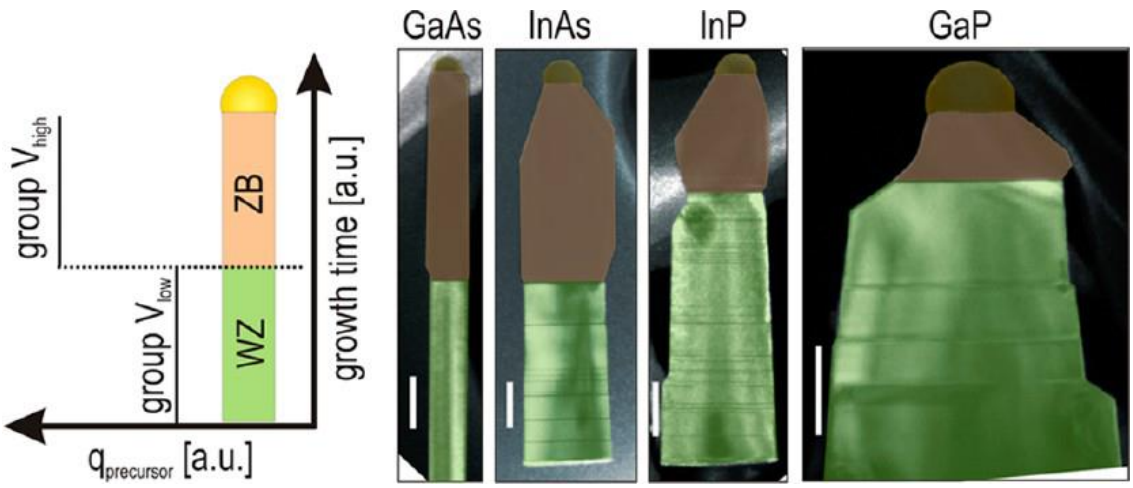

Figure 1-21. Abrupt WZ/ZB phase switch in GaAs, InAs, InP and GaP NWs. Reprinted with permission from 161. Copyright 2013 American Chemical Society.

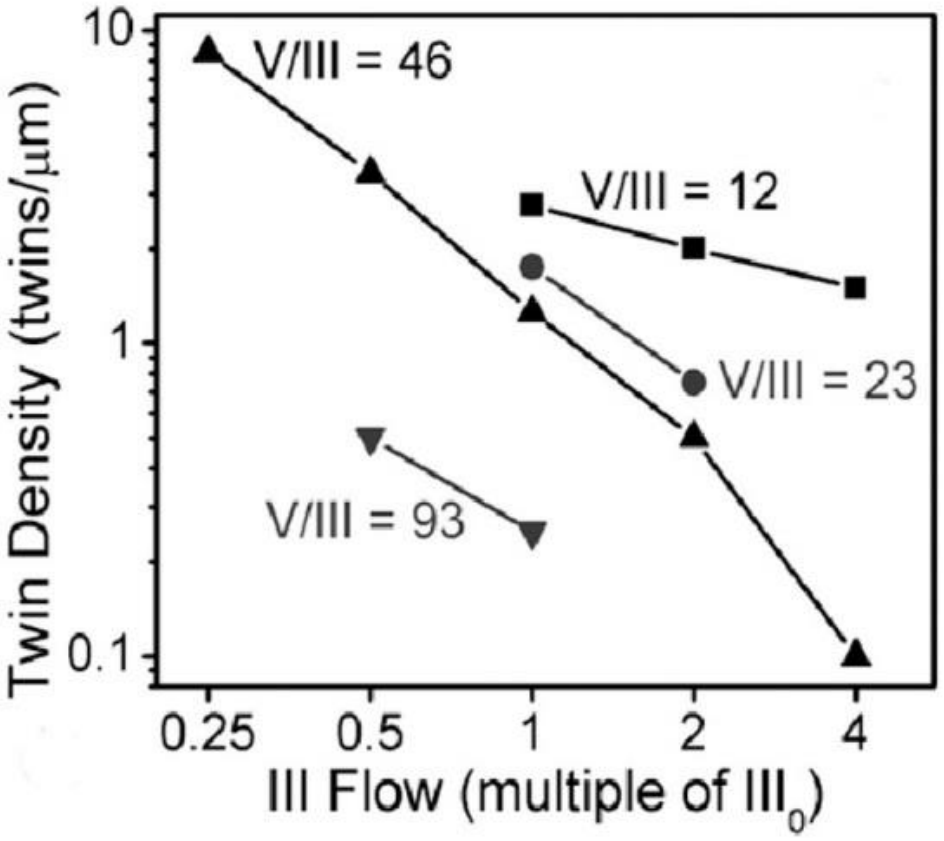

Figure 1-22. Twin density versus group-III flux for GaAs NW growth with different constant V/III ratios. Reprinted with permission from 158. Copyright 2009 American Chemical Society.

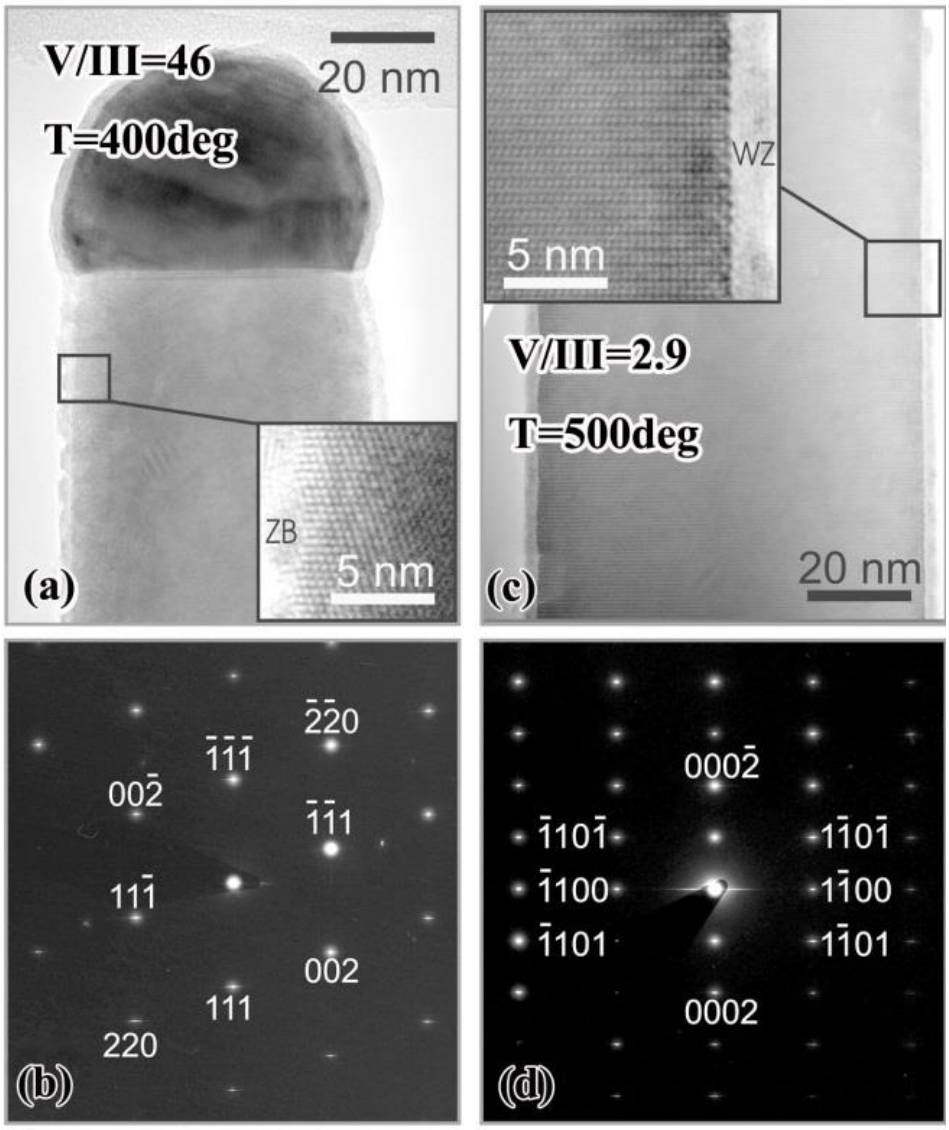

Figure 1-23. (a) (b) pure ZB and (c) (d) pure WZ InAs NWs grown at group-V rich and poor conditions, respectively. Reprinted with permission from 166. Copyright 2010 American Chemical Society.

Besides changing the composition of catalyst droplets, the shape of the droplets can also influence the crystal structure of the nucleation. In the model proposed by Krogstrup *et al.*,[167] for the droplet with a low wetting angle and moderate size, a large proportion of its TPL contacts directly with the edge of the NW top facets, which promotes the WZ formation.

When reducing the droplet size, the TPL will be contracted from the edge to the top facet. If further increasing the droplet size from moderate size, the TPL will proceed to the side facets. Both these situations are favourable for the ZB nucleation. All these cases are illustrated in Fig. 1-24. As observed by Rieger *et al*.,[168] during the Ga droplet consumption of GaAs NWs, the reduction of the droplet contact angle from about 137° to 90° can change the crystal structure from ZB to WZ. Further consuming the droplet, the TPL receded to the NW top facet and the crystal structure was changed back to ZB. They also achieved the reversible change between the WZ and ZB phase by controlling the droplet size. Munshi et al. presented similar results[169] in their GaAs NW growth. They demonstrated a good control of high-quality WZ/ZB phase junctions by changing the droplet size. For the Krogstrup's model, Yu *et al*.[170] made some supplements. They suggested that the formation of defects could be induced by the shift of the TPL along the NW sidewalls. They observed the occurrence of a defect section before the crystal structure was changed to pure WZ GaAs during the Ga droplet consumption. Besides, they demonstrated the growth of ZB/defect-section superlattices and WZ/defect-section superlattices through changing the Ga droplet size, which also supports their defect-formation theory (Fig. 1-25). Apart from the droplet shape related TPL position change, distortion of droplets could also cause formation of defects. As proposed by Algra *et al*.,[163] the tilted angles of NW side facets can keep changing the shape of NW cross section and hence cause droplet deformation. In the end, the deformation energy is released by introducing the twin plane. The twin plane can change the tilt directions of the side facets and start a new cycle of strain accumulation. Due to this periodical accumulation and release of strain energy, InP twinning superlattices have been achieved (Fig. 1-26).

Figure 1-24. Illustration of the influence of the TPL position and the nucleation location on the nucleation crystal structure. (a) Top facet contact. (b) Top facet edge contact. (d) Sidewall contact.

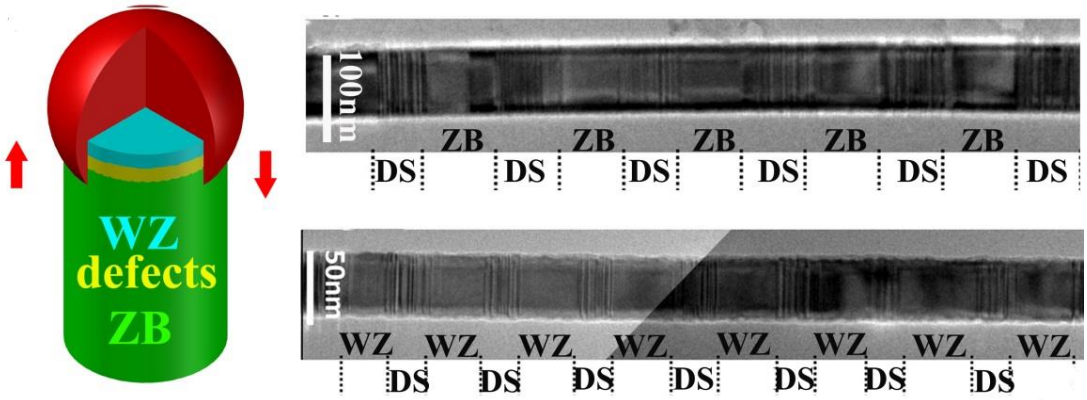

Figure 1-25. ZB/defect-section and WZ/defect-section superlattices induced by the TPL shift along the sidewall. Reprinted with permission from 170, Copyright 2012 American Chemical Society

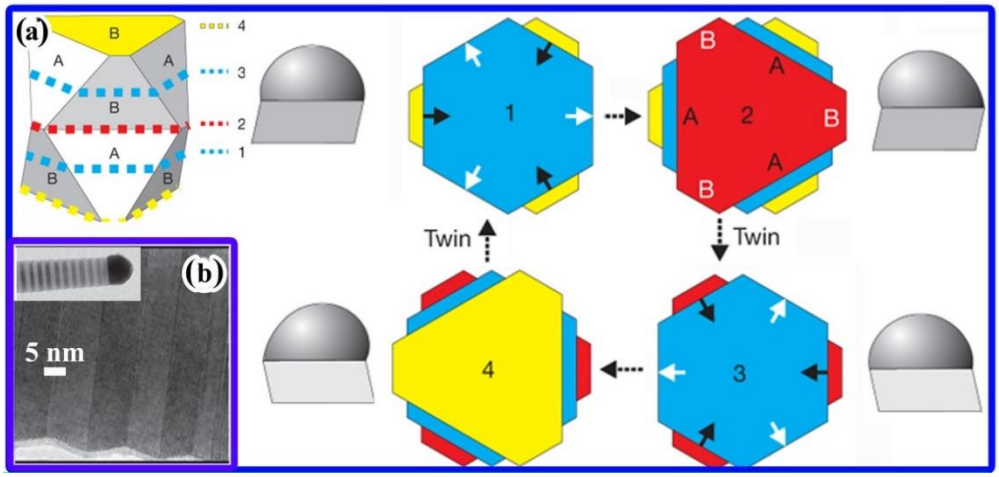

Figure 1-26. InP NW twinning superlattice and its formation mechanism. Reprinted by permission from Macmillan Publishers Ltd: Nature[163], copyright 2008.

Most of the factors mentioned above are highly coupled. For example, the flux, the droplet composition, the droplet surface energy, the seed particles deformation and the droplet contact angle are all interconnected. Besides, the growth temperature, the adatom surface diffusion and desorption, the solubility and chemical content of the seed particle, the effective V/III ratio, and the droplet chemical potential are also closely linked. Therefore, it is difficult to clarify which factor is the key parameter that determines the results. Instead, an overall consideration is needed in the NW growth design and growth analysis.

1.5 Solar Cell Application of III-V Nanowires

In the present world, the energy issues are a big concern. We are running out of the traditional energy resources that we have been relying on. Besides, the combustion of these fossil fuels can cause serious environmental pollution. Because of these, scientists have been searching for new energy resources for decades. Especially in recent years, it has attracted more and more attention. It is widely accepted that the solar energy can be a strong candidate, because it is plentiful, ultra-clean and renewable. The research in the solar energy harvesting, such as solar cells (SCs), has been investigated for decades in thin film structure.[171,172] However, finding the balance between efficiency and cost is still a major obstacle, which stops the solar power from being widely used in our daily life. Especially, the lattice and thermal expansion coefficient mismatch issues can significantly increase the difficulties and cost of the SC fabrication.

By using the NW structure, SCs have the potential to achieve both high efficiency and low cost due to such advantages as better photon harvesting and carrier extraction

efficiencies.

The NW has a 1D structure with a subwavelength diameter and high refractive index. These structural features make the electromagnetic modes of NWs leaky, so they can interact more effectively with the outside media.[173] As a result, the absorption cross section of NWs can be significantly enlarged compared with their physical size.[174] This allows NWs to absorb light from outside their projected area. In addition, the waveguide modes of NWs can guide light to propagate along their axis, which can further enhance the photon absorption.[174] By controlling the NW diameter, we can control the absorption wavelength of the leaky modes.[175-177] This can achieve the wavelength-selective absorption enhancement. Due to easy adjustments of some other geometry parameters,[178] such as the NW length,[179] profile[180] and density, tailoring the absorption spectrum is more straightforward than in thin film devices, which is beneficial for current matching in multi-junction devices.[181] When a large number of NWs stand together on the substrate surface, they can form a refractive index transition layer, which can avoid the abrupt refractive index difference between air and substrate.[182] This can significantly reduce the light reflectance.[183-185] Besides, the arrays formed by NWs with sub-wavelength dimensions can offer a strongly enhanced light scattering effect.[186,187] Therefore, the light propagation path in the absorbing media can be significantly elongated, which makes the effective optical thickness well exceed the Lambertian limit.[188-191] As demonstrated by Garnett *et al*.,[192] the light propagation path in NW arrays is 73 times longer compared with its actual physical thickness. This advanced light trapping ability can greatly enhance the light absorption within a wide range of incident angles.[193,194] Diedenhofen *et al*.[180] reported that their InP NWs (3 μm) have an omnidirectional absorbance of more than 80%

in the wavelength range from 400 to 850 nm. Zhang *et al*.[175] showed that their off-substrate GaAs NWs, with a length of the 1.6 μm and a low surface coverage of only 15%, have a solar-weighted above-bandgap absorbance of 94%. Wallentin *et al*.[195] reported that the short-circuit current generated by their InP NWs (~1.5-μm long, 12% surface coverage) is about 83% of the best InP planar cells. Apart from the enhanced absorption, NWs can also function as waveguides to lead the below bandgap photons into the substrate, which is highly beneficial for multi-junction devices. As demonstrated by Diedenhofen *et al*.,[180] their InP NWs can couple more than 90% of the below bandgap photons into the underlying substrate. Due to the advanced photon harvesting functions, NW devices can use a much smaller amount of material to achieve high absorption efficiency. Compared with the thin film technique, this is beneficial for saving the rare materials and greatly reducing the cost.

The NW can provide advanced extraction capability for the generated carriers. In SC, the generated carriers are difficult to be extracted if they are more than one diffusion length away from the space charge region. Therefore, the minority carrier diffusion length determines the carrier collection efficiency. If the defect density in SCs increases, the minority carrier diffusion length will reduce and hence the carrier collection efficiency will drop.[196] In thin film structures, the carrier collection is along the same direction as the solar photon travelling path.[197,198] Therefore, in order to adequately absorb the photons, a thick absorber is preferred. However, this gives high demand for the crystal quality in order to achieve long carrier diffusion length. As a result, the cost can be significantly increased. For the NW devices with core-shell p-n junctions, the light absorption is along the entire NW, while the carrier separation is along the radial directions (Fig. 1-27). Due to the small radius of NWs, the radial

distance that carriers need to pass before being collected is smaller than or comparable with their diffusion length. Therefore, decoupling paths for light absorption and carrier separation can ensure good efficiency. Besides, the large surface-to-volume ratio of NWs gives them a large junction area, which can further increase the carrier separation efficiency. As a result, the use of lower-purity materials can still obtain high efficiency and hence reduce the device cost.

Various materials have been used to fabricate NW SCs, such as GaAs,[174] InP,[195] InGaAs,[199] InGaP,[200] InAsP,[201] GaAsP,[202] and InGaN[203]. There are two main types of junctions used in NW SCs, axial and core-shell junctions (Fig. 28). The axial junction is more advantageous for easier and better contacts formation because the contacting layers are far away from the active region. On the other hand, the core-shell junction is more sensitive to the device fabrication process, because the active region is just hundreds of nanometres beneath the contact metal and can be easily damaged during the device processing. However, this structure is beneficial for the carrier separation and collection.

The research of NW SCs involves both single and array (large area) structures. The investigation of single NW SCs can help to understand the limiting factors for the NW SCs and find ways to improve. Besides, the single NW SC can be used in low power circuits. So far, the single NW SC, with the NW lying horizontally on the holder substrate, can achieve an efficiency of 10.2% by using self-catalyzed GaAsP core-shell p–i–n NWs (1 Sun, AM1.5G) (Fig. 1-29).[202] These NWs with an energy bandgap of 1.7 eV were grown on Si substrate. This design is aiming for the combination of the 1.7 eV III-V NW SC with the Si bottom SC,[204] which is promising to achieve an efficiency of 33.8% (one Sun, AM1.5G) and 42.3% under

concentrated light (500 Suns, AM1.5G).[205] Most of the single NW SCs are made from single junction NWs. However, Heurlin *et al*.[206] demonstrated an axial tandem single InP NW SC. This axial tandem junction was formed by connecting two p-n junctions axially through a heavily doped p-n tunnel junction. The authors reported an open-circuit voltage of 1.15 V (one Sun, AM1.5G), which is 67% higher than for single junction devices. This demonstrates that the multi-junction NW devices fabrication gives promising results, which is beneficial for achieving high efficiency and open-circuited voltage. Most of the single NW SCs were measured with the light projected perpendicular to the NW axis. In this configuration, their efficiency is underestimated due to weakened light coupling. As proposed by Heiss *et al*.,[207] the efficiency of the GaAs NW SC can be underestimated by a factor of 1.6~7.0. Therefore, if the light is projected along the NW axis, the NW SC efficiency can be greatly enhanced. Krogstrup *et al*.,[174] achieved a record-high efficiency of 40% in their GaAs core-shell p–i–n SCs by making them stand vertically on the substrate (one Sun, AM1.5G). The good performance of single NW SCs make the fabrication of large-area high-power-output NW array SCs promising. Wallentin *et al*.[195] reported an efficiency of 13.8% in their axial p–i–n InP NW array SCs (one Sun, AM1.5G). An open-circuit voltage of 0.906 Volt was achieved in these SCs, which is higher than that of the planar structure. The NWs for this SC were grown homoepitaxially on InP substrates. In order to further reduce the cost, the heteroepitaxial growth is necessary to replace the expensive substrates by cheap ones. However, at present, the heteroepitaxially grown NW SCs are still low in efficiency. Such as the devices reported by Shin *et al*.,[201] InAsP NW arrays on Si substrates, with wafer-scale uniformity, good aspect ratio (>100) and high density (>$5\times10^8/cm^2$), only had an efficiency of 3.6% (one Sun,

AM1.5G). This low-efficiency issue could be due to the NW/Si interface quality, device structure and/or contact fabrication.[208] Moreover, Mohseni *et al.*[209] grew InGaAs NW SCs on graphene treated substrates and achieved an efficiency of 2.51% (AM1.5G), which demonstrated the feasibility of using non-crystal substrates. In addition, the NW structure could also be useful for organic SCs. The large surface-to-volume ratio of the NW structure and the high carrier mobility and affinity of the III-V materials can effectively separate the carriers and hence improve the efficiency. For example, Chao *et al.*[210] demonstrated the effectiveness of using the NW structure in the poly(3,4-ethylenedioxythiophene):poly(styrenesulfonate) (PEDOT:PSS) SCs (one Sun, AM1.5G). They found that the SCs with GaAs NWs had an efficiency of 5.8%, while that from the one with only planar GaAs was as low as 0.29% .

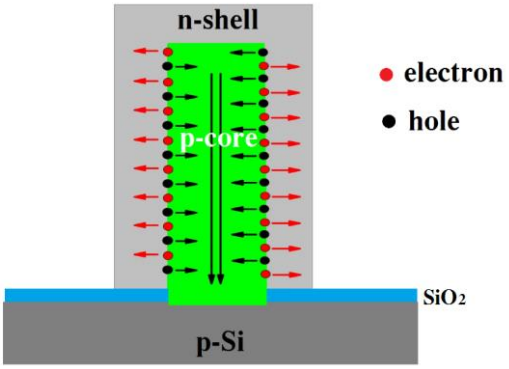

Figure 1-27. Illustration of carrier separation and collection in the core-shell p-n junction SC.

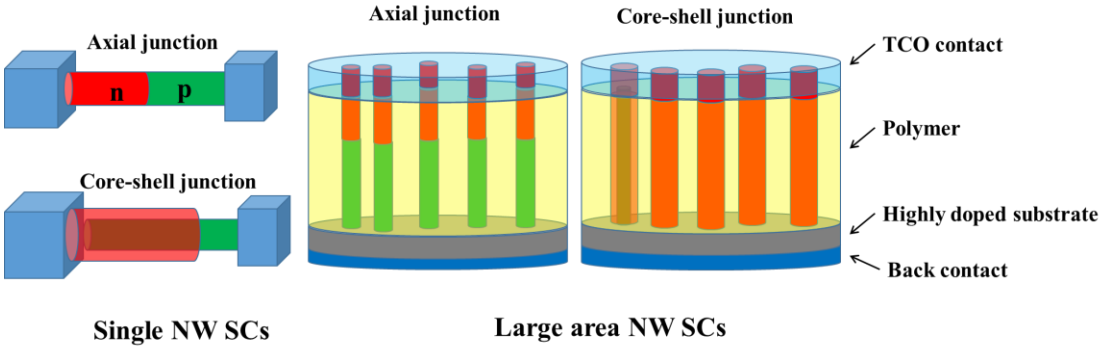

Figure 28. Illustration of some NW SC structures.

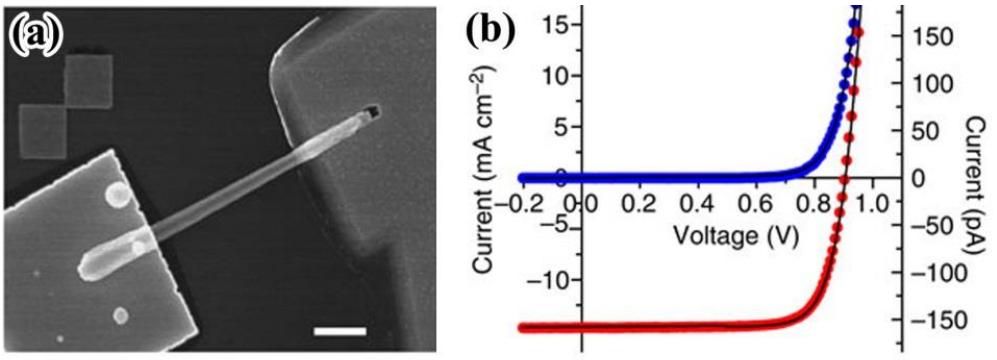

Figure 1-29. Single GaAsP core-shell NW SC and the I-V curve. Reprinted by permission from Macmillan Publishers Ltd: Nature Communications[202], copyright 2013.

1.6 Motivations of Present Work

The self-catalyzed GaAsP NWs use a Ga droplet as the catalyst, which does not introduce any contamination from foreign metals. It is thus compatible with the well-developed Si fabrication processing. After the NW growth, the VLS growth termination by the Ga droplet consumption can facilitate good-morphology high-quality shell growth. This can reduce the cost and avoid extra contamination.

Ternary materials, III-III-V and III-V-V, are popular because of their large bandgap and lattice constant coverage, which can offer more freedom in band structure design and lattice match compared with binary materials.[211-212216] For the self-catalysed NW growth mode, it is difficult to make a large parameter change during the growth, due to the small NW growth window. This makes it difficult to grow self-catalyzed III-III-V NWs, because different group III elements have quite distinct properties and hence different optimum growth conditions.[128-130] GaAsP only contains one group-III element, which helps to circumvent this issue. In addition, the GaAsP NWs are beneficial for growing axial heterojunctions with sharp interfaces by switching As/P composition due to the low reservoir effect.[104,105] This is very

useful for making axial quantum dots, which can have multiple applications such as single photon sources.[217]

Bandgap of the ternary material GaAsP can cover wavelengths ranging from green (550 nm) to near infrared (860 nm) at room temperature, which makes it one of the most promising III−V compound semiconductors for photovoltaics and visible LEDs.[218-220] It has been predicted that a two-junction tandem SC, consisting of a 1.7 eV GaAsP NW junction and a 1.1 eV Si junction, has a theoretical efficiency of 33.8% at 1 sun AM1.5G and 42.3% under 500 suns AM1.5D concentration.[205] If this 1.7/1.1 eV two-junction device is used in water splitting, it has the potential to achieve an efficiency of 27%.[172] Moreover, the GaAsP NW also shows promise for light emitters, such as lasers and LEDs. The working wavelength of these emitters can reach the green region and solve the "green-yellow gap".[221-225]

1.7 Thesis Structure

In this thesis, the investigation of self-catalysed high-quality core-shell GaAsP NWs is presented in six chapters.

The 1st chapter is the introduction to NWs, including the basic structure features, fabrication methods, advantages and applications.

The 2nd chapter gives an introduction of the facilities used for NW growth and characterization, especially the solid-source molecular beam epitaxy.

The 3rd chapter is about the research on the self-catalysed GaAsP NWs on un-patterned Si substrates over a wide range of parameters, such as the V/III flux ratio, growth rate, and growth temperature. The P incorporation efficiency, Be doping, droplet consumption, and uniformity

control were also discussed.

The 4th chapter describes the GaAsP NW shell growth. The key factors that can affect the shell morphology are included, such as the growth rate. The composition uniformity of these core-shell NWs is also investigated. In addition, the surface passivation of these NWs by using a thin layer of InGaP was studied.

The 5th chapter is about the self-catalysed core-shell GaAsP NWs on patterned Si substrates. The importance of using a high-temperature deoxidization step and a Ga pre-deposition step is discussed. In addition, the influence of the patterned hole size is also investigated.

The final chapter is a conclusion of this thesis and contains some suggestions for future work on NWs.

1.8 References

1. Wagner R and Ellis W, Bell Telephone Laboratories: 1965.

2. Yan R, Gargas D and Yang P 2009 Nature Photonics 3 569

3 Lee A D, Jiang Q, Tang M, Zhang Y, Seeds A J and Liu H 2013 IEEE J. Sel. Top. Quantum Electron. 19 1901107

4 Zhang Y-Y and Yao G-R 2011 J. Appl. Phys. 110 093104

5 Zhang Y Y and Yin Y A 2011 Appl. Phys. Lett. 99 221103

6. Yang P, Yan R and Fardy M 2010 Nano Letters 10 1529

7. Lieber C M and Wang Z L 2007 Mrs Bulletin 32 99

8 Zhang Y, Wu J, Aagesen M, Liu H. 2015 Journal of Physics D: Applied Physics, 48(46), 463001.

9. Yang X, Wang G, Slattery P, Zhang J Z and Li Y 2010 Crystal Growth & Design 10 2479

10. Yao M, Huang N, Cong S, Chi C-Y, Seyedi M A, Lin Y-T, Cao Y, Povinelli M L, Dapkus

P D and Zhou C 2014 Nano Letters 14 3293

11. Avit G, Lekhal K, André Y, Bougerol C, Réveret F o, Leymarie J, Gil E, Monier G, Castelluci D and Trassoudaine A 2014 Nano Letters 14 559

12. Ramdani M R, Gil E, Leroux Ch, Andre Y, Trassoudaine A., Castelluci D, Bideux L, Monier G, Robert-Goumet C, and Kupka R 2010 Nano Letters 10 1836

13. Gudiksen M S, Wang J and Lieber C M 2002 The Journal of Physical Chemistry B 106 4036

14. Koblmüller G, Vizbaras K, Hertenberger S, Bolte S, Rudolph D, Becker J, Döblinger M, Amann M-C, Finley J and Abstreiter G 2012 Applied Physics Letters 101 053103

15. Dresselhaus M S, Chen G, Tang M Y, Yang R G, Lee H, Wang D Z, Gogna P 2007 Advanced Materials 19 1043-1053.

16 Zhang Y-Y, Fan G-H, Yin Y-A and Yao G-R 2012 Opt. Express 20 A133-40

17 Chang-Chun, G., Guang-Han, F., Yun-Yan, Z., Yi-Qin, X., Xiao-Ping, L., Shu-Wen, Z. De-Tao, Z. 2012 Chinese Physics B, 21(6), 68505-68508.

18. Yoshimura M, Tomioka K, Hiruma K, Hara S, Motohisa J and Fukui T 2011 Journal of Crystal Growth 315 148

19. Biermanns A, Breuer S, Trampert A, Davydok A, Geelhaar L and Pietsch U 2012 Nanotechnology 23 305703

20. Tomioka K, Motohisa J, Hara S and Fukui T 2008 Nano Letters 8 3475

21. Tomioka K, Tanaka T, Hara S, Hiruma K and Fukui T 2011 Selected Topics in Quantum Electronics, IEEE Journal of 17 1112

22. Tomioka K, Yoshimura M and Fukui T 2013 Nano Letters 13 5822

23. Chen S, Tang M, Jiang Q, Wu J, Dorogan V G, Benamara M, Mazur Y I, Salamo G J, Smowton P and Seeds A 2014 ACS Photonics 1 638

24. Chen S, Tang M, Wu J, Jiang Q, Dorogan V, Benamara M, Mazur Y, Salamo G, Seeds A and Liu H 2014 Electronics Letters 50

25. Wang T, Lee A, Tutu F, Seeds A, Liu H, Jiang Q, Groom K and Hogg R 2012 Applied

Physics Letters 100 052113

26. Roelkens G, Liu L, Liang D, Jones R, Fang A, Koch B and Bowers J 2010 Laser & Photonics Reviews 4 751

27. Mathine D L 1997 IEEE J. Sel. Top. Quantum Electron. 3 952

28. Wu J, Lee A, Jiang Q, Tang M, Seeds A J and Liu H 2014 IET Optoelectronics 8 20

29. Tang M, Chen S, Wu J, Jiang Q, Dorogan V G, Benamara M, Mazur Y I, Salamo G J, Seeds A and Liu H 2014 Optics Express 22 11528

30. Vurgaftman I, Meyer J and Ram-Mohan L 2001 Journal of Applied Physics 89 5815

31. Lee A, Jiang Q, Tang M, Seeds A and Liu H 2012 Optics Express 20 22181

32. Lee A, Liu H and Seeds A 2013 Semiconductor Science and Technology 28 015027

33. Liu H, Wang T, Jiang Q, Hogg R, Tutu F, Pozzi F and Seeds A 2011 Nature Photonics 5 416

34. Chen S, Tang M, Wu J, Jiang Q, Dorogan V, Benamara M, Mazur Y, Salamo G, Seeds A and Liu H 2014 Electronics Letters 50 1467

35. Grassman T J, Brenner M R, Gonzalez M, Carlin A M, Unocic R R, Dehoff R R, Mills M J and Ringel S A 2010 Electron Devices, IEEE Transactions on 57 3361

36. Yamaguchi M and Amano C 1985 Journal of Applied Physics 58 3601

37. Johansson J and Dick K A 2011 CrystEngComm 13 7175

38. Ikejiri K, Ishizaka F, Tomioka K and Fukui T 2013 Nanotechnology 24 115304

39. Munshi A M, Dheeraj D L, Fauske V T, Kim D-C, van Helvoort A T, Fimland B-O and Weman H 2012 Nano Letters 12 4570

40. Hong Y J, Lee W H, Wu Y, Ruoff R S and Fukui T 2012 Nano Letters 12 1431

41. Mohseni P K, Lawson G, Couteau C, Weihs G, Adronov A and LaPierre R R 2008 Nano Letters 8 4075

42. Cohin Y, Mauguin O, Largeau L, Patriarche G, Glas F, Søndergård E and Harmand J-C 2013 Nano Letters 13 2743

43. Lohn A J, Li X and Kobayashi N P 2011 Journal of Crystal Growth 315 157

44. Dhaka V, Haggren T, Jussila H, Jiang H, Kauppinen E, Huhtio T, Sopanen M and Lipsanen H 2012 Nano Letters 12 1912

45. Novotny C J, Yu E T and Yu P K 2008 Nano Letters 8 775

46. Larsson M W, Wagner J B, Wallin M, Håkansson P, Fröberg L E, Samuelson L and Wallenberg L R 2007 Nanotechnology 18 015504

47. Ercolani D, Rossi F, Li A, Roddaro S, Grillo V, Salviati G, Beltram F and Sorba L 2009 Nanotechnology 20 505605

48. Ye H, Lu P, Yu Z, Song Y, Wang D and Wang S 2009 Nano Letters 9 1921

49. Glas F 2006 Physical Review B 74 121302

50. Zhang G, Tateno K, Gotoh H, Sogawa T and Nakano H 2010 Japanese Journal of Applied Physics 49 015001

51. de la Mata M, Magén C, Caroff P and Arbiol J 2014 Nano Letters 14 6614

52. Jabeen F, Patriarche G, Glas F and Harmand J-C 2011 Journal of Crystal Growth 323 2

53. Caroff P, Messing M E, Borg B M, Dick K A, Deppert K and Wernersson L-E 2009 Nanotechnology 20 495606

54. Caroff P, Wagner J B, Dick K A, Nilsson H A, Jeppsson M, Deppert K, Samuelson L, Wallenberg L and Wernersson L E 2008 Small 4 878

55. Plissard S, Dick K, Wallart X and Caroff P 2010 Applied Physics Letters 96 121901

56. Caroff P, Messing M E, Borg B M, Dick K A, Deppert K and Wernersson L-E 2009 Nanotechnology 20 495606

57. Hocevar M, Immink G, Verheijen M, Akopian N, Zwiller V, Kouwenhoven L and Bakkers E 2012 Nature Communications 3 1266

58. Schuster F, Laumer B, Zamani R R, Magén C, Morante J R, Arbiol J and Stutzmann M 2014 ACS Nano 8 4376

59. Liu H, Steer M, Badcock T, Mowbray D, Skolnick M, Suarez F, Ng J, Hopkinson M and David J 2006 Journal of Applied Physics 99 046104

60. Liu H, Sellers I, Badcock T, Mowbray D, Skolnick M, Groom K, Gutierrez M, Hopkinson

M, Ng J and David J 2004 Applied Physics Letters 85 704

61. Biermanns A, Rieger T, Bussone G, Pietsch U, Grützmacher D and Lepsa M I 2013 Applied Physics Letters 102 043109

62. Grönqvist J, Søndergaard N, Boxberg F, Guhr T, Åberg S and Xu H 2009 Journal of Applied Physics 106 053508

63. Søndergaard N, He Y, Fan C, Han R, Guhr T and Xu H 2009 Journal of Vacuum Science & Technology B 27 827

64. Hilse M, Takagaki Y, Ramsteiner M, Herfort J, Breuer S, Geelhaar L and Riechert H 2011 Journal of Crystal Growth 323 307

65. Sköld N, Karlsson L S, Larsson M W, Pistol M-E, Seifert W, Trägårdh J and Samuelson L 2005 Nano Letters 5 1943

66. Montazeri M, Fickenscher M, Smith L M, Jackson H E, Yarrison-Rice J, Kang J H, Gao Q, Tan H H, Jagadish C and Guo Y 2010 Nano Letters 10 880

67. Raychaudhuri S and Yu E 2006 Journal of Applied Physics 99 114308

68. Raychaudhuri S and Yu E 2006 Journal of Vacuum Science & Technology B 24 2053

69. Nazarenko M V, Sibirev N V, Ng K W, Ren F, Ko W S, Dubrovskii V G and Chang-Hasnain C 2013 Journal of Applied Physics 113 104311

70. Lu L-X, Bharathi M and Zhang Y-W 2013 Nano Letters 13 538

71. Yan X, Zhang X, Ren X, Huang H, Guo J, Guo X, Huang Y 2011Nano Letters 11 3941

72. Li X and Yang G 2009 The Journal of Physical Chemistry C 113 12402

73. Guo J, Huang H, Zhang J, Li X, Huang Y, Ren X, Ji Z and Liu M 2013 Journal of Applied Physics 113 114301

74. Yan X, Zhang X, Ren X, Li J, Lv X, Wang Q and Huang Y 2012 Applied Physics Letters 101 023106

75. Joyce B A, Sudijono J L, Belk J G, Yamaguchi H, Zhang X M, Dobbs H T, Zangwill A, Vvedensky D D and Jones T S 1997 Japanese Journal of Applied Physics 36 4111

76. Belk J G, Pashley D W, McConville C F, Sudijono J L, Joyce B A and Jones T S 1997

Physical Review B 56 10289

77. Uccelli E, Arbiol J, Morante J R and Fontcuberta i Morral A 2010 ACS Nano 4 5985

78. Assali S, Zardo I, Plissard S, Kriegner D, Verheijen M, Bauer G, Meijerink A, Belabbes A, Bechstedt F and Haverkort J 2013 Nano Letters 13 1559

79. Wilhelm C, Larrue A, Dai X, Migas D and Soci C 2012 Nanoscale 4 1446

80. Mishra A, Titova L, Hoang T, Jackson H, Smith L, Yarrison-Rice J, Kim Y, Joyce H, Gao Q and Tan H 2007 Applied Physics Letters 91 263104

81. Ba Hoang T, Moses A F, Ahtapodov L, Zhou H, Dheeraj D L, van Helvoort A T, Fimland B-O and Weman H 2010 Nano Letters 10 2927

82. Wang J, Gudiksen M S, Duan X, Cui Y and Lieber C M 2001 Science 293 1455

83. Smith L M, Jackson H E, Yarrison-Rice J M and Jagadish C 2010 Semiconductor Science and Technology 25 024010

84. Hoang T B, Moses A, Zhou H, Dheeraj D, Fimland B and Weman H 2009 Applied Physics Letters 94 133105

85. Trägårdh J, Persson A, Wagner J, Hessman D and Samuelson L 2007 Journal of Applied Physics 101 123701

86. Murayama M and Nakayama T 1994 Physical Review B 49 4710

87. Akopian N, Patriarche G, Liu L, Harmand J-C and Zwiller V 2010 Nano Letters 10 1198

88. Joyce H J, Wong-Leung J, Yong C-K, Docherty C J, Paiman S, Gao Q, Tan H H, Jagadish C, Lloyd-Hughes J and Herz L M 2012 Nano Letters 12 5325

89. Couto Jr O, Sercombe D, Puebla J, Otubo L, Luxmoore I, Sich M, Elliott T, Chekhovich E, Wilson L and Skolnick M 2012 Nano Letters 12 5269

90. Schroer M and Petta J 2010 Nano Letters 10 1618

91. Ikonić Z, Srivastava G and Inkson J 1993 Physical Review B 48 17181

92. Stiles M and Hamann D 1988 Physical Review B 38 2021

93. Thelander C, Caroff P, Plissard S, Dey A W and Dick K A 2011 Nano Letters 11 2424

94. Sourribes M J, Isakov I, Panfilova M, Liu H and Warburton P A 2014 Nano Letters 14

1643

95. Parkinson P, Joyce H J, Gao Q, Tan H H, Zhang X, Zou J, Jagadish C, Herz L M and Johnston M B 2009 Nano Letters 9 3349

96. Wallentin J, Ek M, Wallenberg L R, Samuelson L and Borgström M T 2011 Nano Letters 12 151

97. Wang G T, Li Q, Wierer J J, Koleske D D and Figiel J J 2014 Physica Status Solidi (a) 211 748

98. Hobbs R G, Petkov N and Holmes J D 2012 Chemistry of Materials 24 1975

99. Dhindsa N, Chia A, Boulanger J, Khodadad I, LaPierre R and Saini S S 2014 Nanotechnology 25 305303

100. Morales A M and Lieber C M 1998 Science 279 208

101. Noborisaka J, Motohisa J and Fukui T 2005 Applied Physics Letters 86 213102

102. Jensen L E, Björk M T, Jeppesen S, Persson A I, Ohlsson B J and Samuelson L 2004 Nano Letters 4 1961

103. Zhang Y, Aagesen M, Holm J V, Jørgensen H I, Wu J and Liu H 2013 Nano Letters 13 3897

104. Li N, Tan T Y and Gösele U 2008 Applied Physics A 90 591

105. Dick K A, Deppert K, Samuelson L, Wallenberg L R and Ross F M 2008 Nano Letters 8 4087

106. Tomioka K, Kobayashi Y, Motohisa J, Hara S and Fukui T 2009 Nanotechnology 20 145302

107. Lundskog A, Forsberg U, Holtz P O, Janzén E 2012 Crystal Growth & Design, 12, 5491

108. Dick K A 2008 Progress in Crystal Growth and Characterization of Materials 54 138

109. Dick K A and Caroff P 2014 Nanoscale 6 3006

110. Munshi A M, Dheeraj D L, Fauske V T, Kim D-C, Huh J, Reinertsen J F, Ahtapodov L, Lee K, Heidari B and Van Helvoort A 2014 Nano Letters 14 960

111. Dick K A and Caroff P 2014 Nanoscale 6 3006

112. Wu Y and Yang P 2001 Journal of the American Chemical Society 123 3165

113. Joyce H J, Gao Q, Tan H H, Jagadish C, Kim Y, Zhang X, Guo Y and Zou J 2007 Nano Letters 7 921

114. Jacobsson D, Persson J M, Kriegner D, Etzelstorfer T, Wallentin J, Wagner J B, Stangl J, Samuelson L, Deppert K and Borgström M 2012 Nanotechnology 23 245601

115. Jung C S, Kim H S, Jung G B, Gong K J, Cho Y J, Jang S Y, Kim C H, Lee C-W and Park J 2011 The Journal of Physical Chemistry C 115 7843

116. Regolin I, Khorenko V, Prost W, Tegude F-J, Sudfeld D, Kästner J and Dumpich G 2006 Journal of Applied Physics 100 074321

117. Gorji Ghalamestani S, Ek M, Ganjipour B, Thelander C, Johansson J, Caroff P and Dick K A 2012 Nano Letters 12 4914

118. Ek M, Borg B M, Dey A W, Ganjipour B, Thelander C, Wernersson L-E and Dick K A 2011 Crystal Growth & Design 11 4588

119. Borg B M, Dick K A, Ganjipour B, Pistol M-E, Wernersson L-E and Thelander C 2010 Nano Letters 10 4080

120. Dey A W, Svensson J, Borg B M, Ek M and Wernersson L-E 2012 Nano Letters 12 5593

121. van Weert M H, Helman A, van den Einden W, Algra R E, Verheijen M A, Borgstrom M T, Immink G, Kelly J J, Kouwenhoven L P and Bakkers E P 2009 Journal of the American Chemical Society 131 4578

122. Bar-Sadan M, Barthel J, Shtrikman H and Houben L 2012 Nano Letters 12 2352

123. Breuer S, Pfüller C, Flissikowski T, Brandt O, Grahn H T, Geelhaar L and Riechert H 2011 Nano Letters 11 1276

124. Perea D E, Allen J E, May S J, Wessels B W, Seidman D N and Lauhon L J 2006 Nano Letters 6 181

125. Jiang N, Gao Q, Parkinson P, Wong-Leung J, Mokkapati S, Breuer S, Tan H H, Zheng C L, Etheridge J and Jagadish C 2013 Nano Letters 13 5135

126. Ahtapodov L, Todorovic J, Olk P, Mjåland T, Slåttnes P, Dheeraj D L, van Helvoort A T, Fimland B-O and Weman H 2012 Nano Letters 12 6090

127. Mohseni P K and LaPierre R R 2009 Nanotechnology 20 025610

128. Kim Y, Joyce H J, Gao Q, Tan H H, Jagadish C, Paladugu M, Zou J and Suvorova A A 2006 Nano Letters 6 599

129. Paek J, Yamaguchi M and Amano H 2011 Journal of Crystal Growth 323 315

130. Heiss M, Ketterer B, Uccelli E, Morante J R, Arbiol J and i Morral A F 2011 Nanotechnology 22 195601

131. Plissard S, Dick K, Wallart X and Caroff P 2010 Applied Physics Letters 96 121901

132. to T 1998 Japanese Journal of Applied Physics 37 L1217

133. Akiyama T, Sano K, Nakamura K and Ito T 2006 Japanese Journal of Applied Physics 45 L275

134. Bukała M, Galicka M, Buczko R, Kacman P, Shtrikman H, Popovitz-Biro R, Kretinin A and Heiblum M 2010 In PHYSICS OF SEMICONDUCTORS: 29th International Conference on the Physics of Semiconductors 349

135. Caroff P, Bolinsson J and Johansson J 2011 Selected Topics in Quantum Electronics, IEEE Journal of 17 829

136. Dick K A, Caroff P, Bolinsson J, Messing M E, Johansson J, Deppert K, Wallenberg L R and Samuelson L 2010 Semiconductor Science and Technology 25 024009

137. Conesa-Boj S n, Kriegner D, Han X-L, Plissard S b, Wallart X, Stangl J, Fontcuberta i Morral A and Caroff P 2013 Nano Letters 14 326

138. Xu T, Dick K A, Plissard S, Nguyen T H, Makoudi Y, Berthe M, Nys J-P, Wallart X, Grandidier B and Caroff P 2012 Nanotechnology 23 095702

139. Zhang Z, Zheng K, Lu Z-Y, Chen P-P, Lu W and Zou J 2015 Nano Letters15 876.

140. Wang J, Plissard S, Hocevar M, Vu T T, Zehender T, Immink G G, Verheijen M A, Haverkort J and Bakkers E P 2012 Applied Physics Letters 100 053107

141. Krishnamachari U, Borgstrom M, Ohlsson B, Panev N, Samuelson L, Seifert W, Larsson

M and Wallenberg L 2004 Applied Physics Letters 85 2077

142. Fonseka H A, Caroff P, Wong-Leung J, Ameruddin A S, Tan H H and Jagadish C 2014 ACS Nano 8 6945

143. Wu Z, Mei X, Kim D, Blumin M, Ruda H, Liu J and Kavanagh K 2003 Applied Physics Letters 83 3368

144. Xu H, Wang Y, Guo Y, Liao Z, Gao Q, Tan H H, Jagadish C and Zou J 2012 Nano Letters 12 5744

145. Wacaser B A, Deppert K, Karlsson L S, Samuelson L and Seifert W 2006 Journal of Crystal Growth 287 504

146. Wang J, Plissard S b R, Verheijen M A, Feiner L-F, Cavalli A and Bakkers E P 2013 Nano Letters 13 3802

147. Caroff P, Dick K A, Johansson J, Messing M, Deppert K and Samuelson L 2009 Nature Nanotechnology 4 50

148. BukaŁa M, Galicka M, Buczko R and Kacman P 2010 Physica E: Low-dimensional Systems and Nanostructures 42 795

149. Sano K, Akiyama T, Nakamura K and Ito T 2007 Journal of Crystal Growth 301 862-865

150. Dubrovskii V and Sibirev N 2008 Physical Review B 77 035414

151. Glas F, Harmand J-C and Patriarche G 2007 Physical Review Letters 99 146101

152. Dubrovskii V, Sibirev N, Harmand J and Glas F 2008 Physical Review B 78 235301

153. Johansson J, Dick K, Caroff P, Messing M, Bolinsson J, Deppert K and Samuelson L 2010 The Journal of Physical Chemistry C 114 3837

154. Glas F 2010 Journal of Applied Physics 108 073506

155. Dubrovskii V 2014 Applied Physics Letters 104 053110

156 Johansson J, Karlsson L S, Dick K A, Bolinsson J, Wacaser B A, Deppert K and Samuelson L 2008 Crystal Growth and Design 9 766

157. Paiman S, Gao Q, Tan H, Jagadish C, Zhang X and Zou J 2013 Journal of Crystal Growth 383 100

158. Joyce H J, Gao Q, Tan H H, Jagadish C, Kim Y, Fickenscher M A, Perera S, Hoang T B, Smith L M and Jackson H E 2008 Nano Letters 9 695

159. Gil E, Dubrovskii V G, Avit G, André Y, Leroux C, Lekhal K, Grecenkov J, Trassoudaine A s, Castelluci D and Monier G 2014 Nano Letters 14 3938

160. Dheeraj D, Munshi A, Scheffler M, van Helvoort A, Weman H and Fimland B 2013 Nanotechnology 24 015601

161. Lehmann S, Wallentin J, Jacobsson D, Deppert K and Dick K A 2013 Nano Letters 13 4099

162. Wallentin J, Ek M, Wallenberg L R, Samuelson L, Deppert K and Borgström M T 2010 Nano Letters 10 4807

163. Algra R E, Verheijen M A, Borgström M T, Feiner L-F, Immink G, van Enckevort W J, Vlieg E and Bakkers E P 2008 Nature 456 369

164. Kawaguchi K, Sudo H, Matsuda M, Ekawa M, Yamamoto T and Arakawa Y 2014 Applied Physics Letters 104 063102

165. Wallentin J, Persson J M, Wagner J B, Samuelson L, Deppert K and Borgström M T 2010 Nano Letters 10 974

166. Joyce H J, Wong-Leung J, Gao Q, Tan H H and Jagadish C 2010 Nano Letters 10 908

167. Krogstrup P, Curiotto S, Johnson E, Aagesen M, Nygård J and Chatain D 2011 Physical Review Letters 106 125505

168. Rieger T, Lepsa M I, Schäpers T and Grützmacher D 2013 Journal of Crystal Growth 378 506

169. Munshi A M, Dheeraj D L, Todorovic J, van Helvoort A T, Weman H and Fimland B-O 2013 Journal of Crystal Growth 372 163

170. Yu X, Wang H, Lu J, Zhao J, Misuraca J, Xiong P and von Molnár S 2012 Nano Letters 12 5436

171. Lam P, Wu J, Tang M, Jiang Q, Hatch S, Beanland R, Wilson J, Allison R and Liu H

2014 Solar Energy Materials and Solar Cells 126 83

172. Walter M G, Warren E L, McKone J R, Boettcher S W, Mi Q, Santori E A and Lewis N S 2010 Chemical Reviews 110 6446

173. Cao L, White J S, Park J-S, Schuller J A, Clemens B M and Brongersma M L 2009 Nature Materials 8 643

174. Krogstrup P, Jørgensen H I, Heiss M, Demichel O, Holm J V, Aagesen M, Nygard J and i Morral A F 2013 Nature Photonics 7 306

175. Zhang J, Dhindsa N, Chia A, Boulanger J, Khodadad I, Saini S and LaPierre R 2014 Applied Physics Letters 105 123113

176. Anttu N, Lehmann S, Storm K, Dick K A, Samuelson L, Wu P M and Pistol M-E 2014 Nano Letters 14 5650

177. Hu Y, Li M, He J and LaPierre R 2013 Nanotechnology 24 065402

178. Wu P M, Anttu N, Xu H, Samuelson L and Pistol M-E 2012 Nano Letters 12 1990

179. Dai Y-A, Chang H-C, Lai K-Y, Lin C-A, Chung R-J, Lin G-R and He J-H 2010 Journal of Materials Chemistry 20 10924

180. Diedenhofen S L, Janssen O T, Grzela G, Bakkers E P and Gómez Rivas J 2011 ACS Nano 5 2316

181. Huang N, Lin C and Povinelli M L 2012 Journal of Applied Physics 112 064321

182. Hu L and Chen G 2007 Nano Letters 7 3249

183. Zhu J, Hsu C-M, Yu Z, Fan S and Cui Y 2009 Nano Letters 10 1979

184. Rayleigh L 1879 Proceedings of the London Mathematical Society 1 51

185. Maskens O L, Rivas J G, Algra R E, Bakkers E P and Lagendijk A 2008 Nano Letters 8 2638

186. Maskens O L, Diedenhofen S L, Kaas B C, Algra R E, Bakkers E P, Gómez Rivas J and Lagendijk A 2009 Nano Letters 9 930

187. Strudley T, Zehender T, Blejean C, Bakkers E P and Maskens O L 2013 Nature Photonics 7 413

188. Callahan D M, Munday J N and Atwater H A 2012 Nano Letters 12 214

189. Saeta P N, Ferry V E, Pacifici D, Munday J N and Atwater H A 2009 Optics Express 17 20975

190. Yablonovitch E 1982 JOSA 72 899

191. Yablonovitch E and Cody G D 1982 Electron Devices, IEEE Transactions on 29 300-305

192 Garnett E and Yang P 2010 Nano Letters 10 1082

193. Zhu J, Yu Z, Fan S and Cui Y 2010 Materials Science and Engineering: R: Reports 70 330

194. Wen L, Zhao Z, Li X, Shen Y, Guo H and Wang Y 2011 Applied Physics Letters 99 143116

195 Wallentin J, Anttu N, Asoli D, Huffman M, Åberg I, Magnusson M H, Siefer G, Fuss-Kailuweit P, Dimroth F and Witzigmann B 2013 Science 339 1057

196. Kayes B M, Atwater H A and Lewis N S 2005 Journal of Applied Physics 97 114302

197. Lam P, Hatch S, Wu J, Tang M, Dorogan V G, Mazur Y I, Salamo G J, Ramiro I, Seeds A and Liu H 2014 Nano Energy 6 159

198. Hatch S, Wu J, Sablon K, Lam P, Tang M, Jiang Q and Liu H 2014 Optics Express 22 A679

199. Shin J C, Kim K H, Yu K J, Hu H, Yin L, Ning C-Z, Rogers J A, Zuo J-M and Li X 2011 Nano Letters 11 4831

200. Gutsche C, Lysov A, Braam D, Regolin I, Keller G, Li Z A, Geller M, Spasova M, Prost W and Tegude F J 2012 Advanced Functional Materials 22 929

201. Shin J C, Lee A, Katal Mohseni P, Kim D Y, Yu L, Kim J H, Kim H J, Choi W J, Wasserman D and Choi K J 2013 ACS Nano 7 5463

202. Holm J V, Jørgensen H I, Krogstrup P, Nygård J, Liu H and Aagesen M 2013 Nature Communications 4 1498

203. Dong Y, Tian B, Kempa T J and Lieber C M 2009 Nano Letters 9 2183

204. Foster A P and Wilson L R 2013 Physica Status Solidi (a) 210 425

205. LaPierre R 2011 Journal of Applied Physics 110 014310

206. Heurlin M, Wickert P, Fält S, Borgström M T, Deppert K, Samuelson L and Magnusson M H 2011 Nano Letters 11 2028

207. Heiss M and i Morral A F 2011 Applied Physics Letters 99 263102

208. Heiss M, Russo-Averchi E, Dalmau-Mallorquí A, Tütüncüoğlu G, Matteini F, Rüffer D, Conesa-Boj S, Demichel O, Alarcon-Lladó E and i Morral A F 2014 Nanotechnology 25 014015

209. Mohseni P K, Behnam A, Wood J D, Zhao X, Yu K J, Wang N C, Rockett A, Rogers J A, Lyding J W and Pop E 2014 Advanced Materials 26 3755

210. Chao J-J, Shiu S-C, Hung S-C and Lin C-F 2010 Nanotechnology 21 285203

211 Zhang Y Y, Fan G H and Zhang Y 2011 Acta. Phys. Sin. 60 028503

212 Chen J, Fan G, Pang W, Zheng S, Zhang Y 2012 Chinese Optics Letters 10 (6), 062302

213 Yun-Yan Z and Guang-Han F 2011 Chin. Phys. B 20 048502

214 Zhang Y Y, Fan G H, Zhang T 2012 Quantum Electronics, IEEE Journal of 48 (2), 169

215 Bin-Bin D, Fang Z, Jing-Jing S, Jian-Yong X, Shu-Wen Z, Yun-Yan Z, Yi-Qin Xu, De-Tao Zhou, Xiao-Peng Yu, Han-Xiang Zhang, Tao Zhang, Guang-Han F. 2013. Chinese Physics B, 22(8), 088503.

216 Chen J, Fan G-H, Pang W, Zheng S-W and Zhang Y-Y 2012 IEEE Photon. Technol. Lett. 24 2218 – 20

217. Borgström M T, Zwiller V, Müller E and Imamoglu A 2005 Nano Letters 5 1439

218 Wu J, Zhang Y, Tutu F, Lam P, Hatch S, Liu H 2013 Optics for Solar Energy, RM1D. 1

219 Holm J V, Aagesen M, Zhang Y, Wu J, Hatch S, Liu H (2014, June). In Photovoltaic Specialist Conference (PVSC), 2014 IEEE 40th (pp. 1041-1044). IEEE.

220 Orchard J R, Zhang Y, Wu J, Liu H, Mowbray D 2015, February. In SPIE OPTO International Society for Optics and Photonics. 937308-937308

221. Krames M R, Shchekin O B, Mueller-Mach R, Mueller G O, Zhou L, Harbers G and Craford M G 2007 Display Technology, Journal of 3 160

222. Crawford M H 2009 Selected Topics in Quantum Electronics, IEEE Journal of 15 1028

223. Jun C, Guang-Han F, Yun-Yan Z, Wei P, Shu-Wen Z and Guang-Rui Y 2012 Chinese Physics B 21 058504

224. Zhang Y-Y, Zhu X-L, Yin Y-A and Ma J 2012 Electron Device Letters, IEEE 33 994

225. Yun-Yan Z and Guang-Han F 2011 Chinese Physics B 20 048502

Chapter 2:

Experimental Methods

2.1 Introduction

The self-catalysed NW growth is very sensitive to growth parameters, which gives high requirements for the growth facilities. They need to be able to precisely control a wide range of growth parameters. The molecular beam epitaxy system is able to control the deposition with atomic precision, and hence is highly suitable for the NW growth. For the NW morphology and crystal structure inspection, due to their nanometre size, high resolution imaging equipment is necessary, such as the scanning electron microscope (SEM) and transmission electron microscope (TEM). For the determination of the band gap, the photoluminescence measurement is the first choice. Although these machines are also used in characterizing tradition thin film structures, their operation in NW field is somehow different.

2.2 Molecular Beam Epitaxy (MBE)

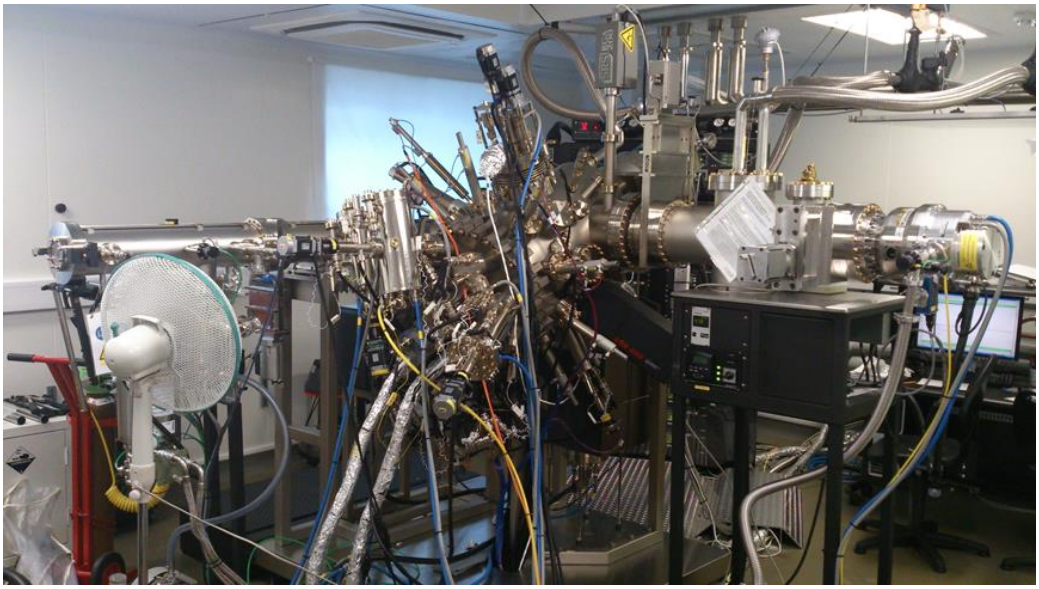

Figure 2-1. Veeco GEN930 MBE.

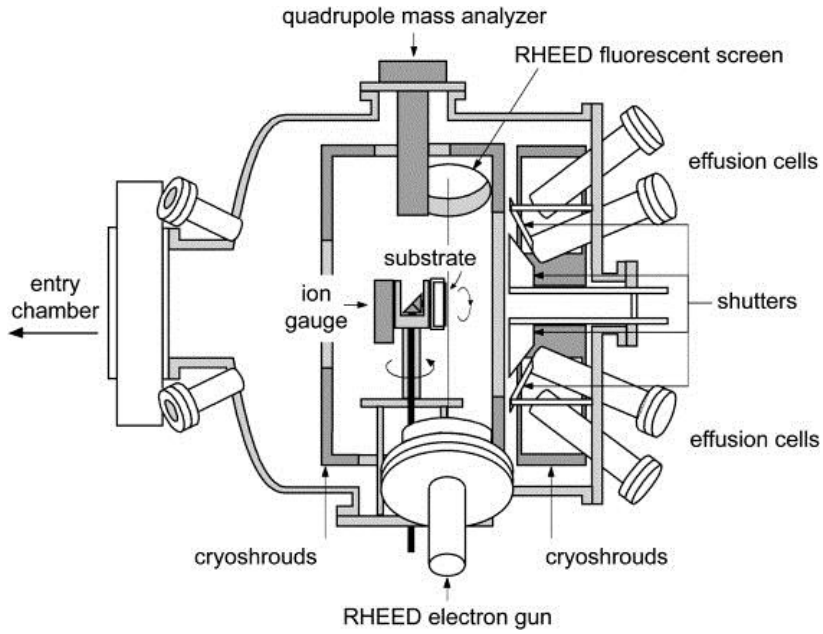

Figure 2-2. Illustration of the structure of the MBE growth chamber. Reprinted from The Lancet, 47. 2-3, S. Franchi,G. Trevisi,L. Seravalli,P. Frigeri, Quantum dot nanostructures and molecular beam epitaxy, 30, Copyright (2003), with permission from Elsevier.[1]

The molecular beam epitaxy system used in our NW growth is GEN930 manufactured

by Veeco (Fig. 2-1). Its simplified structure is illustrated in Fig. 2-2. This system has four vacuum chambers that are the Loadlock Chamber, the Prep Chamber, Phosphorus recovery system, and the Growth Chamber (Fig. 2-3). All the chambers are separated with an ultra-high vacuum (UHV) gate valve, which prevents the inter-chamber cross-contamination of background gas.

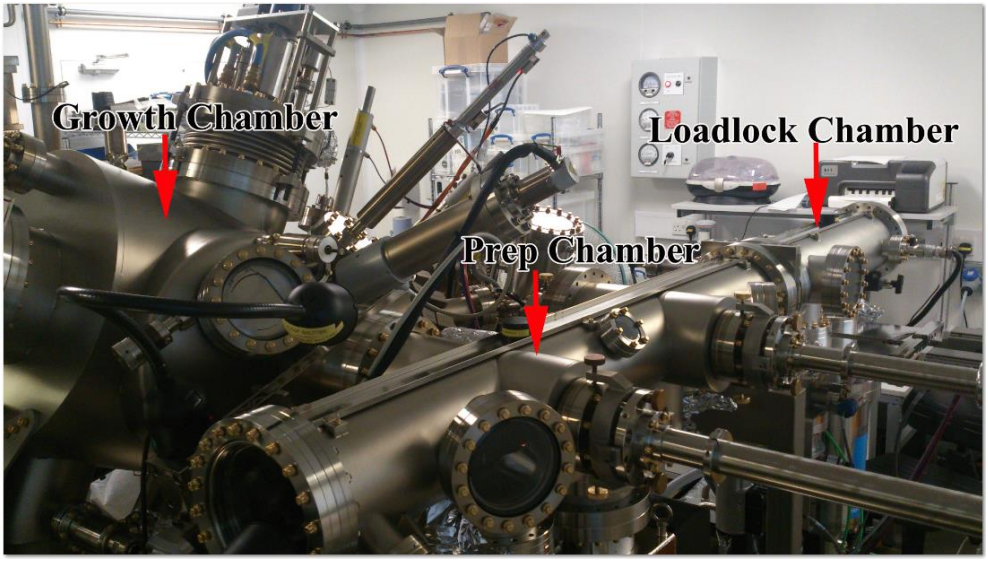

Figure 2-3. Growth, prep and loadlock chamber of the Veeco GEN930 MBE.

The Loadlock Chamber is used for loading and unloading substrates and samples in and out of the MBE, while keeping the ultra-high vacuum in the two other chambers. In this chamber, there are two quartz infrared (IR) tube lamps mounted on the sidewalls. When a new sample is loaded into the Loadlock Chamber, a preliminary outgas is performed. During the outgas process, the lamps heat the chamber to 100-200 °C, [2] which can greatly reduce the water vapour and other volatile contaminants. Usually in the Loadlock Chamber the rough pumping system includes a turbo pump and a scroll backing pump. The scroll pump is the backing of the turbo pump. The turbo pump can also maintain the chamber pressure in the

high vacuum region. This pump combination is commonly used for rough pumping all the chambers from atmosphere to high-vacuum pressure levels. In addition to the turbo pump, a cryopump is also attached to the Loadlock Chamber to provide better vacuum capability. But the rough pumping is still done by the turbo pump combination, because the cryopump is only opened at comparatively high vacuum level.

The Prep Chamber is a buffer chamber to provide a UHV clean environment between the Growth Chamber and the Loadlock Chamber. Similar to the Loadlock Chamber, the Prep Chamber also has a heating stage on the sidewalls, which can be heated up to 600^{o}C. A pre-growth substrate degassing can be performed and can drive off almost all the evaporable residual contaminants, such as water or hydrocarbons. It can also be used to remove substrate oxide, although most growers prefer doing it in the Growth Chamber. Because this heater is separated from the one in the Growth Chamber, the substrate degassing can be carried out in parallel to the sample growth. Therefore, the Prep Chamber serves as substrate preparation chamber for growth. Moreover, the Prep Chamber can act as a storage chamber for wafers before and after the growth. The rough pumping of the Prep Chamber is normally done through the Loadlock Chamber. Therefore, it does not have a rough pumping system. Instead, it has an ion pump, integrated with a titanium sublimation pump (TSP). However, this integrated pump is a standard UHV pump and needs the chamber to reach a high-vacuum level before it can be started.

The Growth Chamber is where the wafer growth happens. It includes a substrate manipulator, substrate heater, thermocouple, various effusion cells, cryopanels, vacuum facilities and analytical instruments. The substrate manipulator holds wafers during the

growth and can be moved along two axes (Fig. 2-4). One axis is the indexing, which is to position the gauge for beam flux measurement, and the substrate for growth and transfer. The second axis is for the wafer to rotate along its own axis, which is beneficial for achieving a uniform growth across the entire wafer. The substrate heater has a wound wire heating filament inside that can heat the substrate to a temperature higher than 1000 °C.[2] In order to measure the wafer temperature during the growth, a thermocouple and a pyrometer are used. The thermocouple is right behind, but not touching, the substrate and shielded from the heater filament to improve its accuracy and stability. The pyrometer is right facing the front surface of the wafer when it is at the growth position. Because it detects the optical emission from wafers, it is normally positioned outside the chamber and collects the wafer emission through an optical viewport (Fig. 2-5). In order to improve the measurement accuracy, the pyrometer, the optical viewport and the wafer are arranged along the centre axis of the Growth Chamber. In the chamber, the effusion cells are attached with a common focal point where the sample is positioned during the sample growth. In our solid-source system, we have Al, Ga, In, P, As, Sb, Si and Be sources. The effusion cells are separated by a cryopanel. Inside the cryopanel a coolant is running, such as liquid nitrogen, water or water/alcohol solution. Therefore, by controlling the temperature, the cryopanel can provide a stable environment for cells, which is beneficial for the independent and precise cell temperature control by avoiding the cross-interaction of the cell heat. The vacuum level of this chamber is critical for achieving good growth quality. The cryogenic pump is a good choice, because it can provide high-speed and high-capacity pumping for a wide range of gas species. But this is a close-end pump and needs to be regenerated regularly by pumping out the trapped gasses. The ion pump and the

TSP pump are also attached to the Growth Chamber, because they are very effective at pumping out a wide range of active and noble element vapours.

For our MBE with the capability to grow phosphides, pumping out the residue gas is much more complex. The direct venting out of the phosphorus-containing residue gas can cause serious environmental pollution and is a safety hazard. Therefore, a phosphorus recovery system is needed to deal with the phosphorus residues (Fig. 2-6). This system has a LN_2 cooled trapping well, which is backed by a turbo-molecular pump and a scroll pump in sequence. This combination can greatly slow down the exposure of the phosphorus to oxygen, making the phosphorus oxidization process safer.

In order to control and monitor the chamber condition, especially during the growth, a wide range of highly-sensitive analytical instruments are used. The ion vacuum gauges are used to measure the chamber vacuum level. They are hot-filament Bayard-Alpert type and mounted in a nude configuration (Fig. 2-7). The low-pressure limit of the ion gauges is about 2×10^{-11} Torr.[2] Besides, the ion vacuum gauges can also be used to measure the beam equivalent pressure, which is critical for the growth parameter control. During the growth, the Reflective High Energy Electron Diffraction (RHEED) system is widely used for the in-situ inspection of wafer growths. The electron beam grazes over the wafer surface with a low-impingement angle trajectory. The diffracted electrons contain the crystallographic information, such as the surface reconstruction. This can be used to determine the growth conditions, such as to know if the growth is under group-V-rich or group-III-rich environment. Moreover, the morphological information can also be obtained by RHEED, such as the flatness. This can help monitor the growth modes, such as the 0D QD growth or the 2D thin

film growth. For the thin film growth, the intensity oscillation of the RHEED pattern can be used to extract the deposition rate of elements. The MBE growth requires a UHV and the epitaxy quality is quite sensitive to the background contamination. The residual gas analysis (RGA) can be used to monitor the background by analysing the mass-to-charge ratio of the ionized gas molecules.

Figure 2-4 Substrate manipulator.

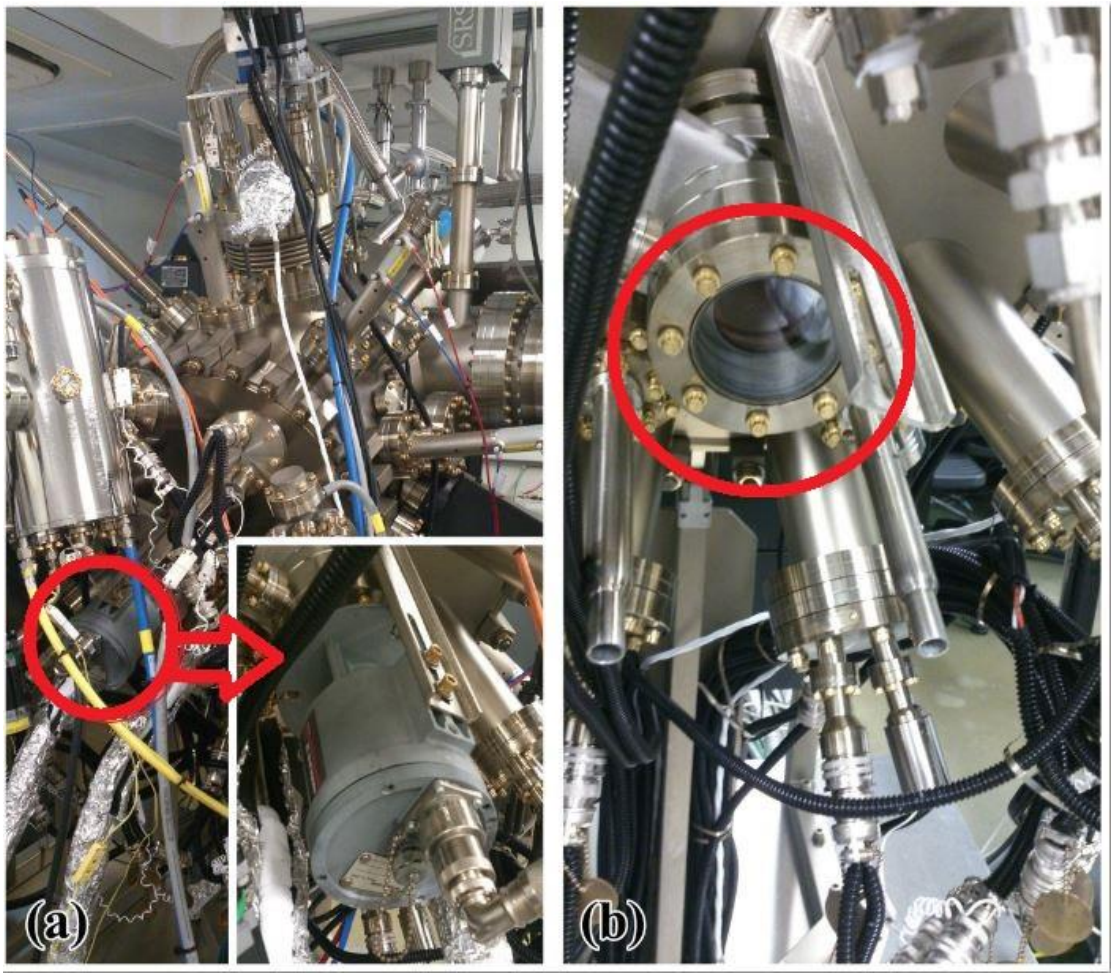

Figure 2-5 Pyrometer and the viewport marked by the red circles.

Figure 2-6. Phosphorus recovery system.

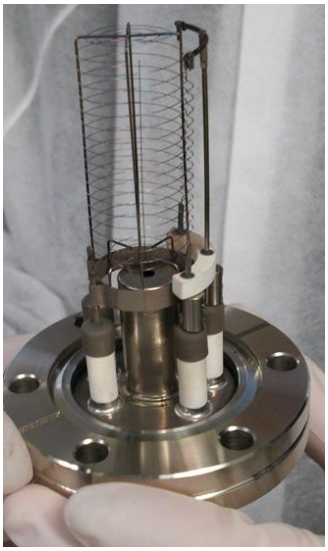

Figure 2-7. Ion gauge.

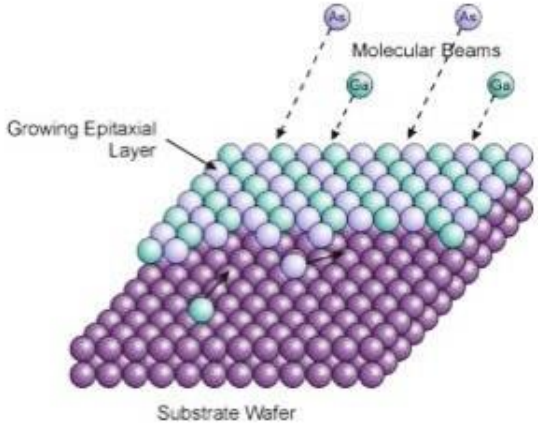

Figure 2-8. Illustration of the MBE epitaxial growth.

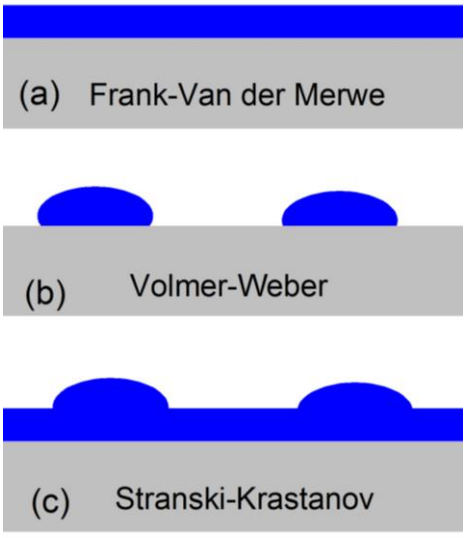

Figure 2-9. Illustration of three different epitaxial growth modes.

During the MBE epitaxial growth, group-III and V fluxes arrive at the surface of the heated substrates with a rectilinear motion under the UHV environment. Following the lattice template of the crystal substrates, the group-III and V adatoms bond with each other to carry out the epitaxy (Fig. 2-8). Depending on the lattice strain and free energy of interfaces, the thin film growth can adopt three different growth modes, namely Frank-Van der Merwe (layer mode), Volmer-Weber (Island mode), and Stranski-Krastanov (Layer plus island mode).[3,4]

By defining the free energy of the film surface, interface, and substrate as E_{film}, E_{int} and E_{sub}, respectively, the energy change during the epitaxial growth is:

$$\Delta E = E_{film} + E_{int} - E_{sub} \qquad 2\text{-}1$$

When the $\Delta E \leq 0$, the epitaxial growth tends to follow the layer-by-layer growth mode (Fig. 2-9a). When the $\Delta E > 0$, the epitaxial growth prefers to follow the island growth mode (Fig. 2-9b). For some special cases, the ΔE can change with the increase of the growth thickness of epitaxial layers. For example, when the growth is between lattice mismatched materials, the strain accumulation can increase the E_{film}. In this case, when the epitaxial film thickness is small, the growth follows the layer-by-layer growth mode due to the $\Delta E \leq 0$, but it switches to the island growth mode when the thickness is large enough to make the $\Delta E > 0$. This growth is illustrated in Fig. 2-9c, which is commonly used for the quantum dot growth, such as the InAs dot on GaAs.[5]

2.3 Scanning Electron Microscope (SEM)

NWs are typically nanometre in diameter. The optical apparatus are useless in measuring the morphology, because their resolution is limited by the wavelength of visible light

(300-800nm). Therefore, an electron microscope needs to be used (Fig. 2-10). The electron microscope uses electrons as the detecting probe. The de Broglie wavelength of an electron is $\lambda=h/p$, where h is the Planck constant and p is the momentum of the electron. According to this equation, an electron with a kinetic energy of 100 eV can have a wavelength of only 0.12 nm, which is almost the size of an atom. Therefore, the resolution of the electron microscope can reach sub-nanometre size, which is suitable for obtaining the NW morphology information.

During the measurement, electron beam is emitted from an electron gun by thermionic or field electron emission into the vacuum, normally with an energy ranging from 0.2 to 40 keV.[6] After focusing by condenser lenses, the electron beam has a spot about 0.4 to 5 nm in diameter. When this beam hits the sample surface, electrons interact with atoms at or near the surface of the sample and generate several types of signals, including secondary electrons, back-scattered electrons, characteristic X-rays, cathodoluminescence, sample current and transmitted electrons. Among them, the secondary electron detection is the most commonly used mode. With help of scanning coils or deflector plates, the electron beam can scan across the sample surface along the X and Y directions. The generated signal can be used to map out the large area sample topography, composition and/or other information. Because the SEM image is composed of processed signal, the image is usually black-and-white with the information shown as brightness and contrast. But in some systems, the combination of several kinds of signals can artificially colourize the image.

Figure 2-10. Zeiss XB 1540 FIB/SEM system in London Centre for Nanotechnology.

For SEM measurements, sample preparation is critical for obtaining good-quality images. The sample needs be able to prevent the accumulation of charges at the surface. Nonconductive samples tend to accumulate charges during the measurement, especially in secondary electron imaging mode. This can affect the electron beam and lead to low image quality. The NW measurement is even more sensitive to the charging effect. Poorly-prepared samples with low conductivity can cause vibration and bending of the NWs, which leads to blurring or image artefacts (Fig. 2-11). Electrically grounding the sample is a commonly used method, such as using the silver paste to stick the sample to the specimen holder. For samples with low conductivity, it is necessary to create some paths for discharge. Coating with an ultrathin layer of electrically conducting material, such as Au, is a commonly used method.

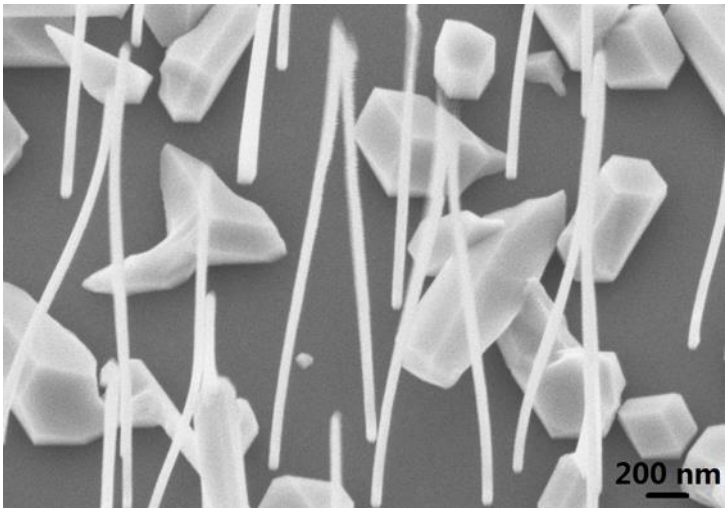

Figure 2-11. Bending and blurring of GaAsP NWs caused by the charging effect.

2.4 Transmission Electron Microscope (TEM)

The TEM measurements for this thesis were done at University of Warwick and Gasp Solar ApS using JEOL 2100 and JEOL ARM200F microscopes.

The TEM is the best facility to obtain crystallographic information about the sample. Same as the SEM, the TEM uses an electron beam as the probe in the measurement. The beam is highly converged, which allows examining the fine detail of the samples, such as a single column of atoms. During the measurement, the electron beam transmits through the ultra-thin specimen and at the same time interacts with the specimen atoms, which results in it containing the crystallographic information of the sample.

When the electron beam is passing through the sample, some electrons will be able to directly pass through without being affected by sample. If the measurement is using these electrons as the source of the signal, this mode is called “bright field imaging mode”, which is the most frequently used mode. During the measurement, if there is no sample in the beam path, the corresponding spot in the picture appears to be bright. If the beam needs to pass

through the sample, it will cause the electron number reduction by occlusion and absorption. For sample regions that are thicker or with a higher atomic number, it will appear to be darker. Therefore, the variation of the contrast can be used for mapping out the sample information. On the other hand, some of the electrons undergo Bragg scattering during passing through the sample. For sample regions that are thicker or with a higher atomic number, the scattering is stronger. If these electrons are used as signal, the diffraction contrast can be used for imaging and providing the crystal information. This mode is called "dark field imaging mode". The images from bright and dark field modes are opposite in contrast and brightness (Fig. 2-12). The bright field mode has a better resolution but a lower element differentiation, while the dark field mode is just opposite with a higher element differentiation and a lower resolution.[7]

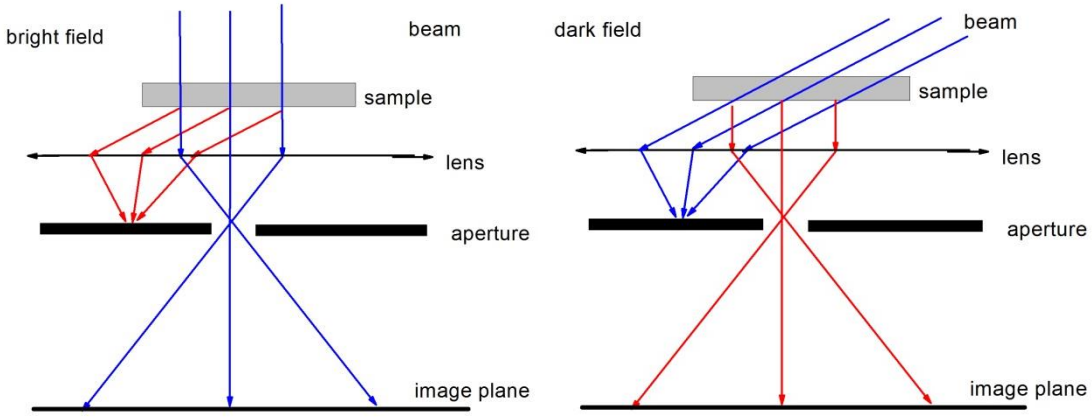

Figure 2-12. Illustration of the bright- and dark field TEM modes.

2.5 Photoluminescence (PL)

Photoluminescence is a non-destructive technique, which is important for the determination of impurities in semiconductors, the band gap of materials and device

structures. The setup includes an excitation light source (532 nm laser here), sample holder stage, sample cooling system (He compressor), monochromator, detector, and signal analyser (computer software). The simplified structure can be seen in Fig. 2-13.

During the measurement, the sample is excited by an optical source. Typically, the optical source is a laser with the photon energy higher than the bandgap of the measured material. Therefore, the absorption of the photons can help the electrons to jump from the valence band to conduction band and generate electron-hole pairs. The electron-hole pairs can relax to a lower energy state through several mechanisms. At room temperature, the band-to-band recombination dominates the emission. At low temperature, the band-to-band recombination is difficult to be observed, because the Coulombic attraction can bind electrons and holes together to form electron-hole pairs that are called "excitons".[8] The photons emitted from the excitons are slightly lower in energy than those from the band-to-band recombination. The recombination can also happen between impurity energy levels, conduction band, and valence band. In most processes the extra energy will be released in form of photons. By measuring the emitted photon energy, the energy level of impurities and the information about device structure can be obtained. In addition, the PL measurement can be used to roughly check the crystal quality, especially the active region of the optoelectronic devices, because the defects normally contribute to non-radiative recombinations. High defects density will lead to strong non-radiative recombinations, which will result in low internal quantum efficiency and hence weak emission intensity. The measurement at a low temperature is beneficial for minimizing the thermal line broadening. The thermal-induced band structure broadening is about kT/2 (k is Boltzmann constant). Cooling the sample can

effectively reduce the broadening. For example, the kT/2 is only 1.8 meV at 4.2 K, which is sufficiently low for most measurements. By doing the power dependent measurements, the filling of the excited states can help to extrapolate the band structure, such as the energy level splitting caused by quantum confinement. The temperature dependent measurement also has similar function. For example, the thermal escape energy can help to deduce the barriers for carrier confinement.

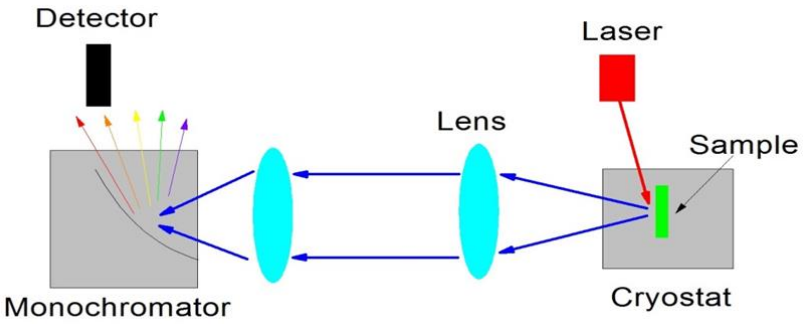

Figure 2-13. Illustration of the PL setting.

For the NW measurement, the heating effect by the laser is significant. Due to the 1D columnar shape with a small interface with the substrate, the heat dissipation is by far lower than that of the bulk material. The heat accumulation can lead to expansion of the lattice and hence change the band structure. As a result, the emission peaks will shift and give out false information. As can be seen in the GaAsP NW measurements at 13K with a laser power of 70 mW shown in Fig. 2-14a, after sufficient sample cooling by blocking the laser, the PL spectrum of the first measurement had a peak wavelength around 800 nm and an intensity about 0.0057 a.u. Right after the first measurement, the second measurement was performed. The peak wavelength of this scan shifted to 820 nm and the intensity reduced by ~30% to

0.0040 a.u. After the second measurement, the laser was blocked again for 1 min to cool down the sample. The peak emission wavelength and intensity of this third scan were almost comparable with those of the first measurement. One scan in Fig. 2-14a was ~23 sec, which indicates that the heating effect of the NW by the laser is very fast. In order to determine the heating up rate, measurements with different wavelength range and hence the different laser heating time was carried out. The measurements in the wavelength range from 750 to 800 nm were preceded by sufficient sample cooling. This can guarantee the value of the 750-nm point in the PL spectrum is free from the heating effect. After that, three measurements were carried out with wavelength ranges of 700~750, 725~750 and 745~750 nm, respectively. Before each measurement, the sample was adequately cooled. As can be seen in Fig. 2-14b, among these three measurements, only the 745~850 nm curve has an end point that can join the start point of the 750~800 nm curve, which indicates the ultra-fast heating rate at this high laser power of 70 mW. Therefore, choosing a suitable laser power to minimize the heating effect but keeping a sufficient emission signal is critical in the NW PL measurement.

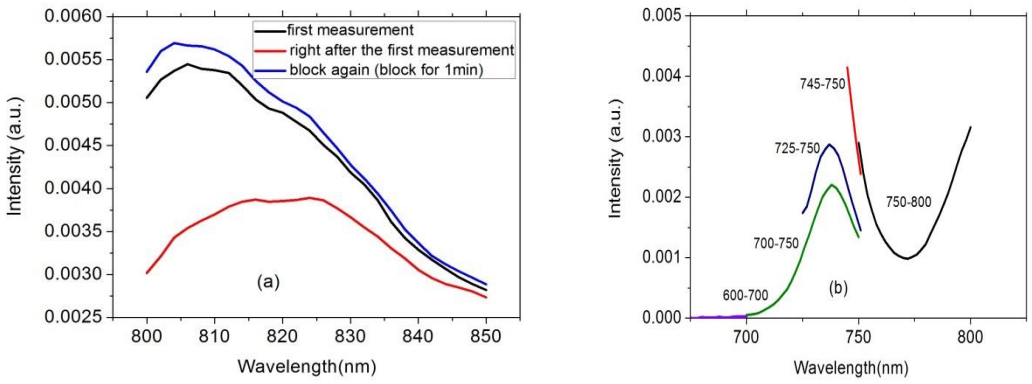

Figure 2-14. (a) PL spectra of GaAsP NWs measured with different laser heating time. (b) PL spectra with different scan range.

2.6 X-Ray Diffraction (XRD)

The wavelength of X-rays is comparable to the interatomic distances in crystals. When the X-ray interacts with the periodic atom arrays in the crystal, diffraction can happen and carry out rich crystallographic information. Thus, X-ray diffraction is widely used in semiconductor field to determine the parameters of epitaxial layers, such as the composition, lattice mismatch, defects, mis-orientation, layer thickness, tilt, relaxation, strain, interface quality, and area homogeneity.

The most important parts of the XRD machine are X-ray tube, sample stage and the X-ray detector, as can be seen in Fig. 2-15a. During the measurement, as illustrated in Fig. 2-15b, the X-ray irradiates parallel planes of atoms and can be scattered by atoms inside. At a certain incident angle θ, the light-path difference of scattered waves can satisfy the Bragg's Law:

$$n\lambda = 2d \sin \theta$$

where n is positive integer, λ is the wavelength of the X-ray, d is the interplanar spacing, and θ is the incident angle. In this case, the interference of the scattered light can lead to an enhanced peak intensity. This is also called diffraction. Since the X-ray wavelength λ is fixed, a family of planes, with an interplanar spacing of d, produces a diffraction peak only at a specific angle θ. Therefore, the space between diffracting planes of atoms determines peak positions. Because the interplanar spacing of atomic planes is governed by the material composition, XRD can be used to check the NW composition and lattice mismatch between the core and shell. As can be seen in Fig. 2-16, the diffraction peaks from the core and shell of the GaAsP NWs are at different angles if they have different lattice constant and hence

composition.

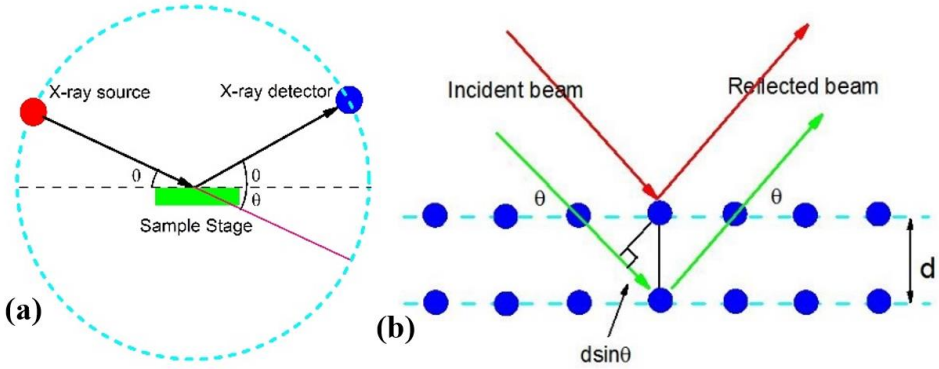

Figure 2-15. (a) Illustration of XRD system. (b) Illustration of XRD measurment mechanism.

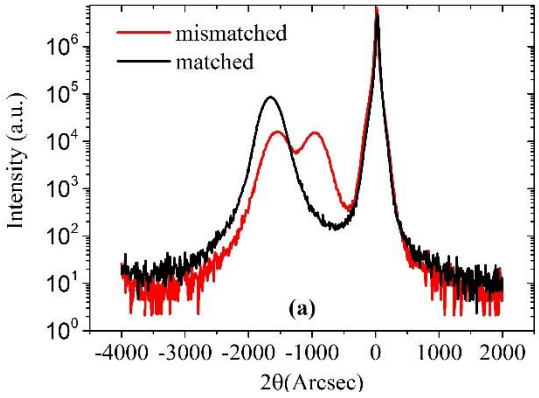

Figure 2-16. XRD measurement of GaAsP NWs with lattice matched and mis-matched core and shell.

2.7 Energy-Dispersive X-Ray Spectroscopy (EDS, EDX, or XEDS)

The EDX measurements for this thesis were done at University of Warwick and Gasp Solar ApS.

The EDX is also known as energy dispersive X-ray analysis (EDXA) or energy dispersive X-ray microanalysis (EDXMA). It allows one to identify what these particular elements are and their relative proportions in a non-destructive way. Thus, it is widely used as

the elemental analysis and chemical characterization of materials.

As illustrated in Fig. 2-17, during the measurement, a high energy source, electrons, protons, or a beam of X-ray, is needed. Their energy can be transferred to inner-shell electrons of the specimen atoms, ejecting them to create holes. These holes are subsequently filled by an electron from an outer higher-energy shell. The superfluous energy resulting from the energy difference between the shells is emitted as a characteristic X-ray photon. Because each element has a unique atomic structure, it can have a unique set of peaks in its X-ray emission spectrum, which can be used to identify elements. If the specimen contains several elements, the fitting of the emission spectrum can give out the atomic percentage of each one.

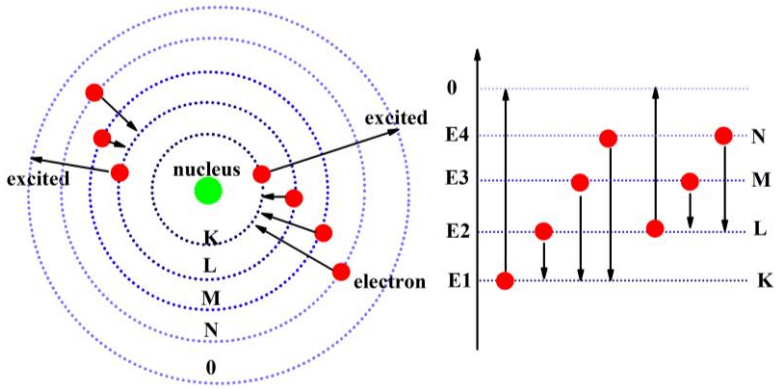

Figure 2-17. Illustration of characteristic X-ray generation.

2.8 Nanoimprint Lithography (NIL)

The patterned Si substrates used in this thesis were prepared by Gasp Solar ApS using NIL.

The NIL is an efficient way to produce small-sized features (down to sub-10nm)[9] over a large area with a high throughput, high resolution and low cost. In a single full-wafer nanoimprint process, wafers with a diameter of 8-inch (203 mm) or more can be printed with

high fidelity. There are many different types of NIL, but two of them are most important and fundamental, namely thermal nanoimprint lithography (T-NIL) and UV-based Nanoimprint Lithography (UV-NIL).

The standard T-NIL and UV-NIL processes need a mold with 3D features. This mold making can be done by the optical lithography technology (OL). However, when the size of the feature is in nanometre range, the electron beam lithography technology (EBL) is preferred. Normally, the mould material needs to have sufficient hardness, good durability, and low chemical reactivity with the involved materials. Therefore, materials, such as silicon, silicon dioxide, silicon carbide, ceramics, quartz, diamond and some polymers can be used to make moulds. Other properties, such as thermal expansion coefficient and transparency, are also important. For example, due to the high temperature operation, the T-NIL needs to consider the thermal expansion coefficient matching between the mould and the wafer. For the UV-NIL process, a mould with good UV light transparency is necessary to achieve successful imprint.

In a standard T-NIL process, a layer of imprint resist, which is normally a thermoplastic polymer, is spin-coated onto the substrate (Fig. 2-18b). Then a mould with predefined pattern features, is pressed against polymer layer with suitable pressure. By heating up the whole setting above the glass transition temperature of the polymer, the pattern features on the mould can be pressed into the polymer layer (Fig. 2-18b and b1). When the system is cooled down and when the polymer is hard enough the mould can be separated, leaving the pattern features in the polymer layer (Fig. 2-18b2). Afterwards, the patterns can be transferred to the substrate underneath (Fig. 2-18c and c').

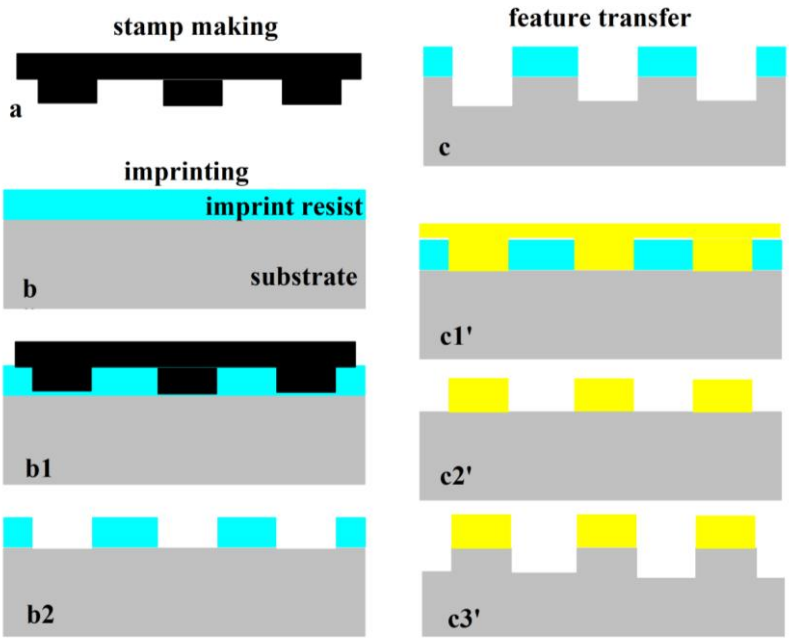

Figure 2-18. Illustration of the T-NIL process. (a) Stamp making, (b) imprint process, and (c) (c') pattern transfer from the imprint resist layer to the substrates.

The UV-NIL shares the basic theory with the T-NIL, but can be performed at room temperature with low pressure. Therefore, this technique has several advantages compared with the T-NIL, such as better overlay alignment accuracy and easier tool design due to the absence of high imprint pressures and thermal heating cycles. However, the cost for these advantages is the additional requirement of the UV transparency for the mould. During the process, a UV-curable liquid photopolymer, instead of thermoplastic, is deposited onto the substrate as the imprint resist (Fig. 2-19b). Then, the UV-transparent mould is pressed against the substrate and the cavities (trenches) will be fully filled by resist (Fig. 2-19c). Next, the resist is cured by UV light and becomes solid (Fig. 2-19d). After detaching the mould from the resist, the pattern transfer can be achieved in the same way as the T-NIL.

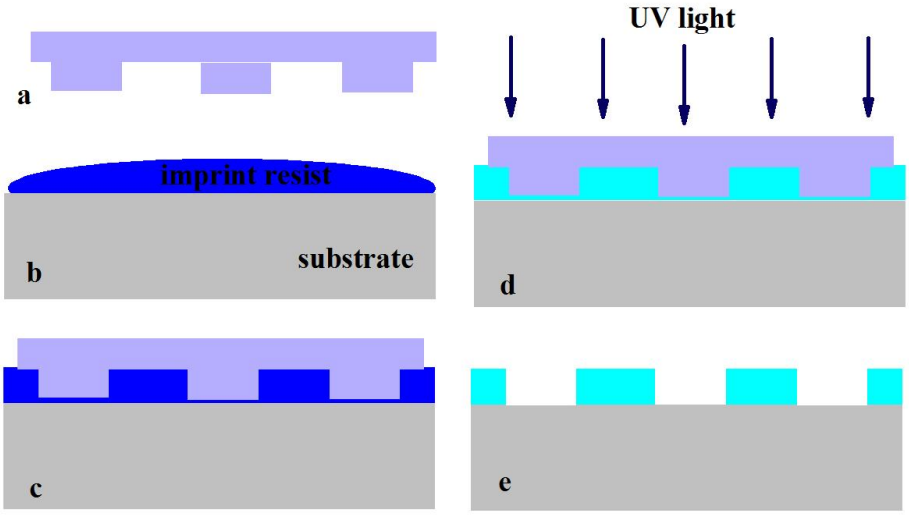

Figure 2-19. Illustration of the UV-NIL process. (a) Stamp making, (b) resist coating, (c) mold contact with the substrate, (d) resist curing, and (d) mold detaching.

The UV-NIL was used to prepare patterned substrates for the growths in this thesis. First, a layer of ~30 nm thermal oxide was grown on Si substrates in a high-temperature oven. SF2GS microresist was then spin coated over the oxide and imprinted with a jet-and-flash imprint lithography (Imprio 100) system. The imprinted patterns were transferred to the thermal oxide by depositing a 20 nm Al film as shadowing mask and then followed by both dry and wet etching of the thermal oxide. As can be seen in Fig. 2-20, holes with various diameters can be created on the patterned substrate.

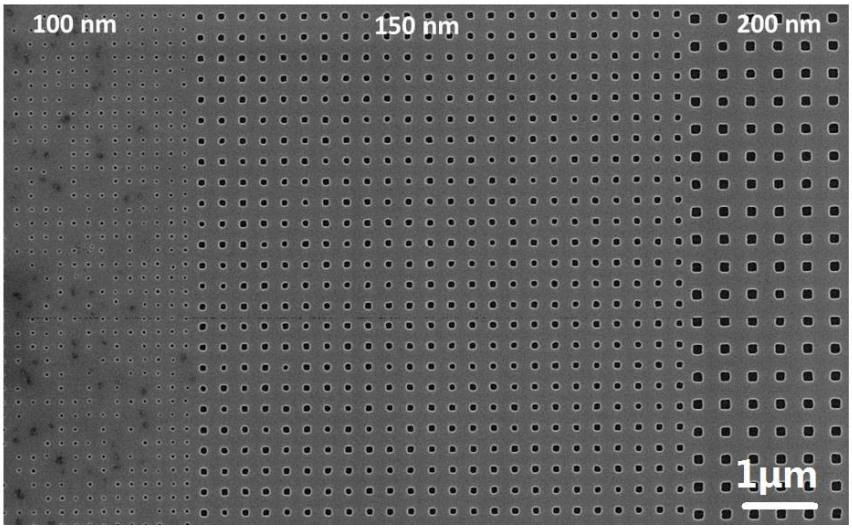

Figure 2-20. SEM image of patterned Si substrate used in positioned NW growth.

2.9 References

1. Franchi S, Trevisi G, Seravalli L, and Frigeri P 2003 Progress in Crystal Growth and Characterization of Materials 47 166

2. GEN II GEN930 Operation Manual, Document 580009

3. Yazawa M, Koguchi M, Muto A, Ozawa M, and Hiruma K 1992 Applied Physics Letters 61 2051.

4. Oura K, Lifshits V G, Saranin A A, Zotov A V, and Katayama M 2003 Surface Science: An Introduction. Berlin: Springer

5. Lee A D, Jiang Q, Tang M, Zhang Y, Seeds A J, and Liu H 2013 IEEE Journal of Selected Topics in Quantum Electronics 19 1901107

6. http://en.wikipedia.org/wiki/Scanning_electron_microscope (June 1st, 2015)

7. http://en.wikipedia.org/wiki/Transmission_electron_microscopy (June 1st, 2015)

8. http://en.wikipedia.org/wiki/Exciton (June 1st, 2015)

9. Lan H, Ding Y. Nanoimprint lithography [J]. Lithography, Michael Wang (ED.), 2010.

Chapter 3:

GaAsP Nanowire Growth on Si Substrates

3.1 Introduction

The ternary material GaAsP has a bandgap that can cover wavelengths from green to infrared. This can offer more freedom in band structure design compared with binary materials, which is very useful for optoelectronic and photovoltaic devices.[1,2] Especially integration of high performance GaAsP optoelectronic devices with the mature, low-cost, large-scale silicon microelectronic technologies can greatly reduce the cost but maintain good device performance. In traditional thin film growth, this goal is difficult to be achieved due to the limitations, such as the lattice and thermal expansion coefficient mismatch. This integration can be achieved with NW structure, because the NWs have excellent strain relaxation ability. Recently, great attention has been paid to the development of GaAsP NWs. However, there are only a few publications about GaAsP NWs in the literature due to difficulties in growing ternary phosphide NWs.[3-8] To facilitate the GaAsP NW growth, most of the reported growths were performed with the help of Au catalyst, because Au has a lot of

advantages such as a large growth window and non-consumable features.[9] However, Au can also degrade device performance because it can be incorporated into Si and NWs to form mid-gap energy states.[10-12] To circumvent these drawbacks, the self-catalysed growth approach is needed to replace the Au-catalysed one. At present, the self-catalysed ternary GaAsP NW is still a less developed field compared with the self-catalysed GaAs NW.[13-16] In addition, introduction of P into the growth can significantly change the nucleation features, and hence make the growth much more complex and difficult to control.

In this Chapter, the self-catalysed GaAsP NW growth was studied by investigating a wide range of growth parameters, such as the V/III flux ratio, growth rate and growth temperature. NWs with good morphology and crystal quality have been achieved over a large range of growth rates. The P incorporation efficiency during these NW growths was found to be two times higher than that of As. The mechanism of this phenomenon is investigated in comparison with the thin film growth. Moreover, in order to proceed to the practical applications of these GaAsP NWs, the Be doping, Ga droplet consumption and the uniformity control were also investigated.

3.2 Experiment

The GaAsP NWs were grown on 3-inch native-oxide-covered 380-μm-thick p-doped silicon (111) substrates by MBE. [17] The substrates were thermally degassed at 500 °C for 1 h under ultrahigh vacuum conditions. After this, the substrates were loaded into the MBE growth chamber for NW growth. Before the growth the substrates were annealed at 640 °C, as measured by the pyrometer, for 5−8 mins under As environment. After that, the substrate was

kept at the same temperature for growth, if not indicated otherwise. Depending on different study purposes, the growth started with the Ga flux and the V/III flux ratio within the range of 4~11.2×10^{-8} torr and 40~80, respectively. Be was used as the p-type dopant. Due to the difficulty of knowing the actual doping concentration in the NW, the nominal 2D thin film doping concentration, calibrated from planar growth of GaAs at 1ML s^{-1}, was used to describe the NW doping.

3.3 Results and Discussion

3.3.1 Comparison between GaAs and GaAsP Nanowire Growth

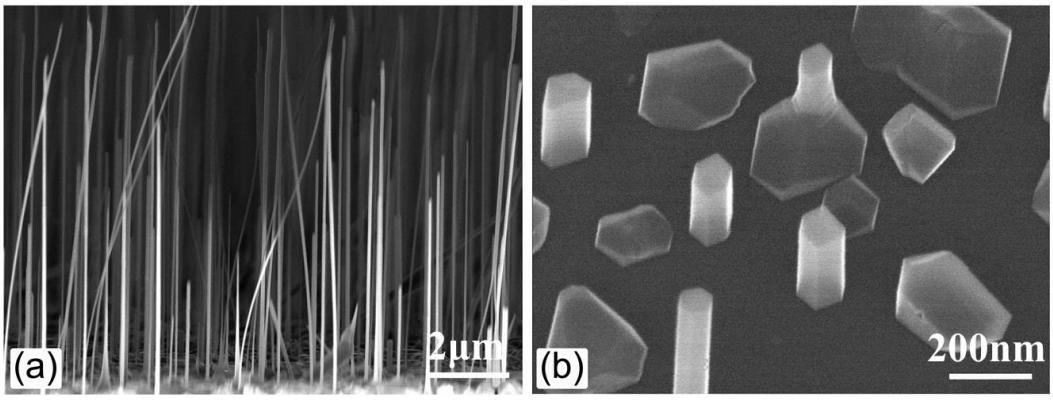

Figure 3-1. SEM image of (a) GaAs NWs and (b) GaAsP pillars grown with a V/III flux ratio of 122. The P/As flux ratio of during the growth of (b) was 1.

The GaAsP NW is made of ternary material, which is different from the GaAs NWs. The participation of phosphorus can make the growth more complex. Therefore, the difference between the GaAs and GaAsP NW growth was first studied. Both the GaAs and the GaAsP NWs were grown under the same condition with a V/III ratio of 122. The P/(P+As) flux ratio was the only difference between them, which was 0 and 50%, respectively. As shown in

Fig. 3-1a, the GaAs NWs are quite long and thin. In contrast, the GaAsP growth shown in Fig. 3-1b only has some thick and short pillars with flat top facet and vertical side facets. This phenomenon indicates that the GaAsP wafer may have grown without the presence of the catalyst droplet, but instead adopting a selective area VS growth mode.[18,19] These results can be explained by the model proposed by Rudolph *et al*.[20] During their self-catalyzed GaAs NW growth, the increase of V/III ratio can increase the NW rate but reduce the diameter, due to the increase of the supersaturation of the catalyst droplet. Further increasing the V/III ratio, the growth mode changed from the VLS growth mode to the VS growth mode and the growth rate and the diameter experienced a rapid decrease and increase, respectively. This model can fit the results in Fig. 3-1 very well. The high V/III ratio of 112 made the GaAs NWs long and thin, but it was still within the VLS growth region. When half of the As flux was replaced by P in the GaAsP growth, the P greatly increased the Ga droplet supersaturation[21] and consumed it rapidly. It is even possible that the fast nucleation rate did not allow the Ga droplet formation at the initial growth stage. The continued growth was following the VS growth mode. Therefore, the stark contrast between the GaAs and GaAsP growths suggests that the P has quite different nucleation features compared with that of the As. In order to achieve the GaAsP NW growth, the growth parameters need to be carefully adjusted to control the NW nucleation, such as the V/III ratio, growth rate, and the growth temperature.

3.3.2 Influence of V/III flux ratio for GaAsP NW growth

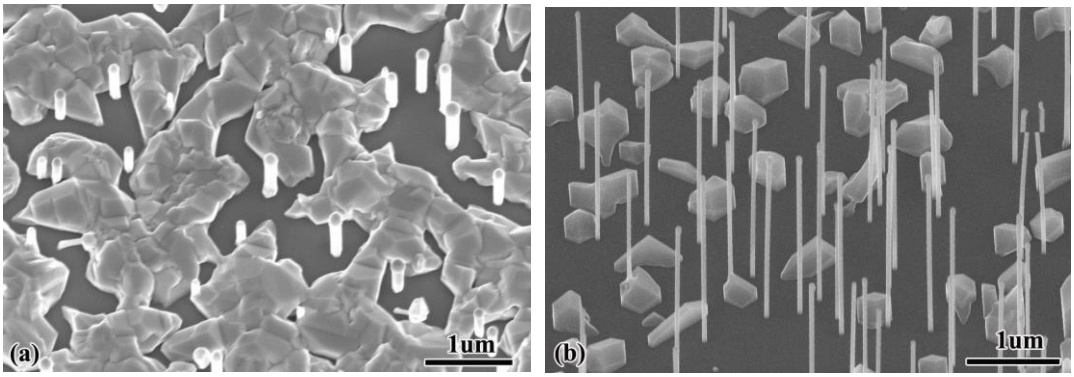

Figure 3-2. SEM images of GaAsP NWs grown with a V/III ratio of (a) 25 and (b) 50.

Adjusting the V/III ratio can control the droplet supersaturation. When increasing the V/III flux ratio, the droplet supersaturation can increase and hence the NW nucleation rate, which leads to shrinkage of the droplet size. As the droplet size decreases, the Gibbs-Thomson effect can increase the As and P vapour pressure of the alloy particles.[22] This can reduce the driving force for the transport of As and P from the vapour to the droplet, which can reduce the effective supersaturation of the droplet.[22] Balance between the vapour chemical potential (V/III flux ratio) and the Gibbs-Thomson effect can lead to a balanced droplet size, which can decide the NW diameter. Therefore, the samples grown at higher V/III flux ratios can produce NWs with a smaller diameter. As can be seen in Fig. 3-2, the NWs grown at a low V/III ratio of 25 are much thicker than 100 nm, while these grown with a high V/III ratio of 50 are only about 50 nm.

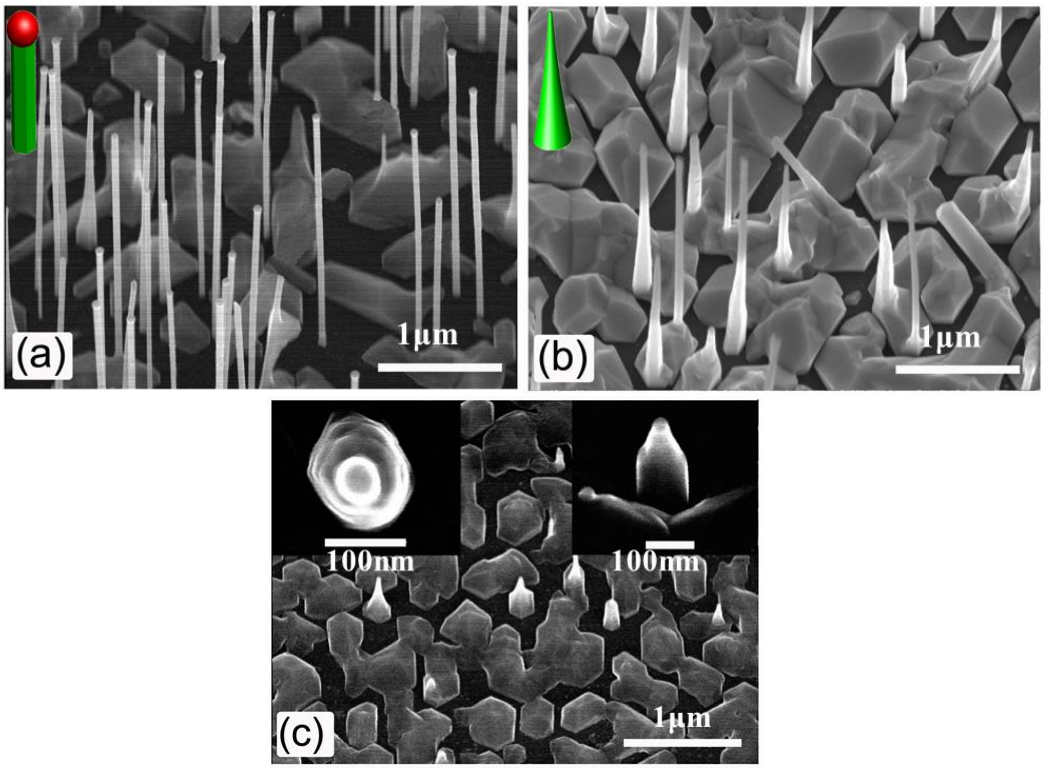

Figure 3-3. SEM images of GaAsP NWs grown with a Ga flux of 8.72×10^{-8} torr, but with V/III ratio of (a) 50, (b) 75, and (c) 100. The insets in (a) and (b) illustrates the NW morphology; while these in (c) are the top and side view of a nano-bud with a scale bar of 100 nm.

However, a too high V/III ratio can have adverse effect on the NW growth. The influence of V/III ratio on the GaAsP NW growth was investigated by changing it from 50 to 100 with the same Ga flux. As shown in Fig. 3-3a, the NWs grown with the V/III flux ratio of 50 are homogeneous in diameter over the whole length. There is a droplet at the very tip of the NW, which clearly indicates the VLS growth mode. In the VLS growth mode, the droplet size decides the NW diameter if there is no VS lateral sidewall growth.[23-25] Therefore, the homogeneous diameter along the NW length reflects that the Ga droplet size was constant during the growth. This further reveals the well balanced replenishment and consumption of the Ga in the droplets under this V/III ratio. Increasing the V/III flux ratio to 75, as shown in

Fig. 3-3b, the NWs exhibit a tapered shape with a much larger base compared with that of the NWs shown in Fig. 3-3a. On the tip of the NWs, there is no evidence to show the existence of the Ga droplet. With the increase of the V/III flux ratio, the lateral sidewall growth, especially on the lower NW facets, can be greatly increased, which can reduce the Ga replenishment of the droplets. As a result, the Ga droplet could not maintain the balance and shrank gradually during the growth. After the disappearance of the Ga droplet, the growth switched to VS mode, causing further increase of the diameter. Further increasing the V/III flux ratio to 100, the droplet was only allowed to survive for a very short time. The lateral VS growth after the disappearance of the droplet led to the cone-shaped nano-buds shown in Fig. 3-3c.

3.3.3 Influence of Growth rate

In thin film growth, the growth rate is a critical parameter which can greatly affect the crystal quality. In order to investigate the influence of growth rate, three growths were performed with the same V/III ratio of 50, but different Ga flux value of 4.62×10^{-8}, 6.78×10^{-8}, and 8.72×10^{-8} torr, respectively. As can be seen in Fig. 3-4, the NWs from all these three samples are quite similar in morphology with uniform diameter along the NW length. Presence of the Ga droplet at the NW tip indicates the VLS mode of all the three NW growths. This shows that it is not the Ga flux, but rather the V/III ratio which plays a decisive role in the self-catalysed GaAsP NW growth. However, the Ga flux can significantly decide the NW density. As the Ga flux increased from 4.62×10^{-8} to 8.72×10^{-8} torr, the NW density increased significantly. This could be due to enhanced nucleation that generates more Ga droplets for NW growth. Therefore, the NW density control can be achieved by the adjustment of the Ga

flux.

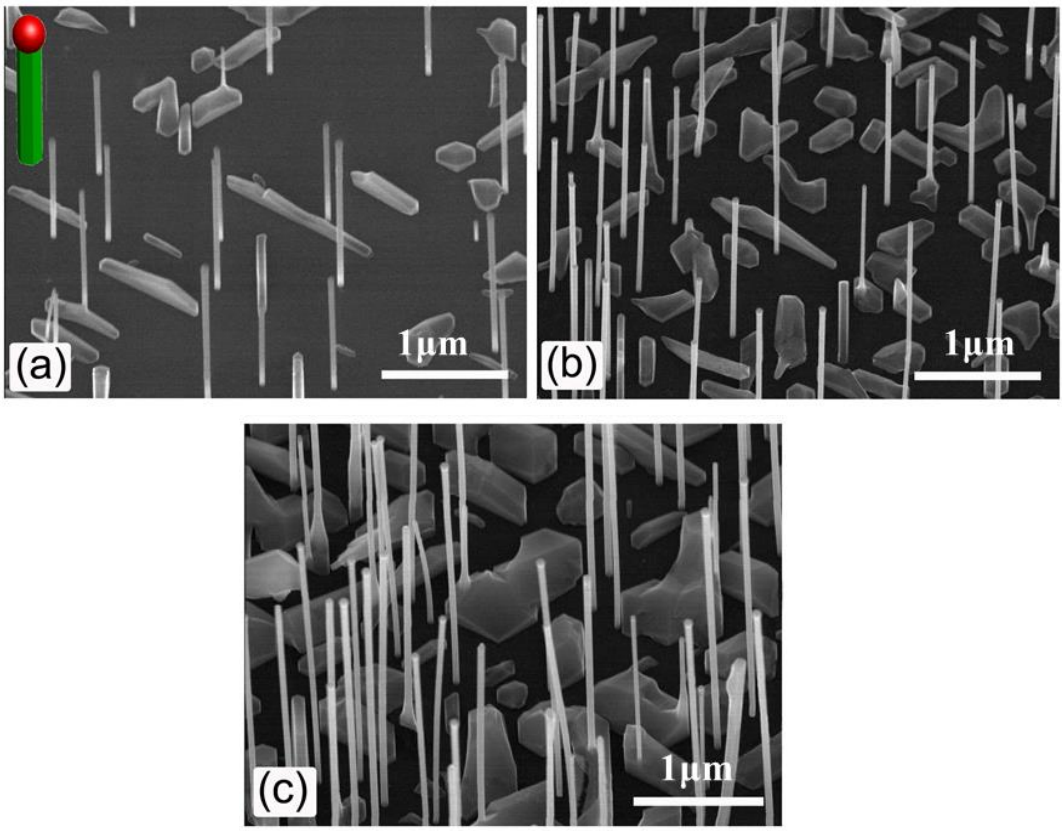

Figure 3-4. SEM images of GaAsP NWs grown with a V/III ratio of 50 and a P/As flux ratio of ~0.14. The Ga flux of (a), (b), and (c) were 4.62×10^{-8}, 6.78×10^{-8}, and 8.72×10^{-8} torr, respectively.

3.3.4 Influence of Growth Temperature

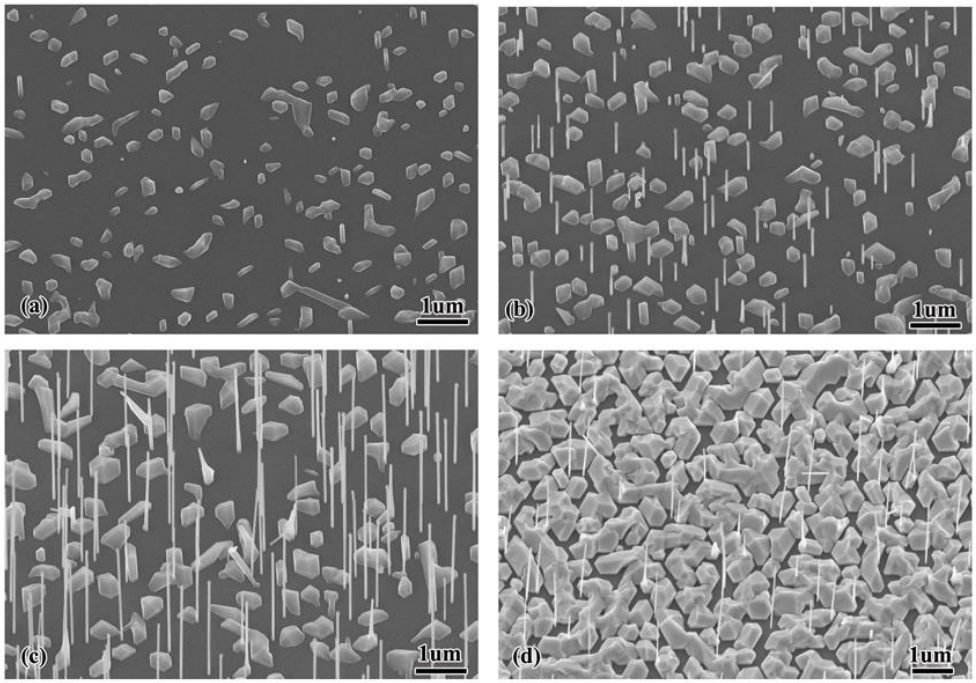

Figure 3-5. SEM images of GaAsP NWs grown on Si(111) substrates. (a)~(d) show the location from substrate centre (645 °C) to edge (635 °C).

The growth temperature is also an important factor that can greatly govern NW growth. The influence of the growth temperature on the NW growth can be seen on the sample shown in Fig. 3-5. The centre of this sample, Fig. 3-5a, only has some small clusters. No NW growth has happened in this area. Moving from the centre to the edge, the NW growth became possible and the NW length is longer when it is closer to the edge. This could be due to the influence of the temperature on the supersaturation of the droplet. As the temperature increases, the supersaturation in the droplet decreases.[21] This could reduce the NW growth rate when it is closer to the centre. In addition, from the wafer centre to edge, the cluster size increases with the decrease of the temperature. At the very edge of the sample, Fig. 3-5d,

the cluster strongly affects the NW growth. These phenomena indicate that the material loss is significant at the centre part of the wafer with higher growth temperature as compared with the wafer edge with lower growth temperature. Strong material loss could also contribute to the absent or shortened NWs at the centre part of the wafer. The wafer used in this research is 3 inches in diameter. The temperature gradient should be around 10^{o}C, which suggests that the growth window of the NWs, at a given V/III ratio and growth rate, is very small.

3.3.5 Crystal Structure of Nanowires

The crystal quality of NWs is one of the key factors that can decide whether they are suitable for applications. For example, it can affect the carrier transport and the band structure.[26-28] Therefore, the crystal quality of NWs grown under different growth conditions were studied by TEM. As can be seen in Fig. 3-6a, b and c, the NWs grown with the right supersaturation (V/III flux ratio) have similar crystal structure despite the different growth rates (Ga fluxes). These NWs are uniform in diameter along the NW length. At the tip of the NW, there is a round droplet, which shows that these NWs were grown by Ga-catalysed VLS mode. There are only a few defects that are concentrated at the top and bottom parts of the NWs. The body of the NWs is almost defect-free with only some occasional twin planes. These NWs have a ZB crystal structure, as confirmed by the electron diffraction pattern shown in the insets. The good crystal quality of these NWs could be due to the low surface energy of the Ga droplet,[29] which can suppress TPL nucleation and promote growth of the ZB crystal structure. [25] As has been demonstrated in the Au-catalysed growth, increase of group-III content in the Au droplet can greatly increase the ZB nucleation probability. For

example, Gil *et al.*[29] increased the Ga concentration in the Au droplets to over 62% during their GaAs NW growth and achieved pure ZB crystal structure even for NWs with a diameter as small as 5 nm.

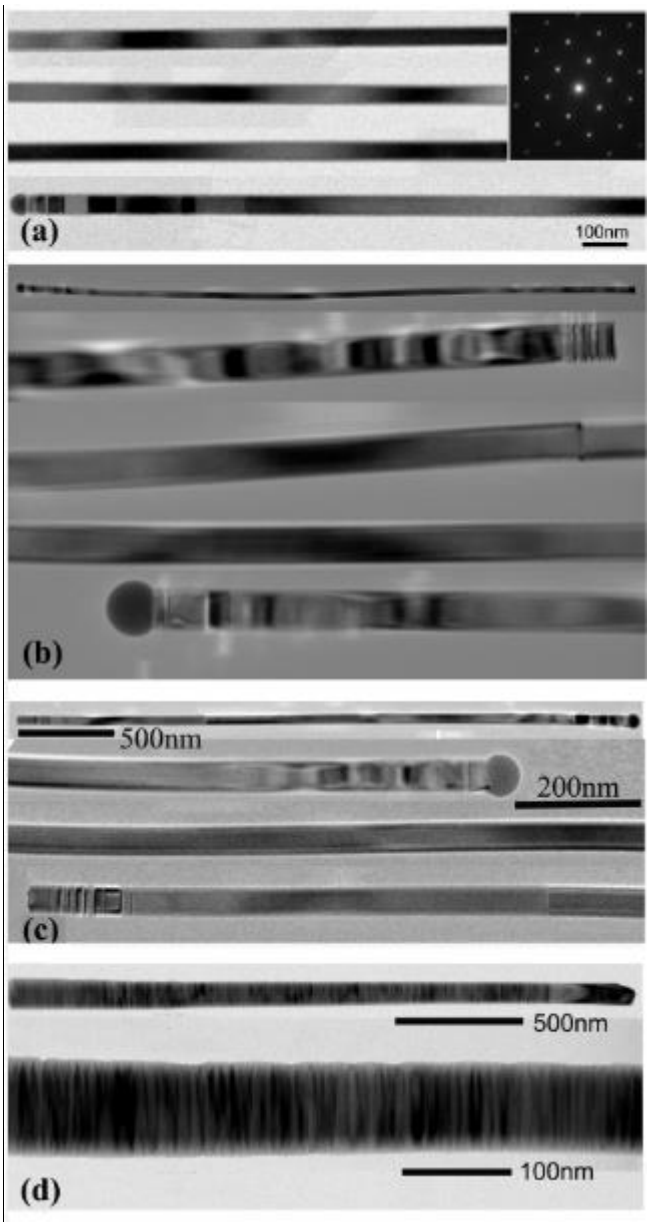

Figure 3-6. TEM images from NWs grown with (a) Ga=11.2×10^{-8}, V/III=50, (b) Ga=8.72×10^{-8}, V/III=50, (c) Ga=6.78×10^{-8}, V/III=50 and (d) Ga=8.72×10^{-8}, V/III=75. The inset in (a) is the electron diffraction pattern. Reprinted with permission from Ref.17. Copyright 2013 American Chemical Society.

In contrast, when the growth parameters are not optimized, especially under unsuitable V/III ratio, the NWs tend to have high density of defects. One example of these NWs is shown in Fig.3-6d which was grown with a V/III flux ratio of 75. This high defect density could be induced by high droplet supersaturation as the V/III flux ratio was increased. Under high droplet supersaturation, WZ nucleation probability can be greatly increased.[21,25,30,31] The droplet shrinkage can also be a cause of the high defect density. In the model proposed by Krogstrup *et al*.,[23] when the size of the large droplet reduces, the TPL will retract from the sidewall to the edge of the NW top facet, which promotes WZ formation. As observed by Rieger *et al*.,[13] the crystal structure can be changed between ZB and WZ phase by controlling the droplet size. In addition, Yu *et al*.[16] suggested that defects formation could be induced by the shift of TPL along the sidewall when the droplet size changes. In support of this theory, they observed an occurrence of a defect-section before the crystal structure was changed to pure WZ during the Ga droplet consumption of GaAs NWs. Besides, they also demonstrated the growth of ZB/defect-section superlattices and WZ/defect-section superlattices through changing the Ga droplet size, which can be used as another support for their defect-formation theory. Apart from the factors mentioned above, variation of NW diameter during growth could cause roughening of the semiconductor/metal interface and hence deformation of the TPL.[32]

Although the detailed growth mechanism for the defect formation is still unknown, keeping a well-balanced Ga droplet replenishment and consumption seems to be a very important factor which decides the crystal quality of NWs. Therefore, during the growth, the V/III ratio needs to be carefully controlled.

3.3.6 Phosphorus Incorporation Efficiency

One advantage of the GaAsP NW is the wide compositional tunability, which is beneficial for the device structure design. Therefore, composition control is highly important for the application of GaAsP NWs. Incorporation of P was investigated by comparing it with that of As.

Correlation between the P percentage in the NW and in the flux were studied by growing GaAsP NWs with different P/(P+As) flux ratios of 7.2%, 10%, 20%, 30%, 40%, and 50%. After measuring by EDX, the P/(P+As) in the NW as a function of that in the flux was shown in Fig. 3-6. As can be seen, by adjusting the P/As flux ratio, the GaAsP NWs with a P content ranging from 10% to 75% can be achieved.

Here, the P flux ratio is defined as:

$$x = \frac{F(P)}{F(P)+F(As)} \quad 3\text{-}1$$

Where F(P) and F(As) are the beam equivalent pressure of P and As flux, respectively.

The P content in the NW is defined as:

$$P\% = \frac{C(P)}{C(P)+C(As)} \quad 3\text{-}2$$

Where C(P) and C(As) are the concentration of P and As in the NWs, respectively.

By defining β as the incorporation coefficient of P and α of As, the P content can be written as:

$$P\% = \frac{\beta x}{\beta x + \alpha (1-x)} \quad 3\text{-}3$$

The relative incorporation ratio of P and As can be defined as:

$$R = \frac{P\%}{As\%} = \frac{\beta}{\alpha} \qquad 3\text{-}4$$

The P content can be changed to:

$$P\% = \frac{Rx}{Rx+(1-x)} = \frac{Rx}{1+(R-1)x} \qquad 3\text{-}5$$

By choosing R with a value of 2.97, Equation (5) fits well with the experimental results in Fig. 3-7. It can be found that the incorporation coefficient of P is about three times bigger than that of As. This is in stark contrast to the thin film planar epitaxial growth by gas-source and solid-source MBEs [33-36] in which As has much higher incorporation coefficient compared with P. The difference between VLS growth and VS growth of the GaAsP material can be explained by the schematic illustration shown in Fig. 3-8.

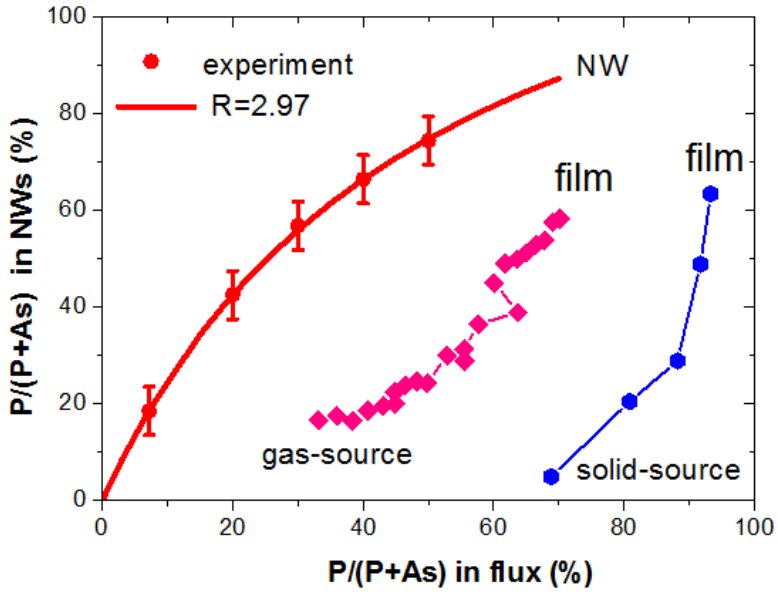

Figure 3-7. P/(P+As) in the NW as a function of that in the flux. The red dots and line show the experimental and fitted results of the NW growth, respectively. The thin film GaAsP grown by gas-source (pink) [33] and solid-source (blue) MBE[36] are also shown as a comparison.

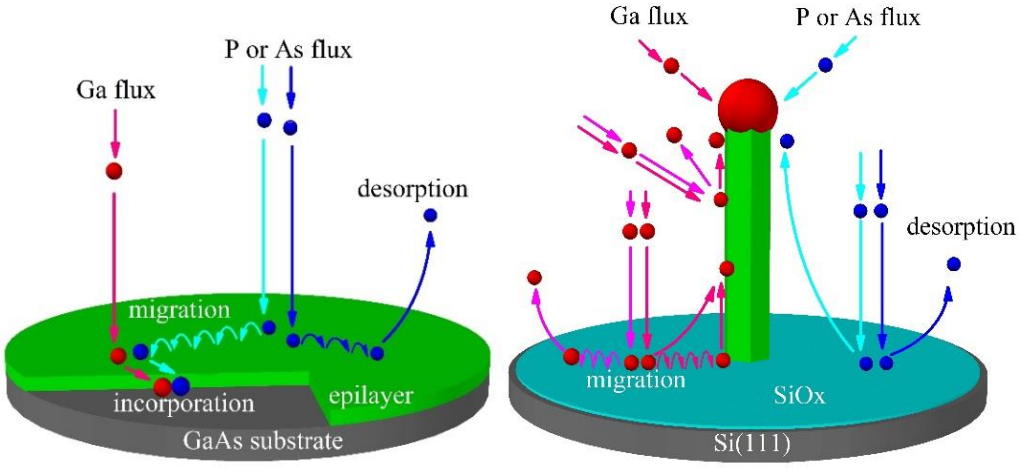

Figure 3-8. Growth mechanism illustration of the thin film VS and the NW VLS growth mode.

In the thin film growth it is following the VS growth mode, which is normal under group-V element rich condition. In this growth mode, growth rate is controlled by group-III elements. In this case, group-V adatoms cannot incorporate into the lattice if they are unable to meet group-III adatoms and in the end will desorb back into the vapour. As adatoms have a larger sticking coefficient and hence longer surface lifetime and migration length, which give them a larger possibility to meet Ga adatoms.[33,38] Therefore, in GaAsP film growth the As adatoms are much easier to incorporate into the epitaxial layer compared with P, though the As has lower chemical activity.[37] In the case of NWs, the growth follows the VLS mode, which is rich in group-III element. The growth is limited by group-V flux. The relative incorporation of P/As is determined by nucleation. The influence of P and As on the Au-catalysed NWs has been investigated theoretically by Glas.[25] According to his model, P has stronger influence on the chemical potential of the Au droplet. For the same concentration, P can increase the chemical potential much more than As. This suggests that inclusion of As atoms in the droplet would be easier than that of P in GaAsP NW growth. However,

according to our results, the extra chemical potential increase in the catalyst droplet does not form a barrier for absorbing P into it. Instead, the promoted chemical potential caused by P can enhance the nucleation rate of GaP relative to GaAs. From the analysis above, it can be seen that the incorporation ratio of P/As in the thin film growth is governed by the physical properties, while that of the NW growth is controlled by the chemical properties. This can be confirmed by the observation in Fig. 3-9 where the P content in the clusters is much lower than that in the NWs.

Moreover, it can be seen in Fig. 3-9 that the thinner NWs have higher P content. This also supports the model shown in Fig. 3-8. The droplets for the NW growth are in nanometre scale, which suffers from the Gibbs-Thomson effect. This makes the droplet of smaller size have a higher vapour pressure, which can drive out the group-V elements in the droplet more efficiently.[22,39] Therefore, higher P content in the thinner NWs indicates higher incorporation efficiency of P. It is also likely that because of this the tip of the GaAsP NWs is commonly observed to be rich in P as shown in Fig. 3-10. When both the As and P flux are turned off, the escape efficiency of As from the droplet could be much larger than that of the P in the environment with a reduced vapour chemical potential. This can enlarge the concentration difference between the P and As in the droplet. During the cooling down procedure, reduction of the temperature can increase droplet superaturation and push precipitation of P and As.

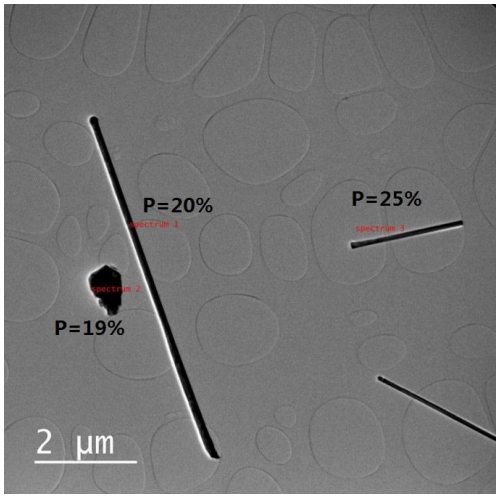

Figure 3-9. EDX meausurement of NWs with different diameters.

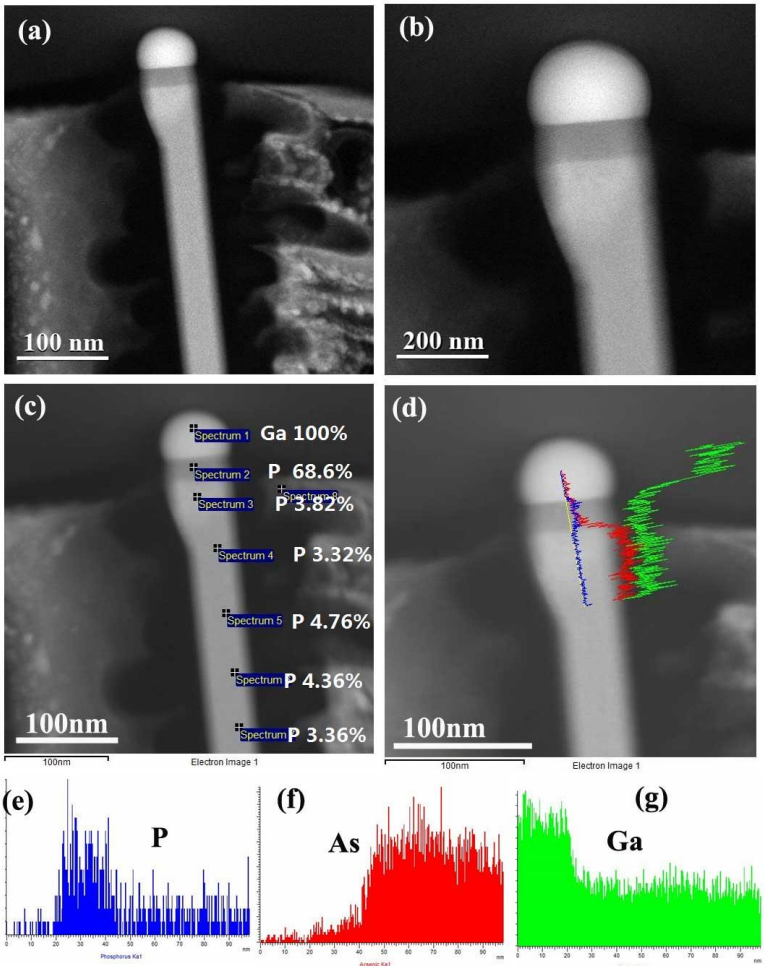

Figure 3-10. (a) and (b) Annular dark field images of GaAsP NW tip. (c) EDX shows the P content in the dark area close to the Ga droplet. (d) XRD line scans shows the same tendency observed in the point spectra measurements in (c). (e), (f) and (g) XRD line scans of P, As and Ga, respectively.

3.3.7 Beryllium Doping

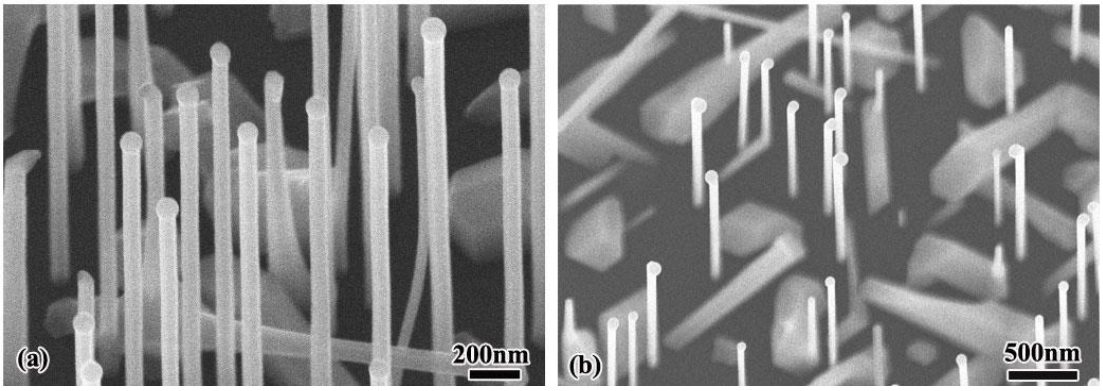

Figure 3-11. SEM images of GaAs NWs grown with Be doping of (a) 0 and (b) 8×10^{17} cm^{-3}.

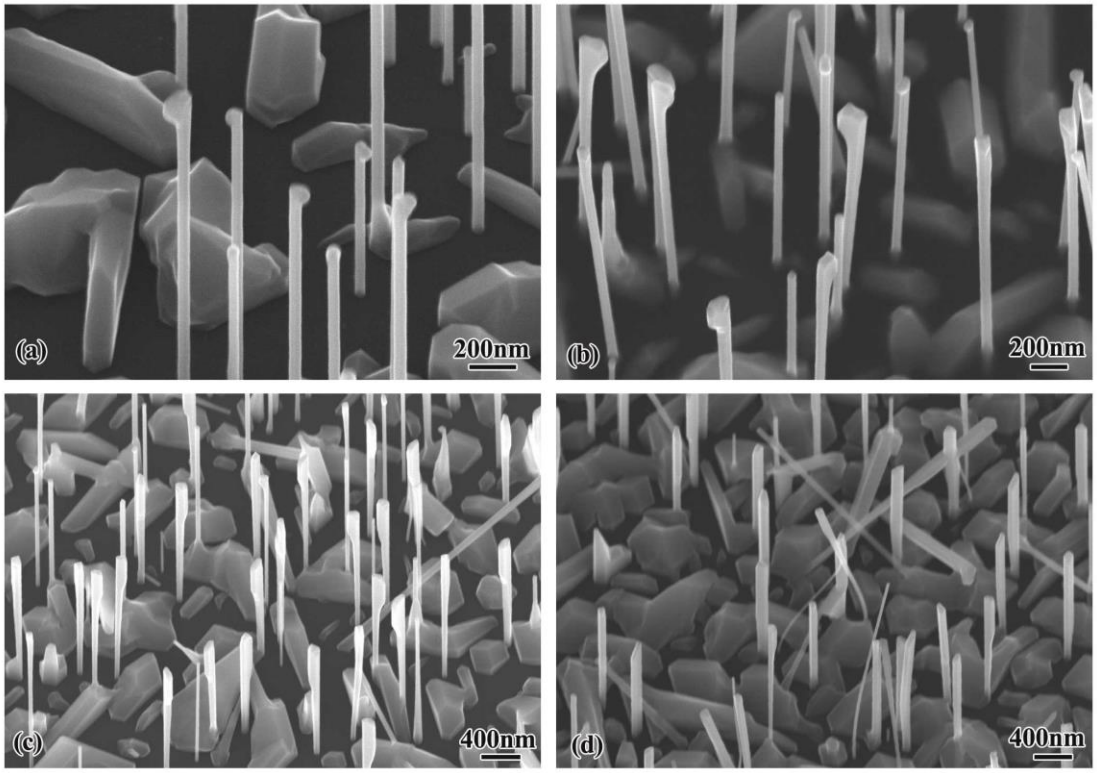

Figure 3-12. SEM images of GaAs NWs grown with Be doping of 1.28×10^{19} cm^{-3}. (a) to (d) is from centre to edge of the sample.

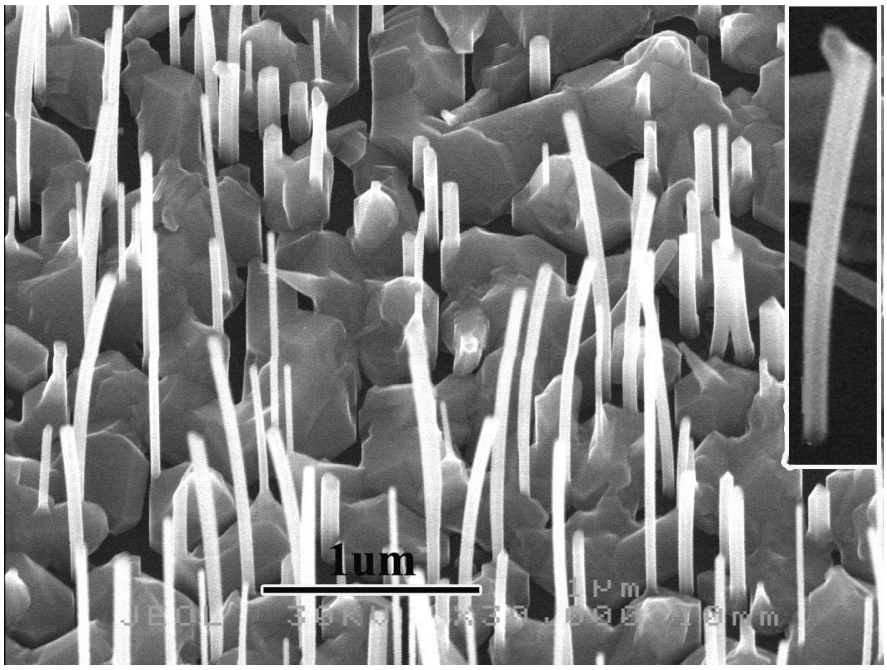

Figure 3-13. SEM images GaAsP sample with Be doping of 8.9×10^{18} cm^{-3}.

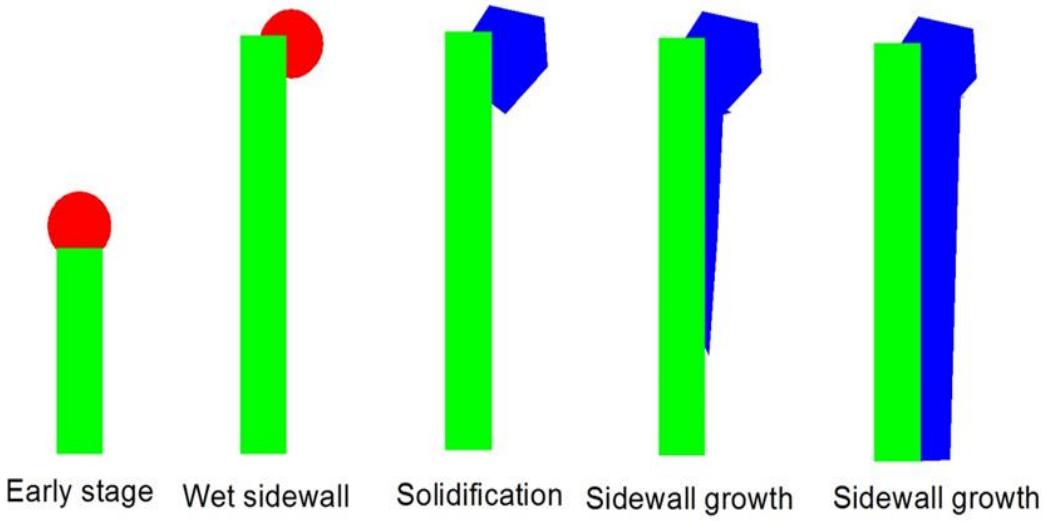

Figure 3-14. Illustration of the NW growth with high Be doping concentration.

Due to the VLS growth mode, the NW is more sensitive to doping, which could greatly change the electrical properties of semiconductors. Therefore, the doping of NWs was studied. As can be seen in Fig. 3-11, after introducing the doping with a nominal concentration of 8×10^{17} cm^{-3}, the Ga droplet position at the tip of the GaAs NW is moved towards the edge.

Further increasing the doping concentration to 1.28×10^{19} cm^{-3}, at the tip of the NWs shown in Fig. 3-12, the liquid Ga droplet no longer exists. Instead, there is a big lump, which replaced the droplet. Comparing the NWs from wafer centre to edge of this growth, it can be observed that the lump was developing downwards and closer to the sample edge it is comparatively well developed. This demonstrates that at a lower growth temperature, the NW is suffering stronger influence from the doping. GaAsP NWs exhibit the same phenomenon, which can be seen in Fig. 3-13. But the doped GaAsP NWs show an arc shape due to bending. All these phenomena could be explained by the illustrations shown in Fig. 3-14. At very early stage, the NW growth is normal, same as un-doped. But with the growth going on, the droplet can accumulate more and more Be, which could lead to lowering of the droplet surface energy.[40] The change in surface energy can influence the contact angle of the droplet and make it slide to sidewalls. Because the large contact area with the sidewalls can provide a large nucleation area, it can greatly increase the nucleation rate, making the droplet solidify quickly. This solidified droplet can provide new atomic steps or facets facilitating sidewall growth. The sidewall growth started at the solidified droplet and developed downwards. Only the sidewalls at the solidified droplet side can be covered by the new-grown VS deposition, because at this high growth temperature, the low-energy sidewalls cannot have lateral growth without the assistance of new atomic steps or facets. This model can be further supported by the observation from Fig. 3-12c. The NWs with high doping tend to have an elongated cross-section, making them look like nanoplates. Besides, as can be seen in Fig. 3-9, the cluster has a lower P content than that of NWs, the VLS- and VS- grown GaAsP material have different phosphorus contents. This can lead to the lattice mismatch and uneven strain

distribution and hence cause bending of the NWs. But for GaAs NWs, due to absence of strain, the NWs do not show bending morphology as can be seen in Fig. 3-12. By using this model, a switch of NW growth direction has been achieved by introducing Be doping halfway during the NW growth, which can be seen in Fig. 3-15.

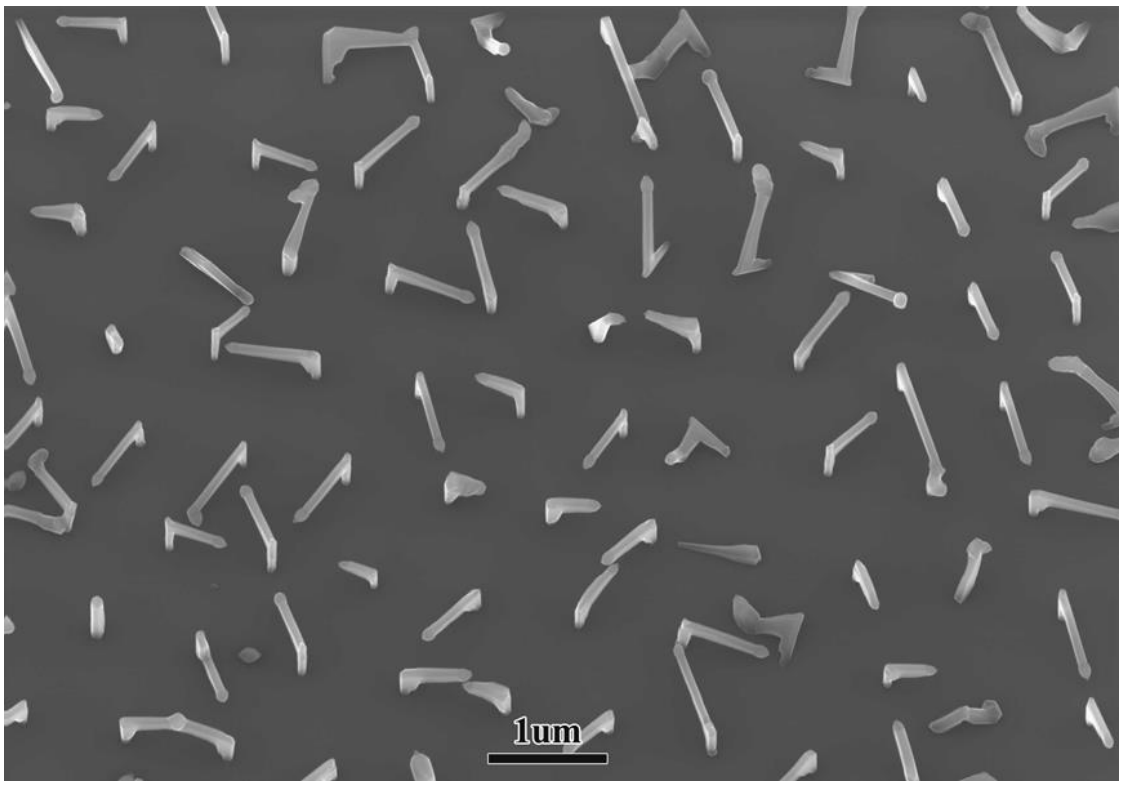

Figure 3-15. SEM image of L-shaped NW growth with introducing high Be doping concentration half-way during the NW growth.

3.3.8 Droplet Consumption

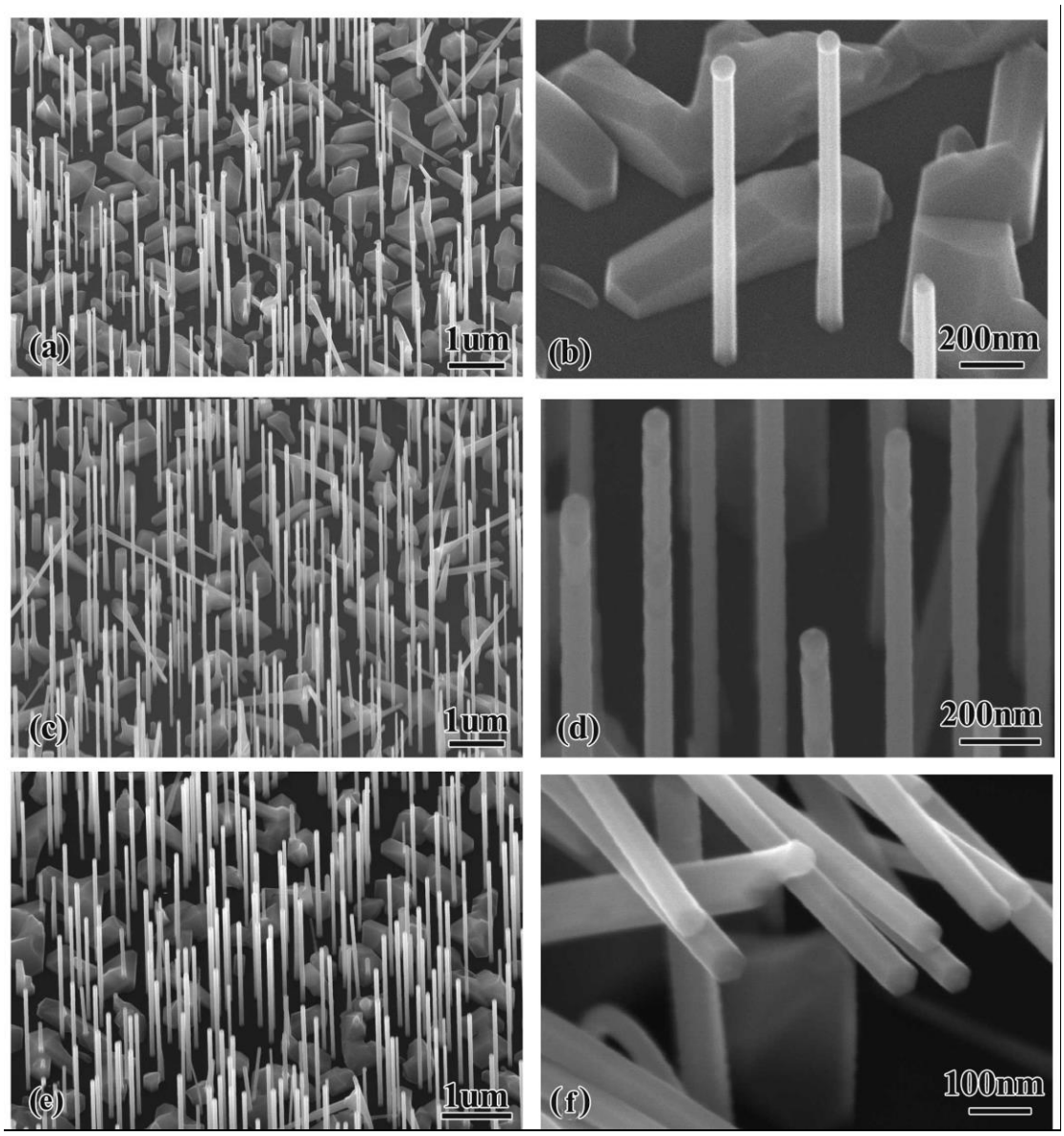

Figure 3-16. SEM image of GaAs NWs (a) (b) without droplet solidification; (c) (d) with droplet solidification at growth temperature; (e) (f) with droplet solidification at quick temperature decrease right after the NW growth.

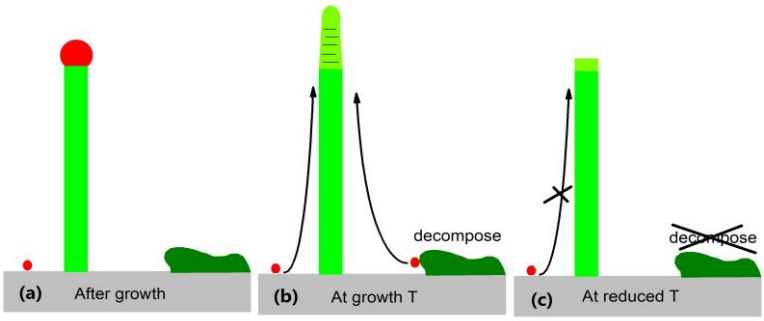

Figure 3-17. Illustration of NWs (a) without droplet solidification; (b) with droplet solidification at growth temperature; (c) with droplet solidification at quick temperature decrease right after the NW growth.

The self-catalysed NW can consume the catalyst droplet to avoid them affecting the shell growth. Therefore, the NW droplet consumption was studied. After the NW growth, the Ga droplet consumption was under an As flux of 6×10^{-7} Torr with the Ga flux closed. Two droplet consumption methods were studied. For one sample, the droplet was consumed by remaining at the growth temperature for 10 minutes before decreasing the wafer temperature. For the other one, the wafer temperature was dropped right after the NW growth. As can be seen in Fig. 3-16a and b, before the droplet consumption, the NW has a droplet at its tip with a size a bit larger than the NW diameter. The NW sidewalls are very smooth. After droplet consumption at the growth temperature for 10 minutes, the droplet disappeared which can be seen in Fig. 3-16c and d. However, the top part of the NW has a slightly gradually reduced diameter with rough surface, indicating the shrinkage of the droplet and the formation of the defects during the droplet consumption. Moreover, the NW has a curved tip. All these suggest continued NW growth during the droplet consumption. In contrast, the NWs with the droplet consumed at a reduced wafer temperature have a flat tip, smooth sidewalls, and a non-shrunk diameter all the way to the tip (Fig. 3-16f and g). The apparent difference between these two

samples can be explained by the model suggested in Fig. 3-17. After the NW growth, there is still quite a lot of Ga adatoms on the wafer surface and the NW sidewalls. These Ga adatoms can still diffuse to the Ga droplet during the Ga consumption if the wafer temperature was kept the same as the NW growth temperature. Moreover, reduction of the As flux from 3.7×10^{-6} Torr to 6×10^{-7} Torr can significantly reduce the chemical potential of the vapour phase. With the wafer temperature that is higher than the GaAs decomposition temperature, the clusters deposited on the wafer surface can decompose to release a lot of Ga atoms. These atoms can also diffuse to the droplet and contribute to the NW elongation. As a result, the droplet shrank gradually and eventually led to the diameter reduction and curved tip. With the wafer temperature rapidly reduced when the droplet consumption starts, the adatom diffusion length and cluster decomposition can be greatly reduced. This can cut the Ga supply of the droplet and avoid the continued NW growth after closing the Ga flux. The shell, grown on core NWs with the droplet consumed at a reduced wafer temperature, can have good morphology, especially the NW tip (Fig. 3-18).

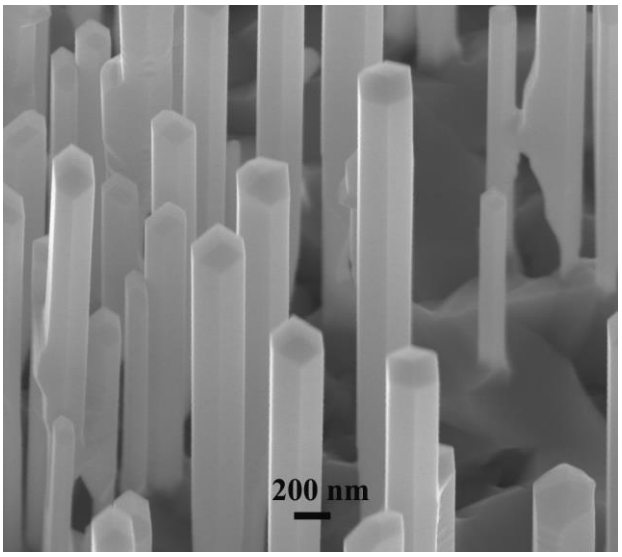

Figure 3-18. SEM image of core-shell GaAs NWs.

3.3.9 Uniformity Control

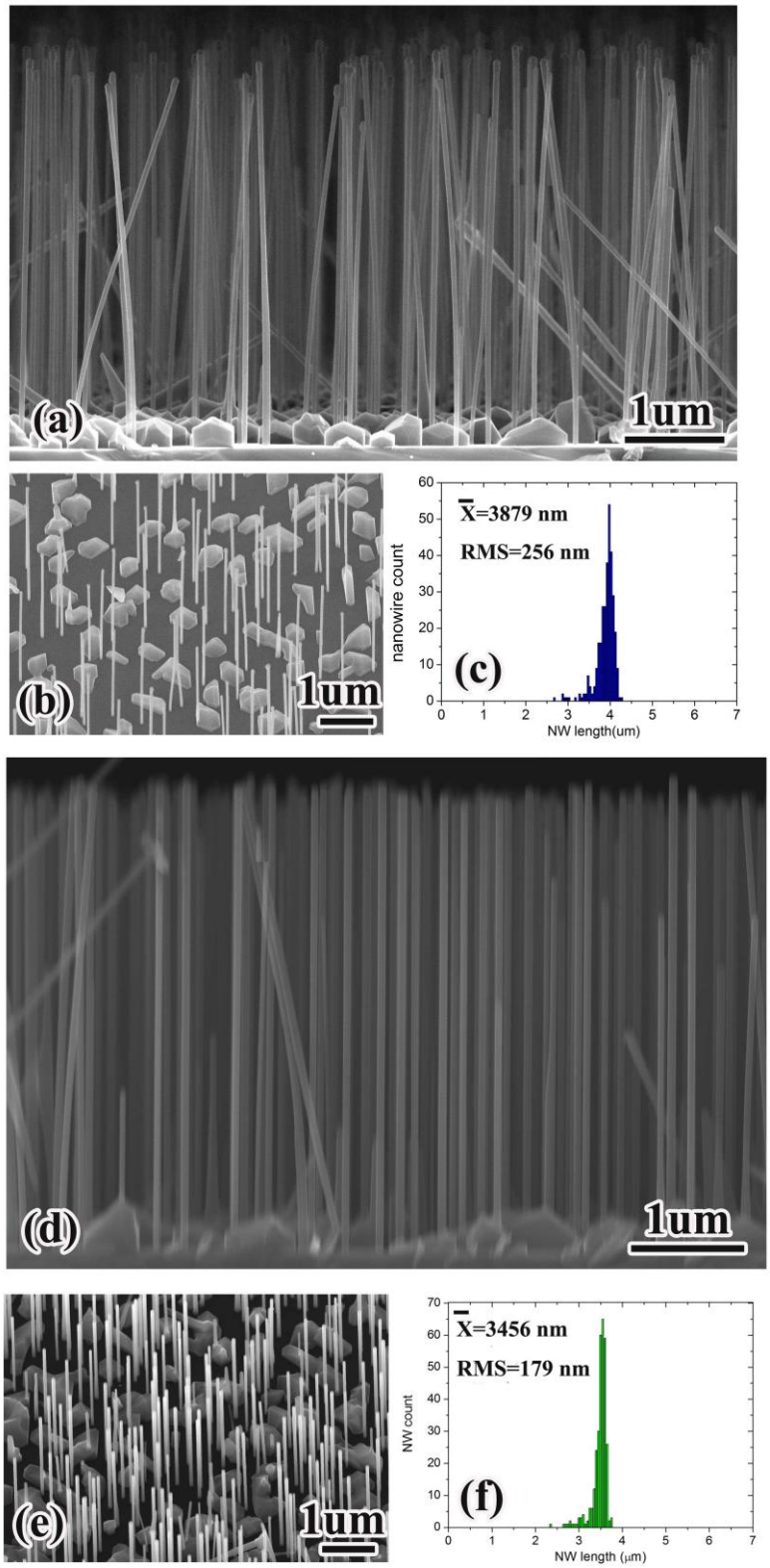

Figure 3-19. Side view, 25° tilted SEM images and NW length summation of uniform (a)~(c) GaAsP NWs (d)~(f) GaAs NWs.

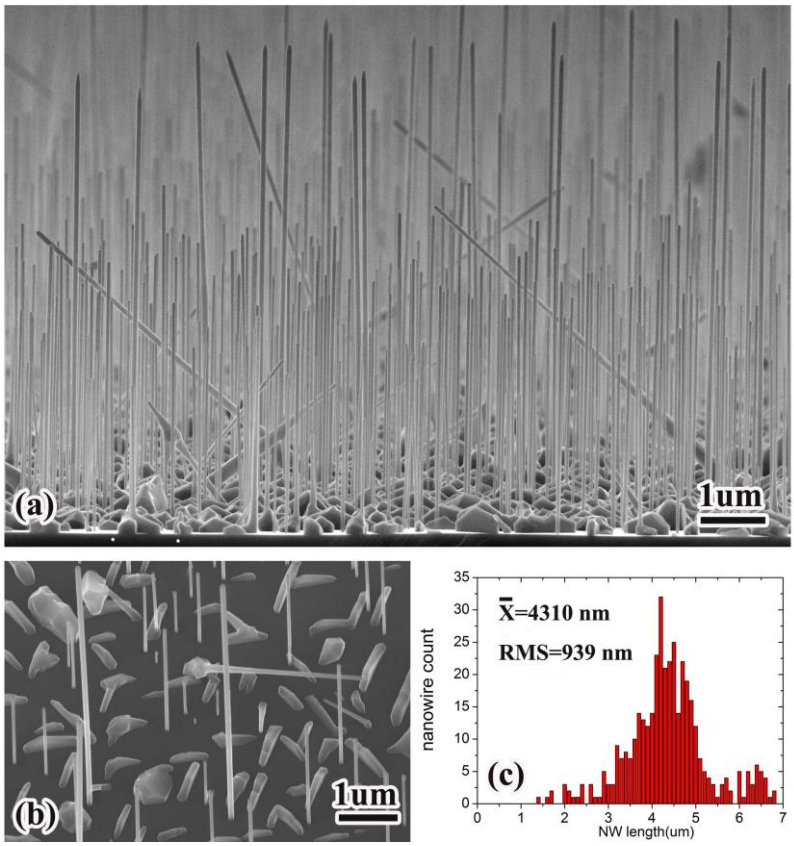

Figure 3-20. Side view, 25° tilted SEM images and NW length summation of GaAsP NWs with 5 mins GaAs growth at the initial stage.

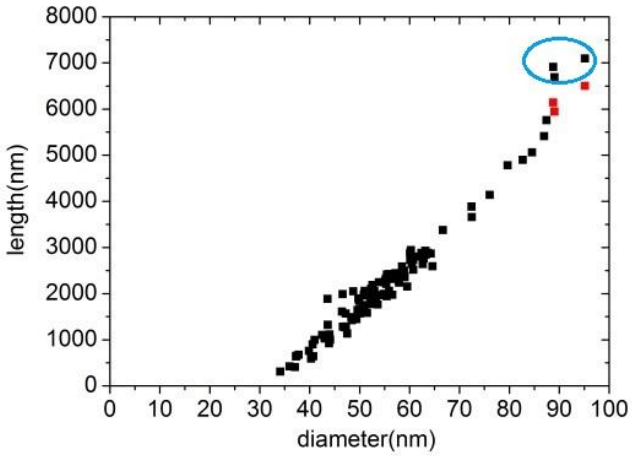

Figure 3-21. NW length as a function of diameter of GaAsP NWs shown in Fig. 3-19a~c. The three red dots are the corrected data from the three measurements shown in the blue circle by reducing a length that corresponds to 5-min growth.

NW uniformity control is critical for NW applications. In some cases, it demands NWs with good uniformity, such as to facilitate the device fabrication; while in some other cases, it needs NWs with low uniformity, such as the requirement for strong light scattering. Uniform NWs can be achieved by keeping the vapour chemical potential (V/III ratio) constant from the beginning to the end of the NW growth. As can be seen in Fig. 3-19, both the GaAs and GaAsP NWs have length deviation of ~5%. The non-uniform NWs can be grown with a disturbed vapour chemical potential. For example, introduction of low vapour chemical potential GaAs growth before the high vapour chemical potential GaAsP growth can produce NWs with length deviation of ~22% shown in Fig. 3-20. In addition, uniform NWs also have uniform diameters, while the non-uniform NWs show a linear diameter-length relationship, which can be seen in Fig. 3-21.

The NW uniformity control could be explained by the model proposed in Fig. 3-22. At the beginning of the GaAs stem growth, the substrate surface had no material deposition, which is beneficial for formation of droplets with comparatively uniform diameters. Because growth temperature was ~10 °C higher than conventional GaAs NW growth, droplets for the GaAs stem growth were quite large and hence led to NWs with large diameter (~90 nm). When the growth is switched to GaAsP growth, introduction of P flux can significantly increase chemical potential of the vapour phase. This can promote formation of a second batch of droplets. Due to strong competition and interference from the first−batch GaAs stems and/or the parasitic−grown clusters, inferior Ga collection environment made the second−batch droplets much smaller and non-uniform. During the subsequent NW growth, the strong GT effect gave the smaller droplets higher vapour pressures. As a result, the effective supersaturation inside is lower, making them

slower in nucleation rate and hence shorter in length. Therefore, droplet size distribution governs the NW uniformity. Consequently, based on this model, it is important to keep a constant chemical potential of the vapour phase for the formation of uniform droplet size and hence achieving uniform NW growth.

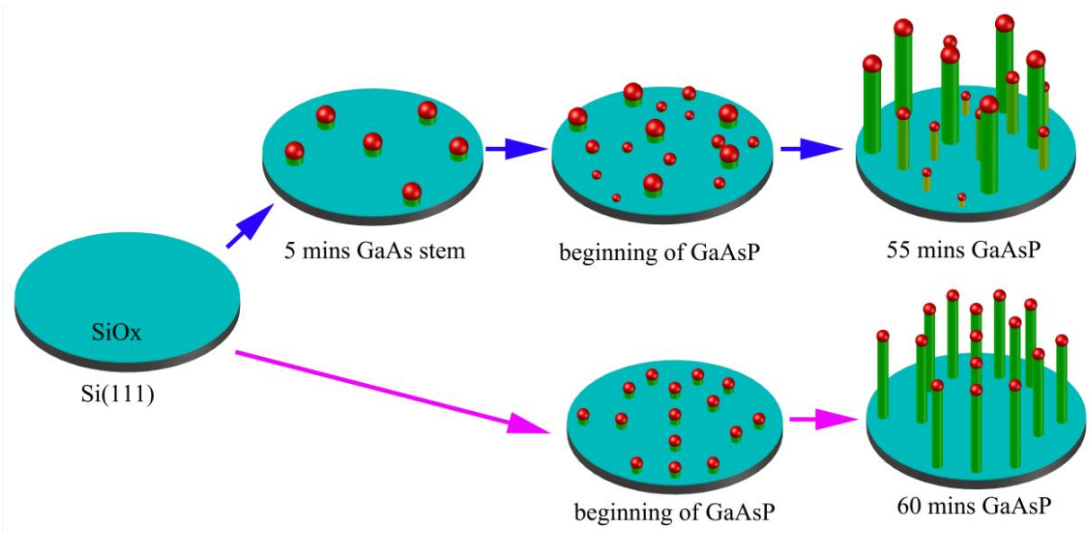

Figure 3-22. Illustration of the NW uniformity control during the NW growth.

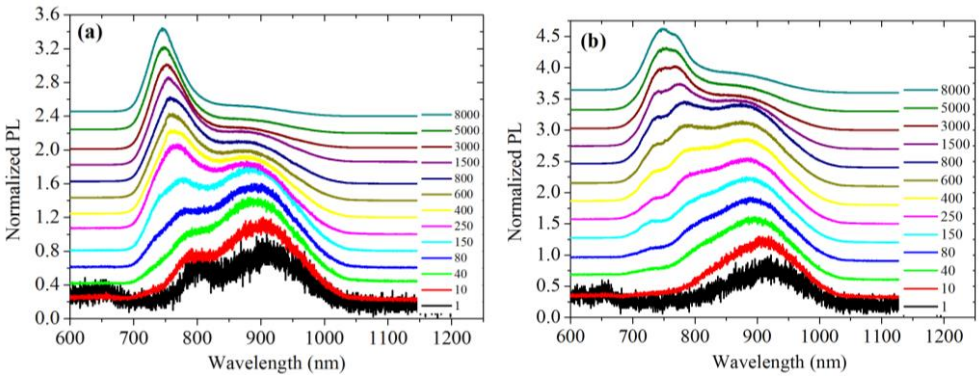

Figure 3-23. 10K power−dependent PL measurement of NWs from (a) Figure 3-19a and (b) Figure 3-20 samples.

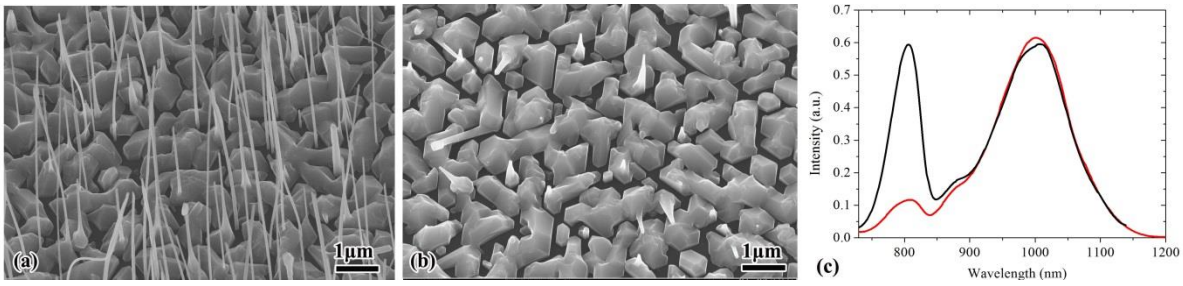

Figure 3-24. SEM images of GaAsP NW sample (a) before and (b) after the NW removal by ultrasonic bath. (c) Room−temperature PL measurement of the samples from (a) and (b).

The optical properties of uniform and non-uniform GaAsP NWs were characterized by PL measurements. Two major peaks were observed in both samples as can be seen in Fig. 3-23. One peak is around 750 nm at 10 K. The intensity of this peak is much stronger at high excitation powers, but decreased much faster with the excitation power compared with the other peak. Emissions from NWs should be the major contribution to this peak. The high surface−to−volume ratio makes NWs suffer from high−density surface states. Therefore, at low excitation power, most of the generated carriers were consumed rapidly at the surface states through non−radiative recombination. This causes them to have low emission intensity. However, NWs have a very good crystal quality with low defect density, especially no threading dislocations that can contribute to the non−radiative recombination. Therefore, as the surface states were getting saturated with increase of excitation power, the emission efficiency and hence PL intensity can be increased rapidly. It needs to be mentioned that the peak from the non-uniform GaAsP NWs is much broader than that of the NWs without GaAs stems. This could be because non-uniform GaAsP NWs have a large variation in size and composition. Moreover, the spectra from non-uniform GaAsP NWs are actually merged from two small peaks. This could be explained by their bi−modal NW distribution. The other peak is around 920 at the low temperature. It is weaker but comparatively less sensitive

to excitation power compared with that of the 750−nm peak. In order to check the origin of this peak, GaAsP NWs were grown at ~630°C to produce NWs as well as high density parasitic clusters. Room−temperature PL measurement was performed on the sample before (Figure 3-24a) and after (Figure 3-24b) NW removal. As can be seen in Figure 3-24c, at room−temperature, this peak is centred at around 1000 nm. Before and after the NW removal, the intensity of this peak did not change much. In contrast, the NW peak decreased dramatically. Therefore, the parasitic grown clusters should be the major origin of the 1000−nm emission. It could be due to defects caused by the group−III rich growth environment, such as the Ga anti−site defects and/or the group−V Schottky defect. [41-43]

3.4 Conclusion

Self-catalyzed GaAsP NWs were grown on Si(111) substrates using MBE. Introduction of P can greatly increase the nucleation rate and lead to failure of GaAsP NW growth. The V/III flux ratio was found to be more important to achieve NW growth than the growth rate. A moderate V/III flux ratio is important to get good NW morphology and crystal quality. NWs with a uniform diameter along the whole NW length can be achieved by adjusting the V/III ratio for a wide range of growth rates. These NWs have an almost pure ZB phase with only a few defects. The growth temperature is also critical for achieving successful NW growth. The window of the growth temperature was found to be very narrow, possibly less than 10 °C. Too high growth temperature can lead to suppression of the NW growth, while too low growth temperature tends to promote cluster growth, which can also affect the NW growth. The P content in the NWs can be controlled in range of 10% to 75%, which can give

a large degree of freedom for the device structure design. The incorporation coefficient of P was found to be almost three times as much as that of As, which could be due to the group-III element rich growth condition and stronger nucleation feature of P. The p-type NW doping was also investigated. Using Be as dopant can lead to sidewall wetting and solidification of the droplet when doping density is too high, which could be due to changes in droplet surface energy. A Be accumulation model in the droplet was proposed, which suggests that the NW morphology degrade happens when the Be concentration in the droplet reaches a high enough level. Droplet consumption was also studied after the NW growth. Low temperature is very helpful for achieving good NW morphology, which could be due to significantly reduced refilling of the Ga droplet. NW uniformity control was also investigated via changing the chemical potential of the vapour phase (V/III flux ratio). Length deviation ranging from 5% to 22% has been demonstrated. The discoveries here not only open up new perspectives for the research of GaAsP NW devices working in visible wavelength, but also provide valuable information for development of other III-V-V type of NWs.

3.5 References

1. LaPierre R 2011 Journal of Applied Physics 110 014310
2. Walter M G, Warren E L, McKone J R, Boettcher S W, Mi Q, Santori E A and Lewis N S 2010 Chemical Reviews 110 6446
3. Mohseni P K and LaPierre R R 2009 Nanotechnology 20 025610.
4. Mohseni P K, Maunders C, Botton G A and LaPierre R R 2007 Nanotechnology 18 445304.

5. Svensson C P T, Seifert W, Larsson M W, Wallenberg L R, Stangl J, Bauer G and Samuelson L 2005 Nanotechnology 16 936.

6. Holm J V, Jørgensen H I, Krogstrup P, Nygård J, Liu H and Aagesen M 2013 Nature Communication 4 1498.

7. Tchernycheva M, Rigutti L, Jacopin G, de Luna Bugallo A, Lavenus P, Julien F H, Timofeeva M, Bouravleuv A D, Cirlin G E and Dhaka V 2012 Nanotechnology 23 265402.

8. Mohseni P K, Rodrigues A D, Galzerani J C, Pusep Y A and LaPierre R R 2009 Journal of Applied Physics 106 124306.

9. Joyce H J, Gao Q, Tan H H, Jagadish C, Kim Y, Zhang X, Guo Y and Zou J 2007 Nano Letters 7 921

10. Bar-Sadan M, Barthel J, Shtrikman H and Houben L 2012 Nano Letters 12 2352

11. Perea D E, Allen J E, May S J, Wessels B W, Seidman D N and Lauhon L J 2006 Nano Letters 6 181

12. Breuer S, Pfüller C, Flissikowski T, Brandt O, Grahn H T, Geelhaar L and Riechert H 2011 Nano Letters 11 1276

13. Rieger T, Lepsa M I, Schäpers T and Grützmacher D 2013 Journal of Crystal Growth 378 506

14. Munshi A M, Dheeraj D L, Todorovic J, van Helvoort A T, Weman H and Fimland B-O 2013 Journal of Crystal Growth 372 163

15. Krogstrup P, Popovitz-Biro R, Johnson E, Madsen M H, Nygård J and Shtrikman H 2010 Nano Letters 10 4475

16. Yu X, Wang H, Lu J, Zhao J, Misuraca J, Xiong P and von Molnár S 2012 Nano Letters 12 5436

17. Zhang Y, Aagesen M, Holm J V, Jørgensen H I, Wu J and Liu H 2013 Nano Letters 13 3897

18. Hertenberger S, Rudolph D, Bichler M, Finley J J, Abstreiter G and Koblmuller G 2010 Journal of Applied Physics 108 114316

19. Hua B, Motohisa J, Kobayashi Y, Hara S and Fukui T 2008 Nano Letters 9 112

20. Rudolph D, Hertenberger S, Bolte S, Paosangthong W, Spirkoska D, Döblinger M, Bichler M, Finley J J, Abstreiter G and Koblmüller G 2011 Nano Letters 11 3848

21. Glas F 2010 Journal of Applied Physics 108 073506

22. Ek M, Borg B M, Johansson J and Dick K A 2013 ACS Nano 7 3668

23. Krogstrup P, Curiotto S, Johnson E, Aagesen M, Nygård J and Chatain D 2011 Physical Review Letters 106 125505

24. Wacaser B A, Dick K A, Johansson J, Borgström M T, Deppert K and Samuelson L 2009 Advanced Materials 21 153

25. Glas F, Harmand J-C and Patriarche G 2007 Physical Review Letters 99 146101

26. Couto Jr O D D, Sercombe D, Puebla J, Otubo L, Luxmoore I J, Sich M, Elliott T J, Chekhovich E A, Wilson L R, Skolnick M S, Liu H Y and Tartakovskii A I 2012 Nano Letters 12 5269

27. Sourribes M J L, Isakov I, Panfilova M, Liu H and Warburton P A 2014 Nano Letters 14 1643

28. Wilhelm C, Larrue A, Dai X, Migas D and Soci C 2012 Nanoscale 4 1446

29. Gil E, Dubrovskii V G, Avit G, André Y, Leroux C, Lekhal K, Grecenkov J, Trassoudaine A s, Castelluci D and Monier G 2014 Nano Letters 14 3938

30. Gudiksen M S, Lauhon L J, Wang J, Smith D C and Lieber C M 2002 Nature 415 617

31. Yamashita T, Akiyama T, Nakamura K, and Ito T 2010 Phys. E (Amsterdam, Neth.) 42 2727.

32. Chiaramonte T, Tizei L H, Ugarte D and Cotta M A 2011 Nano Letters 11 1934

33. Shu-Dong W, Li-Wei G, Wen-Xin W, Zhi-Hua L, Ping-Juan N, Qi H and Jun-Ming Z 2005 Chinese Physics Letters 22 960

34. Arthur J R and LePore J J 1969 Journal of Vacuum Science and Technology 6 545

35. LaPierre R R, Robinson B J and Thompson D A 1996 Journal of Applied Physics 79 3021

36. Hou H, Liang B, Chin T and Tu C 1991 Applied Physics Letters 59 292

37. Vasil'ev V P and Gachon J-C 2006 Inorganic Materials 42 1176

38. Matsushima Y and Gonda S-i 1976 Japanese Journal of Applied Physics 15 2093

39. Yiying W, Fan R and Yang P 2002 Nano Letters 2 83

40. Wallentin J, Ek M, Wallenberg L. R, Samuelson L, Deppert K and Borgström M T 2010 Nano Letters 10 4807

41. Marrakchi, G.; Kalboussi, A.; Bremond, G.; Guillot, G.; Alaya, S.; Maaref, H.; Fornari, R. Journal of applied physics, 1992, 71, 3325−3329

42. Heinke, W.; Queisser, H. J. Physical Review Letters 1974, 33, 1082.

43. Bugajski, M.; Ko, K. H.; Lagowski, J.; Gatos, H. C. Journal of applied physics 1989, 65, 596-599

Chapter 4:

GaAsP Core-Shell Nanowire Structure

4.1 Introduction

Compared with thin film structures, the NWs possess a lot of novel crystallographic,[1,2] photonic,[3-5] electric[6,7] and mechanical[8] properties which could bring breakthroughs in a wide range of fields.[9-13] In order to make good use of these merits, it is necessary to grow advanced structure design. The radial core-shell geometry is of great importance to achieve band structure engineering for construction of high-efficiency NW emitters and photovoltaic devices.[14-18] In particular, the ternary and quaternary III-V semiconductor shells can provide large composition and lattice tunability, which are important for a wide range of applications. However, due to the non-planar surface of the NWs, shell growth is much more complex compared with thin film technique. The NW surface curvature has been reported to be a cause for phase segregation during the III-III-V ternary shell growth, such as AlGaAs shell growth.[19-23] For example, Rudolph *et al*.[19] observed six Al-rich strips along the six corners of

a hexagonal AlGaAs shell. The Al-rich strip has an Al content that is double that of the body of the AlGaAs shell (Fig. 4-1). Similar phenomena have also been observed in AlInP NW shells.[24,25] The phase segregation was found to have a 3-fold symmetry, which is demonstrated in the AlGaAs (Fig. 4-2)[26] and InGaAs (Fig. 4-3)[27] NW growth.

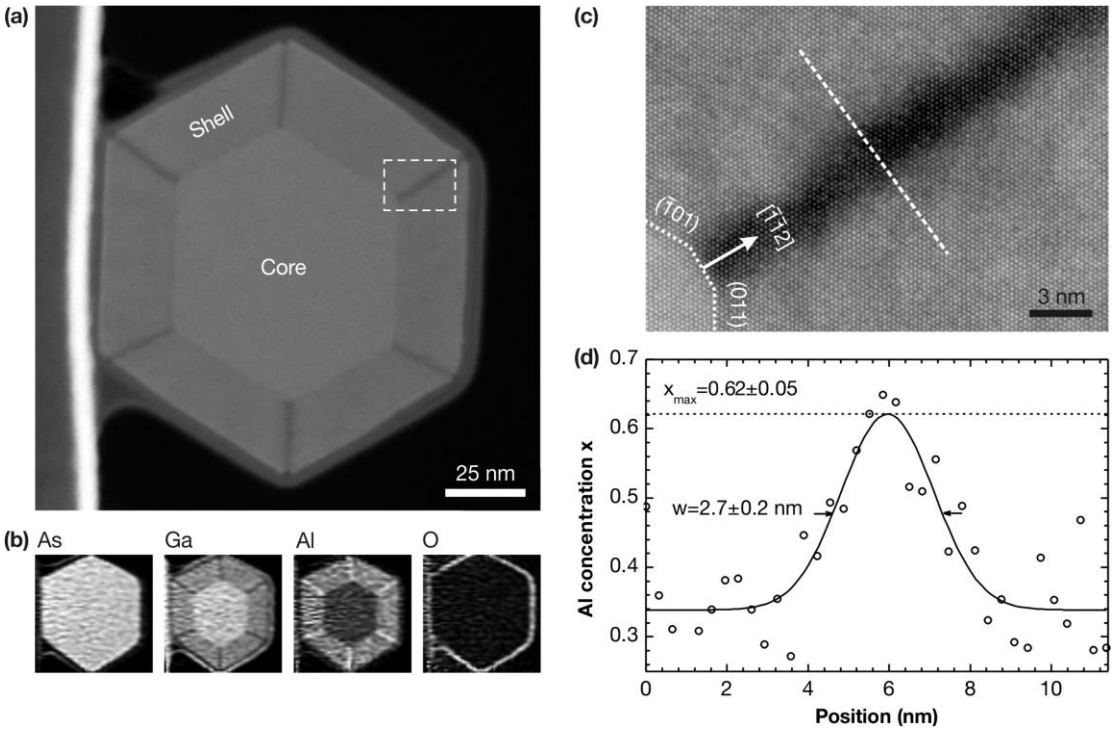

Figure 4-1 (a) Cross-section STEM image of a GaAs−Al0.3Ga0.7As core−shell NW. (b) Elemental maps of As, Ga, Al, and O in the NW cross-section measured by spatially resolved XEDS. (c) Higher magnification STEM image shows the details of an Al-rich stripe indicated by the dashed square in (a). (d) Al content profile of the Al-rich stripe indicated in (c). Reprinted with permission from 19. Copyright 2013 American Chemical Society.

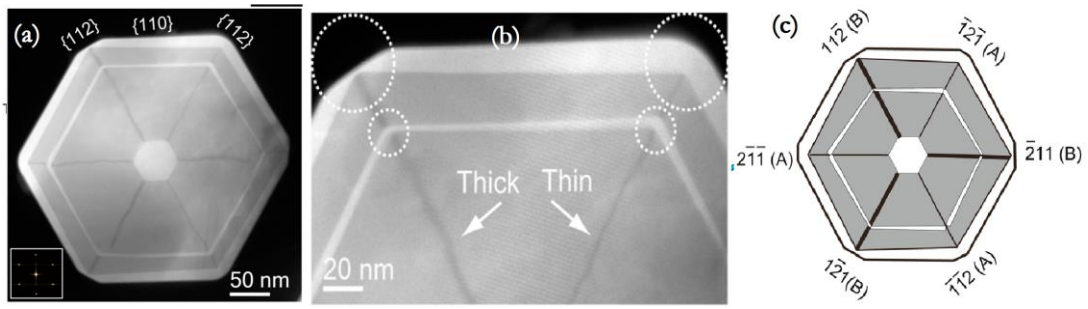

Figure 4-2. (a) Low-resolution and (b) higher-resolution Cross-section STEM image of a GaAs/AlGaAs NW. (c) Schematic summary of the relation between the facet polarity and the Al-rich band symmetry. Reprinted with permission from 26. Copyright 2013 American Chemical Society.

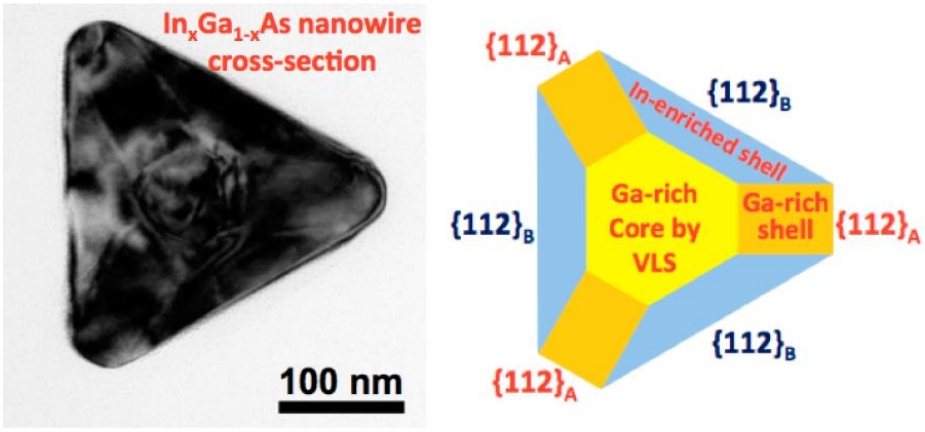

Figure 4-3. (a) Cross-section TEM image of an InGaAs NW. (b) Illustration of the composition distribution and the side facet polarities. Reprinted with permission from 27. Copyright 2013 American Chemical Society.

These compositional inhomogeneity can change local properties, especially the band structure, doping efficiency and strain. This can greatly influence the effective mass and transport of carriers and hence device performance. On the other hand, control of the phase segregation can be very helpful in fabricating novel structures. Heiss *et al.*[28] demonstrated fabrication of AlGaAs quantum dots in the shell of the NWs by this mechanism (Fig. 4-4). Formation of these quantum dots does not need assistance of strain, which is different from

the Stranski–Krastanow mode grown dots.[29] This quantum dot fabrication method allows more freedom in quantum dot material choice and hence band structure engineering and device structure design. Therefore, a study of the compositional inhomogeneity and the underlying formation mechanisms can provide valuable information for control of these phenomena, so as to make good use of them and avoid their potential adverse effects.

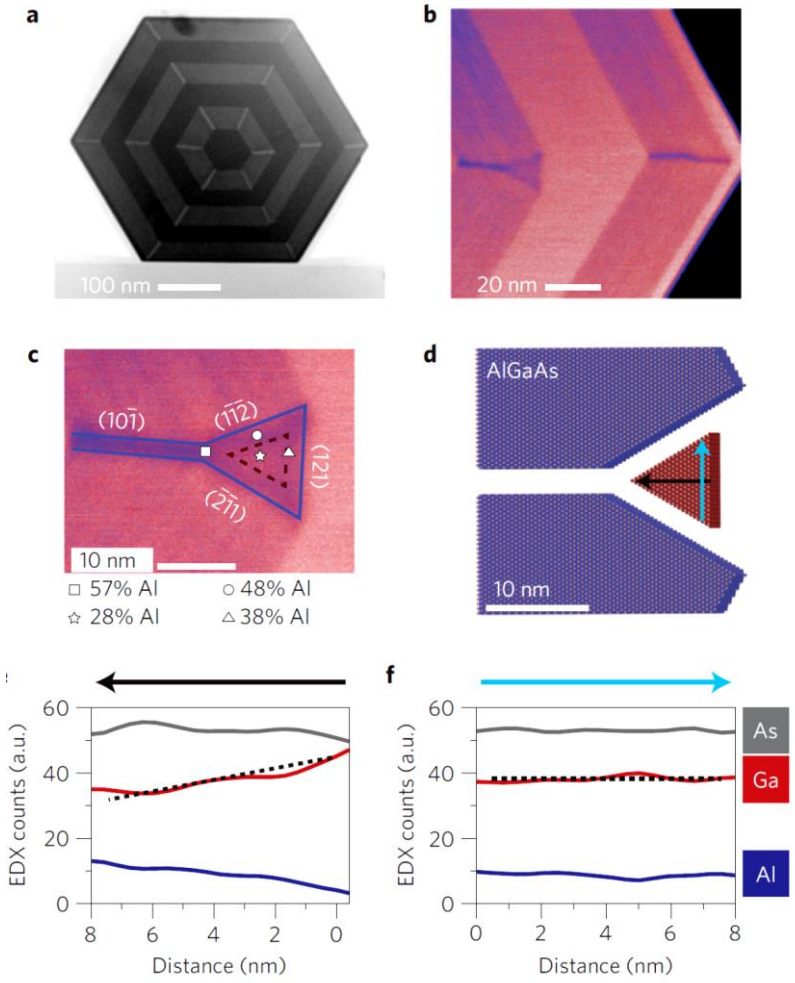

Figure 4-4. (a) Overall and (b) (c) zoom-in Cross-section TEM of a GaAs/AlGaAs core-shell NW. (d) illustration of the Al-rich quantum dot structure shown in (c). (e) and (f) EDX composition profile shown in (d). Adapted by permission from Macmillan Publishers Ltd: Nature Materials,[28] copyright 2013.

In this Chapter, the investigation of GaAsP shell growth is presented. The results suggest

that slow shell growth rate is beneficial for achieving good morphology and crystal quality, due to uniform adatom distribution. The composition distribution of these core-shell GaAsP NWs was also studied. An interesting quasi-3-fold compositional symmetry was observed for the first time in the III-V-V core-shell NW. We propose it is related to sidewall surface chemical potential and polarity-induced adatom bonding energy. In addition, passivation effect of InGaP on these core-shell NWs was also demonstrated with improved optical properties for GaAsP NWs.

4.2 Experiment

The GaAsP NWs were grown on 380-μm-thick p-doped Si (111) substrates. The self-catalysed core NWs were grown with a Ga beam equivalent pressures of 8.72×10^{-8} Torr (corresponding to 0.285 ML/s) and substrate temperature of ~640 °C as measured by a pyrometer. The V/III and the P/(As+P) ratios were 40 and 0.12, respectively. This growth condition led to production of $GaAs_{0.8}P_{0.2}$ core NWs. After the core NW growth, the Ga flux was closed but the As and P fluxes were left on. This operation consumes the Ga droplet by crystalizing into the NW and hence stops the VLS growth. Subsequently, if it is not indicated otherwise, shell growth was carried out at a Ga beam equivalent pressures of 8.72×10^{-8} Torr and substrate temperature of 460~500 °C. The V/III ratio and P/(As+P) ratios are 50 and 31~35, respectively. The nominal shell composition is $GaAs_{0.8}P_{0.2}$, which is the same as the core. The InGaP passivation layer was later grown on the core-shell GaAsP NWs at the same temperature as the GaAsP shell growth. During the 12-minute InGaP growth, the Ga, In and V/III were 8.72×10^{-8} Torr, 5×10^{-8} Torr and 60, respectively. The core/shell composition match

was inspected by X-ray diffraction. For lattice (composition) matched core-shell structure, the peak intensities of the core and shell should be at the same angle. The Zeiss XB 1540 FIB/SEM and JEOL-JSM-6320F SEM were used to inspect the NW morphology. The JEOL 2100 and doubly-corrected ARM200F microscopes were used to perform the TEM measurement with an operation voltage of 200 kV. For the complete NW measurement, the NWs were scraped onto a laced carbon support. The NW cross-section specimens were prepared with JEOL 4500 FIB/SEM with focused ion beam lift-out technique. Compositional analysis was performed with Oxford Instruments 80 mm^2 SDD EDX detectors with the energy-dispersive X-ray spectrometry (EDX) function.

4.3 Results and Discussion

4.3.1 Influence of Shell Growth Rate

The NW shell growth adopts the same growth mechanism as thin film growth. However, due to their 1D columnar shape, the growth parameters are quite different, especially growth rate. In order to study the influence of growth rate, two growths were performed with Ga fluxes of 8.72×10^{-8} (corresponding to 0.285 ML/s) and 2.77×10^{-7} Torr, respectively. The other parameters were the same between these two runs. The results are presented in Fig. 4-5. As can be seen in Fig. 4-5a, the NWs grown with the Ga flux of 8.72×10^{-8} Torr have smooth side facets, a uniform diameter along the whole NW length and a clean hexagonal tip. In contrast, the NWs grown with higher Ga flux have a match-stick-like morphology, indicating more deposition at the tip. The TEM measurement shows that the tip of the NW contains high density defects (Inset in Fig. 4-5b).

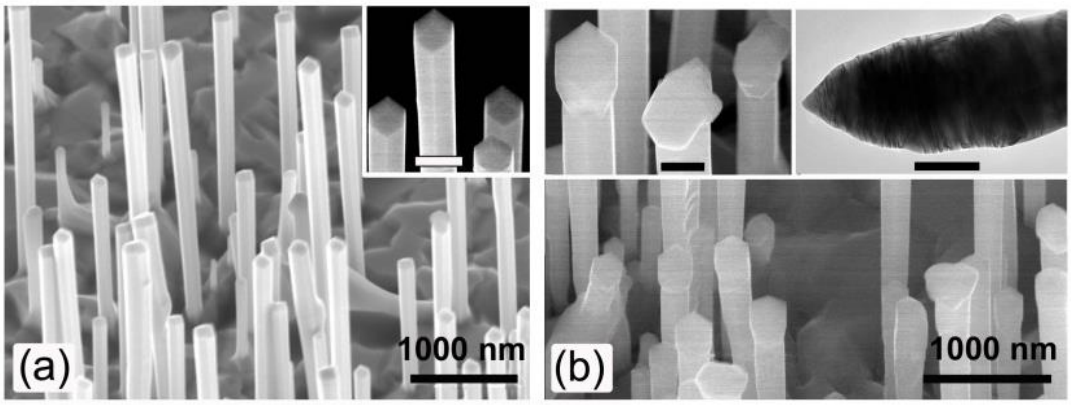

Figure 4-5. SEM images of core-shell NWs grown with Ga flux of (a) 8.72×10^{-8} and (b) 2.77×10^{-7} torr. The inset in (a) shows the enlarged tip of some NWs. Scale bar=200 nm. The insets in (b) show the SEM and TEM images of some NW tips. Scale bars=200 nm.

In the growth chamber of Veeco GEN930 MBE system, the effusion cells are angled 33° relative to the substrate normal, making the NW side facets suffer from shadow effect caused by neighbouring NWs. This can block the source beams. Therefore, the direct material flux at the NW tip part is larger as illustrated in Fig. 4-6. When the shell growth rate is slow, Ga adatoms have longer time to make a more uniform distribution along the NW length. This is beneficial for uniform VS NW shell growth and hence results in good NW morphology shown in Fig. 4-5a. For the NW shell growth with large Ga flux, fast material deposition rate can greatly reduce the adatom diffusion time. Therefore, the adatoms are incorporated into the shell lattice before they migrate far enough. This makes the NW tips grow much faster with poor crystal quality (Fig. 4-5b). Based on the apparent difference shown in Fig. 4-5, a slow shell growth rate is suggested because it is beneficial for obtaining good shell morphology.

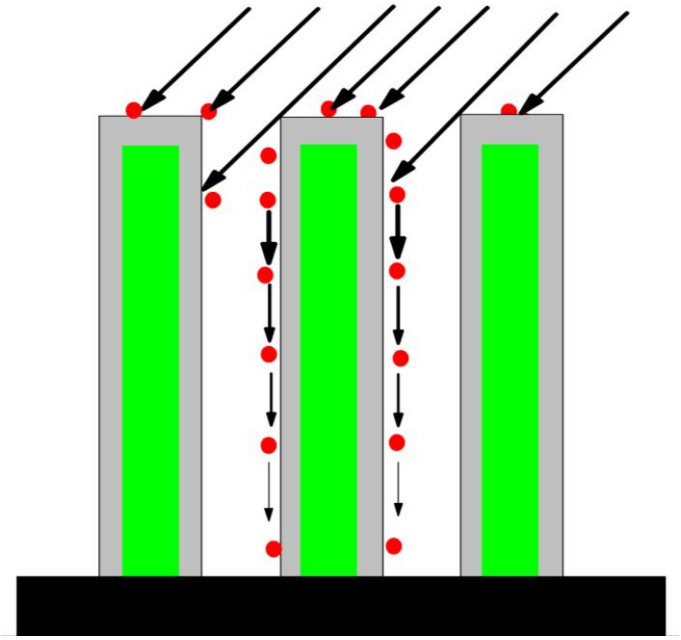

Figure 4-6. Illustration of the NW shell growth.

4.3.2 Composition Distribution of Core-Shell Nanowires

4.3.2.1 Composition Distribution of Core-Shell Nanowires

For a core-shell structure made of multicomponent materials, the radial composition distribution can greatly influence device performance. In order to obtain this information, core-shell NW cross sections were prepared with a thickness of ~70 nm by taking NWs from the sample shown in Fig. 4-7. The NWs have very smooth on side facets. Same as the core NW, the defects are mainly concentrated at the very tip and the bottom part, leaving the body part almost defect-free. As confirmed by dark field TEM and annular dark field scanning TEM (ADF-STEM) measurements shown in Fig. 4-7b and c, the twin defects are so sparse that the segment presented is completely defect-free. The shell has ZB crystal structure which is copied from the core NW.

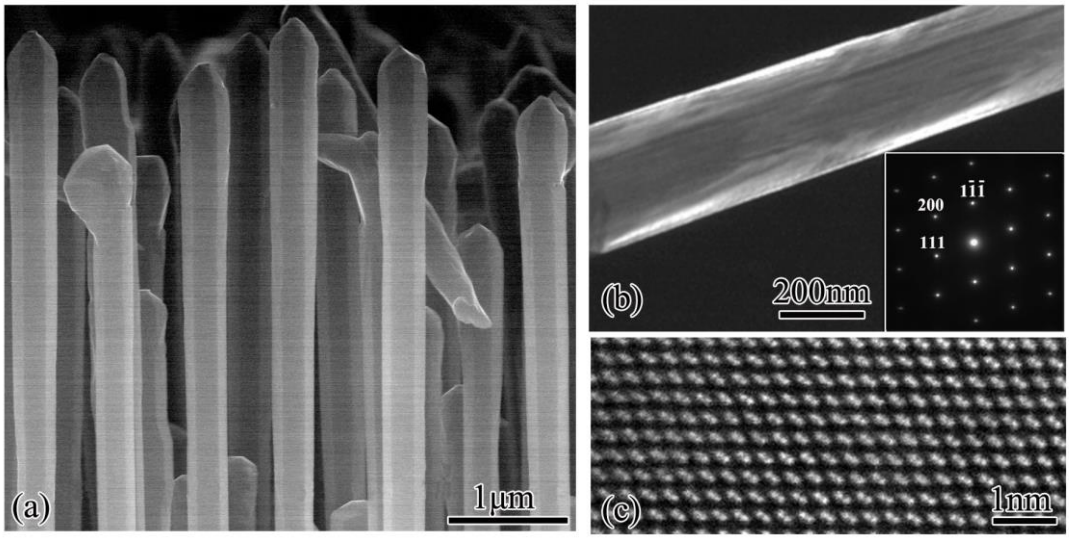

Figure 4-7. (a) Side-view SEM image, (b) Conventional DF-TEM image and (c) High-magnification annular dark field image of core-shell $GaAs_{0.8}P_{0.2}$ NWs. Inset in (b) is electron diffraction pattern. Reprinted with permission from Ref. 31. Copyright 2014 American Chemical Society.

Line element mapping was performed across a NW and the results are shown in Fig. 4-8. Composition is relatively uniform along axial direction, which reveals good composition match of the core-shell structure. In addition, in the Annular Dark Field image, shown in Fig.4-9, no clear change in contrast was observed which confirms no obvious change in composition along the NW axis.

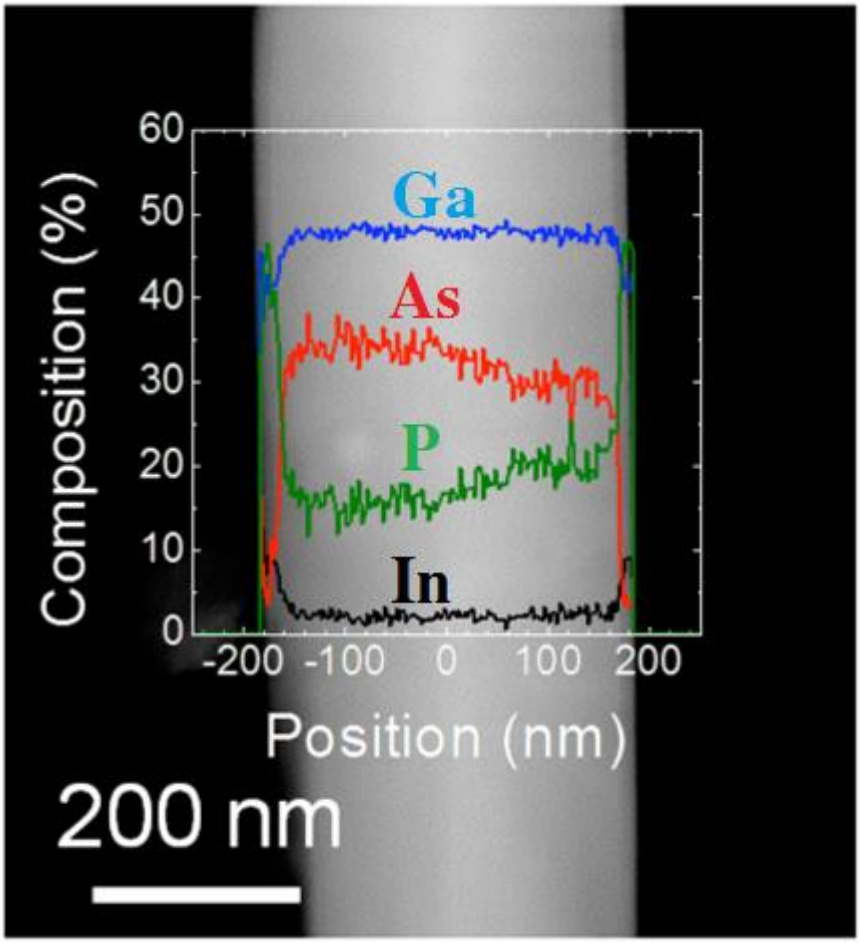

Figure 4-8. Line element mapping obtained across a core-shell NW. The element composition is normalized to the NW thickness.

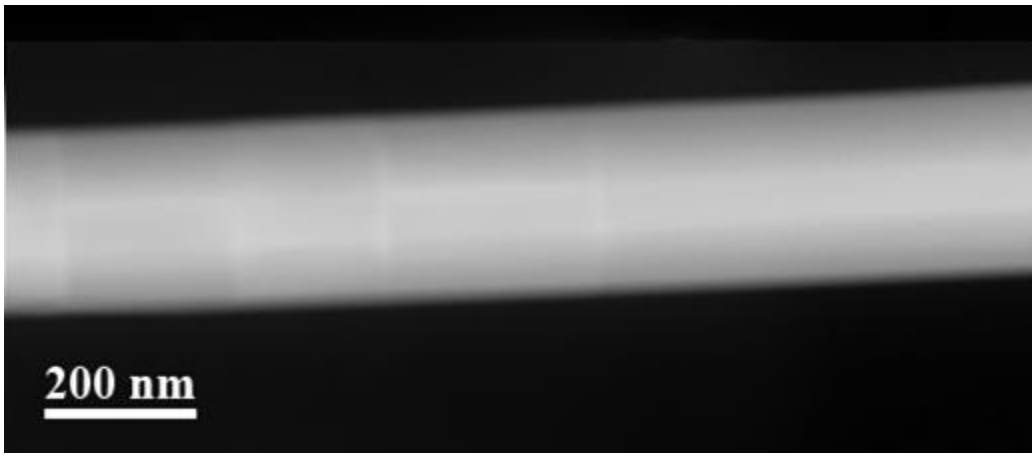

Figure 4-9. Annular Dark Field image of a core-shell NW.

In order to further investigate the composition distribution, cross-sections of the core-shell NWs were prepared by FIB/SEM (thickness ~70 nm) and examined using STEM.

As can be seen in Fig. 4-10, the core-shell structure has an approximately hexagonal shape. The irregularity of the hexagonal cross section could be due to the anisotropic source material supply. This sample was grown on an un-patterned Si substrate. The Ga droplets, formed at the beginning of the NW growth, were arranged randomly, which resulted in random distance between the NWs. As a result, source material supply to each facet of the NW was anisotropic during the shell growth. Three distinct radial dark lines/bands are running from the centre area to alternate outer vertices of the hexagon, forming a quasi-3-fold symmetry arrangement. At a higher magnification, Fig. 4-10b, these lines seem to have a zig-zag shape, alternating maybe between {112} and {101} planes. In addition, sharp, straight, bright and dark bands and blocks of material are also presented with their edges parallel to the side faces of the NW. In ADF-STEM measurement, the contrast is proportional to an exponent of the atomic number Z^m, in which the m is ~ 1.6 to 2. Therefore, the contrast difference shown in Fig. 4-10 is an indication of variations in the As/P ratio. The brighter regions correspond to higher As content due to its large atom size which can generate stronger signal during the measurement. In contrast, the darker regions are richer in P. As confirmed by the EDX line profile shown in Fig. 4-10b, P content in the dark bands regions is higher compared with the adjacent brighter regions. To further check the composition difference, the ADF-STEM image was analysed by the geometric phase algorithm. The results presented in Fig. 4-10c reveal that the dark bands are smaller in the inter-atomic spacing, which is consistent with higher P content. The lattice constants of $GaAs_{0.6}P_{0.4}$ and $GaAs_{0.8}P_{0.2}$ are respectively 0.55573nm and 0.5613 nm. Therefore, it can be seen clearly that the compositional phase segregation happened during the GaAsP shell growth.

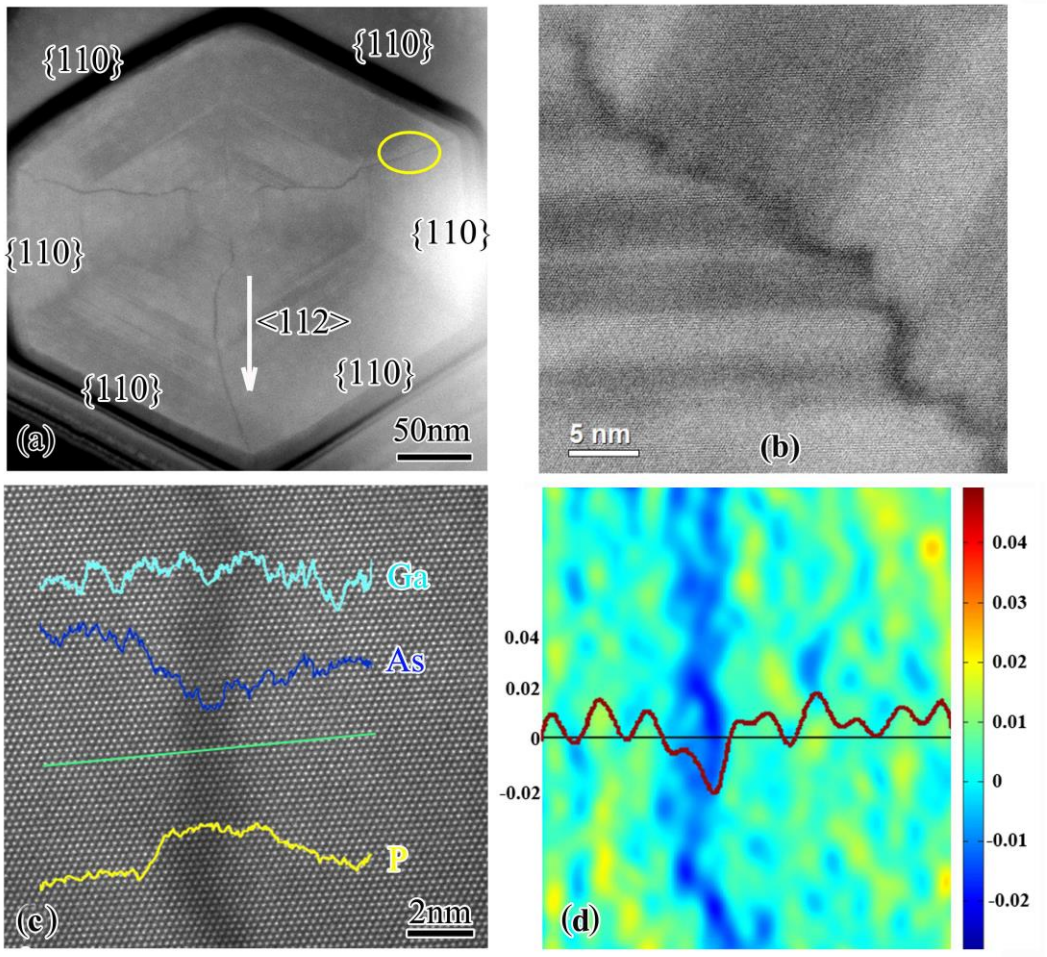

Figure 4-10. (a) ADF-STEM image of the GaAsP core-shell NW cross-section. (b) ADF-STEM image shows the detail of a dark line in the GaAsP core-shell NW cross-section. (c) High-resolution ADF-STEM of a dark band area marked by the yellow ellipse in (a). An X-ray count profile measured along the green line is overlaid. (d) Horizontal-axis strain (ε_{xx}) mapping around same area of (b). A line profile of the strain across the dark band is overlaid.

In order to find the starting point of the dark bands during the shell growth, an ADF-STEM image with a higher magnification was taken around central part that encloses the core area. As can be seen in Fig. 4-11a, there is a regular hexagon with a diameter ~50 nm

at the central region, which is uniform in composition. This can be seen more clearly in the false colour image shown in Fig. 4-11b. This hexagonal area is due to the NW core that was grown with the VLS growth mode. From Fig. 4-11, it can be seen that the dark bands originated from the outer corners of this hexagonal core and run radially. Moreover, it is interesting to observe that there are other three comparatively indistinct dark lines running radially from the other three corners of the core. They are also higher in P content compared with the adjacent brighter regions, but they are not as dark as the other three apparent dark bands, indicating a comparatively lower P content. In the 3D image of the core-shell NW pillars, these six bands are actually P-rich planes, which are connecting radially the corners of the core and the shell.

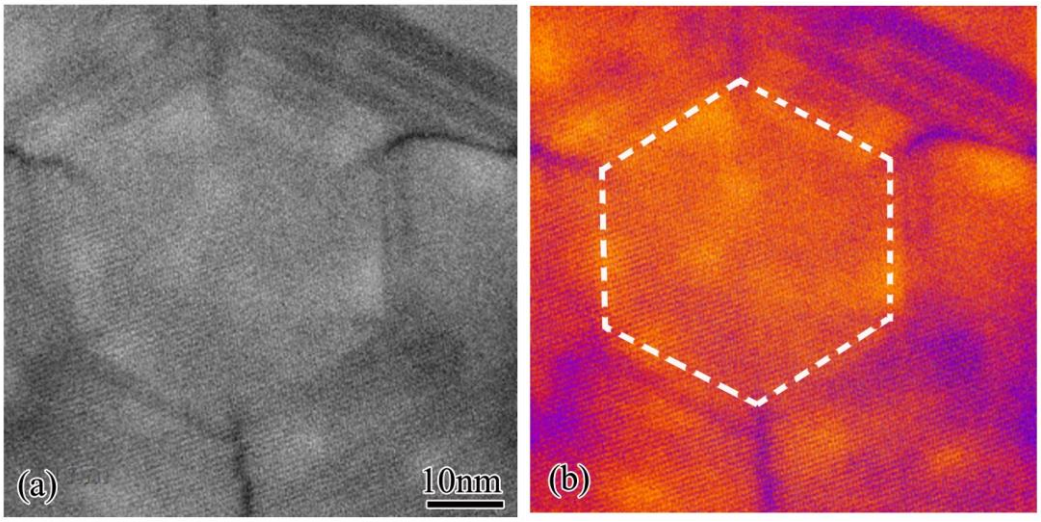

Figure 4-11. (a) ADF-STEM image of the centre region of the GaAsP core-shell NW cross-section. (b) The false colour image of (a). The white dashed hexagon is the guidance to the eye, indicating the core area.

4.3.2.2 Sidewall Facet Polarities

The core-shell NW in this study has a cubic structure, which can be seen on the inset of Fig. 4-7b. A 3-fold symmetry of the dark bands is consistent with the 3-fold symmetry of the cubic structure. Besides, when material is non-centrosymmetric, surfaces with opposite orientations, (*h k l*) and (*-h –k -l*), are different. One of them will be terminated with group-III cations; while the other with group-V anions. This is called A and B polarity, respectively.[32] But some of the surfaces are equal in the number of cations and anions. These facets are neutral, or non-polar. For example, self-catalysed NWs are commonly observed to be bounded by {110} and {112} side facets due to their low surface energy. The {110} facet is non-polar, while the {112} is polar.[26] Due to different polarity features, different growth mechanisms are expected on these side facets.

In order to check the side facet polarities of the NWs, convergent beam electron diffraction (CBED) was used. The Kikuchi pattern (Fig. 4-12a) and CBED pattern (Fig. 4-12a inset) were obtained by aligning the electron beam along the NW growth direction [111]. The NW cross section aligned to the diffraction pattern is shown in Fig. 4-12b. Then, the sample was tilted to the [112] zone axis following the 220 Kikuchi lines to obtain another CBED pattern (Fig. 4-12c). In this pattern, the simulation of the bright/dark contrast of the 111-type discs (Fig. 4-12d) can help unambiguously index the [112] and [111] patterns, which can be used to obtain the absolute orientations in the NW cross section. As can be seen in Fig. 4-12b, the distinct P-rich bands are along the <112>A directions, while the indistinct bands are in <112>B directions. This suggests that phase segregation is stronger in <112>A direction.

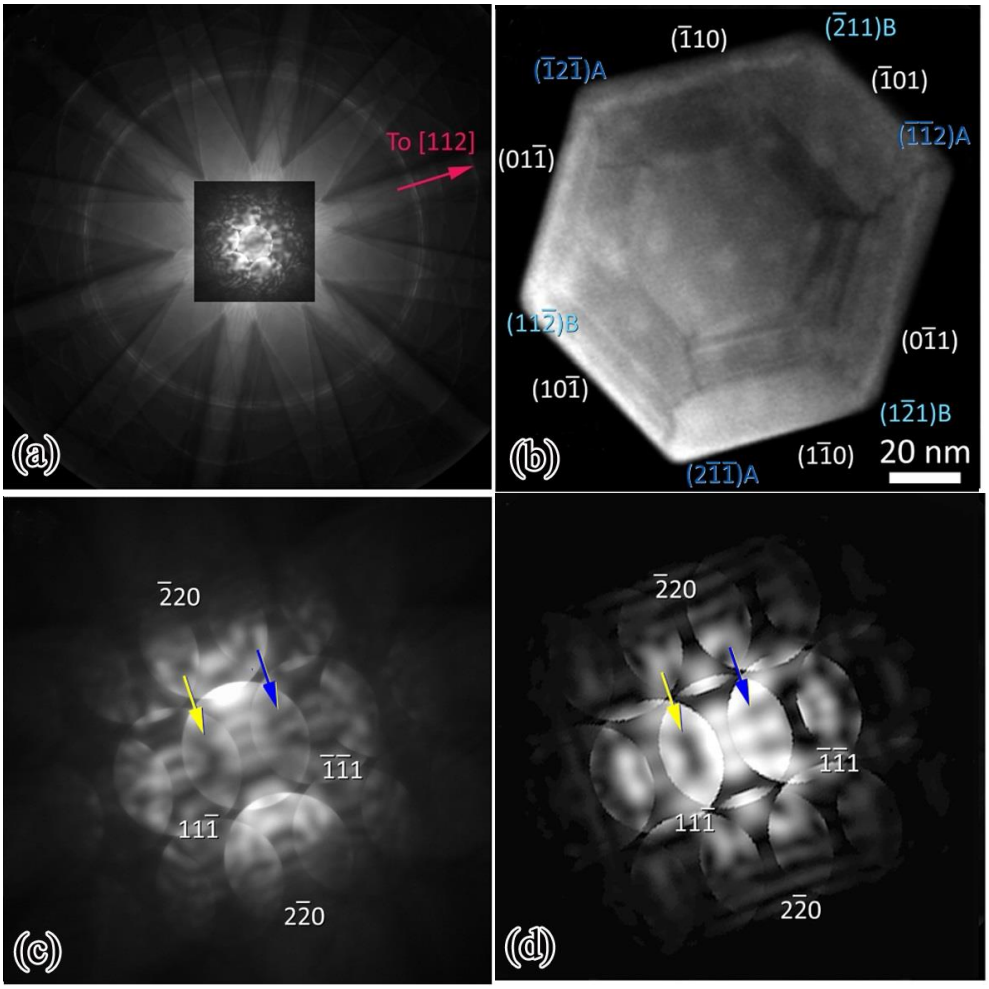

Figure 4-12. (a) Kikuchi pattern and CBED pattern (inset) obtained with the electron beam along the nanowire growth direction. (b) ADF-STEM image of the core-shell NW marked with the sidewall polarities. (c) Experimental (d) Simulated [112] CBED pattern from the GaAsP cross setion with a specimen thickness of 75nm. Bright and dark features in the polarity-sensitive 111-type discs are marked with arrows in (c) and (d).

4.3.2.3 Origin of the Phosphorus-Rich Bands

In general, high symmetry facets with a low Miller index are low in surface energy. These facets are more stable and the growth rate is normally slower than that of the high Miller index facets when grown under the same growth conditions. Therefore, the NWs are

normally bounded by {110} and {112} side facets because of their low surface energy.[26] In addition, in most cases the {112} side facets are much smaller compared with the {110} facets, which makes them easy to be overlooked. This is because the surface energy of the {112} facets is at least two times larger than that of the {110} facets.[33] During the growth, the {112} facets were growing faster than {110} facets, making them shrink to the corner. When the {112} facets get smaller, their surface chemical potential relative to the {110} facets becomes larger, due to increase in the effective curvature.[34] Therefore, the adatoms on the {112} facets will be driven by the surface chemical potential difference to diffuse away to the low chemical potential {110} facets, decreasing the growth rate of {112} facets.[24] In the end, due to balance between the influences of the surface energy and the chemical potential, the {112} facets will adopt a self-limited growth rate. During epitaxial growth with multicomponent materials, the cohesive energies (chemical bonding energy) of different elements with the substrate surface are different,[35] leading to different diffusion coefficients (diffusion length).[36] This feature can significantly influence the multicomponent shell growth. As can be seen in Fig. 4-13, phase segregation, which is rich in elements with a stronger bonding energy, is commonly observed along the <112> directions. This is due to elements with a weaker bonding energy having a longer diffusion length, making the diffusion away from the {112} facets easier when driven by the surface chemical potential difference. In the GaAsP material, P adatoms have a shorter diffusion length compared with that of As adatoms due to stronger bonding energy. [35] Therefore, during the GaAsP shell growth at the NW corners with {112} facets, more As were diffused away, leaving P-rich bands along these <112> directions.

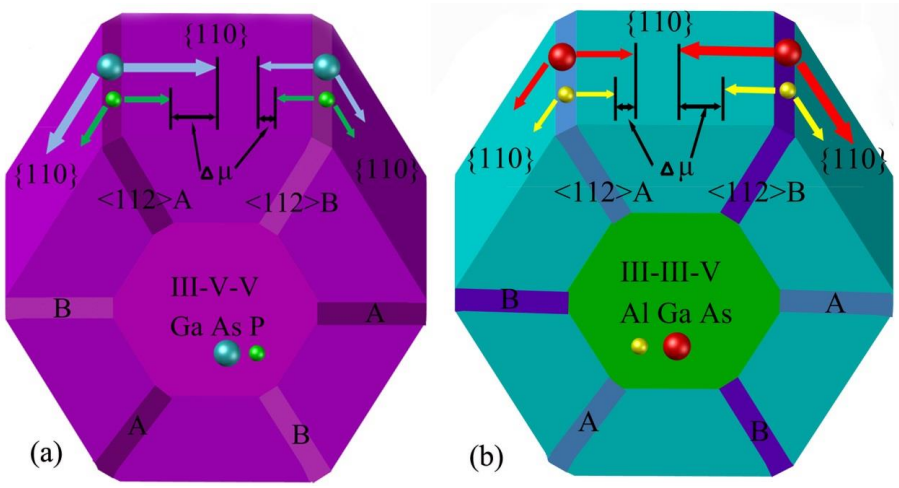

Figure 4-13. Illustrations of the phase segregation mechanism happened in the shell made of (a) III-V-V and (b) III-III-V materials.

4.3.2.4 Origin of the 3-Fold Compositional Symmetry

As presented above, the 3-fold symmetry of the P-rich bands is related to the polarities of the sidewalls. Because the core-shell NW is bounded by {110} and {112} facets and the {110} facets are non-polar and all equal, the cause of this special symmetry is attributed to the {112} facets. The surface feature differences of the {112} facets with A and B polarities are summarized in Table 4-1. In each 1×1 unit cell, the {112}A facets have two 3-fold-coordinated group-III atoms and one 2-fold-coordinated group-V surface atom, while the {112}B facets have two 3-fold-coordinated group-V atoms and one 2-fold-coordinated group-III atom.[32] Therefore, each group-V (group-III) atom incorporated into {112}A facets has two (three) new bonds, while that incorporated to the {112}B facets has three (two) new bonds.[37,38] Due to the bond number difference, the bonding energy of the group-V (group-III) atoms is much stronger at the {112}B ({112}A) facets, which makes incorporation coefficients of group-V (group-III) adatoms larger on {112}B ({112}A) facets. As a result, the

compositional phase segregation of group-V (group-III) elements is commonly observed to be stronger in <112>A (<112>B) directions. In the following paragraphs, the polarity-driven phase segregation phenomenon in III-V-V and III-III-V type of shell material growth will be described by taking GaAsP and AlGaAs as examples.

In case of our GaAsP shell growth illustrated in Fig. 4-13a, the diffusion length difference between As and P can be expressed as:

$$\triangle\mu_{AsP}=(\mu_{As}-\mu_{P}) \quad 5\text{-}1$$

where μ_{As} and μ_{P} are the diffusion lengths of As and P, respectively.

The diffused-away adatom flux difference between As and P adatoms can be expressed as:

$$\triangle n_{AsP}=(n_{As}-n_{P}) \quad 5\text{-}2$$

where n_{As} and n_{P} are the diffused-away adatom fluxes of As and P, respectively.

On the {112}B ({112}A) facets, the bonding energy of the group-V atoms is stronger (weaker), which makes $\triangle\mu_{AsP}$ smaller (larger) and hence reduces (increases) $\triangle n_{AsP}$. As a result, the element selectivity at the {112}B ({112}A) facets are weaker (stronger), which leads to lower (stronger) compositional phase segregation, making the P content of the P-rich band higher in the <112>A directions.

In the case of AlGaAs shell growth illustrated in Fig. 4-13b, the diffusion length difference between Al and Ga can be expressed as:

$$\triangle\mu_{AlGa}=(\mu_{Ga}-\mu_{Al}) \quad 5\text{-}3$$

where μ_{Ga} and μ_{Al} are the diffusion lengths of Ga and Al, respectively.

The diffused-away adatom flux difference between Ga and Al adatoms can be expressed

as:

$$\triangle n_{AlGa}=(n_{Ga}-n_{Al}) \quad 5\text{-}4$$

where n_{Ga} and n_{Al} are the diffused-away adatom fluxes of Ga and Al, respectively.

On the {112}A ({112}B) facets, the bonding energy of group-III atoms is stronger (weaker), which makes $\triangle\mu_{AlGa}$ smaller (larger) and hence reduces (increases) $\triangle n_{AlGa}$. As a result, the element selectivity at {112}A ({112}B) facets are weaker (stronger), which leads to lower (stronger) compositional phase segregation, making the Al content of Al-rich band higher in <112>B directions.

Table 4-1. Surface adatom bond information on {112} A and B facets in each 1 × 1 unit cell[32]

{112} Facet	Group-III atoms bonding site			Group-V atoms bonding site		
	Bond type	Site number	Bond strength	Bond type	Site number	Bond strength
A	3-fold-coordinated	2	Strong	2-fold-coordinated	1	Weak
B	2-fold-coordinated	1	Weak	3-fold-coordinated	2	Strong

4.3.3 Passivation of Core-Shell Nanowires

NWs have a large surface-to-volume ratio, which also means a large density of surface states.[41] Therefore, surface passivation of NWs is even more important compared with thin film structures.[41] In order to passivate the surface of NWs, a thin layer of InGaP was grown on the core-shell GaAsP NWs. From the EDX maps (Fig. 4-14), it can be found that the edge

of the core-shell structure is low in Ga and As, but high in P and In. This indicates successful InGaP passivation layer growth.

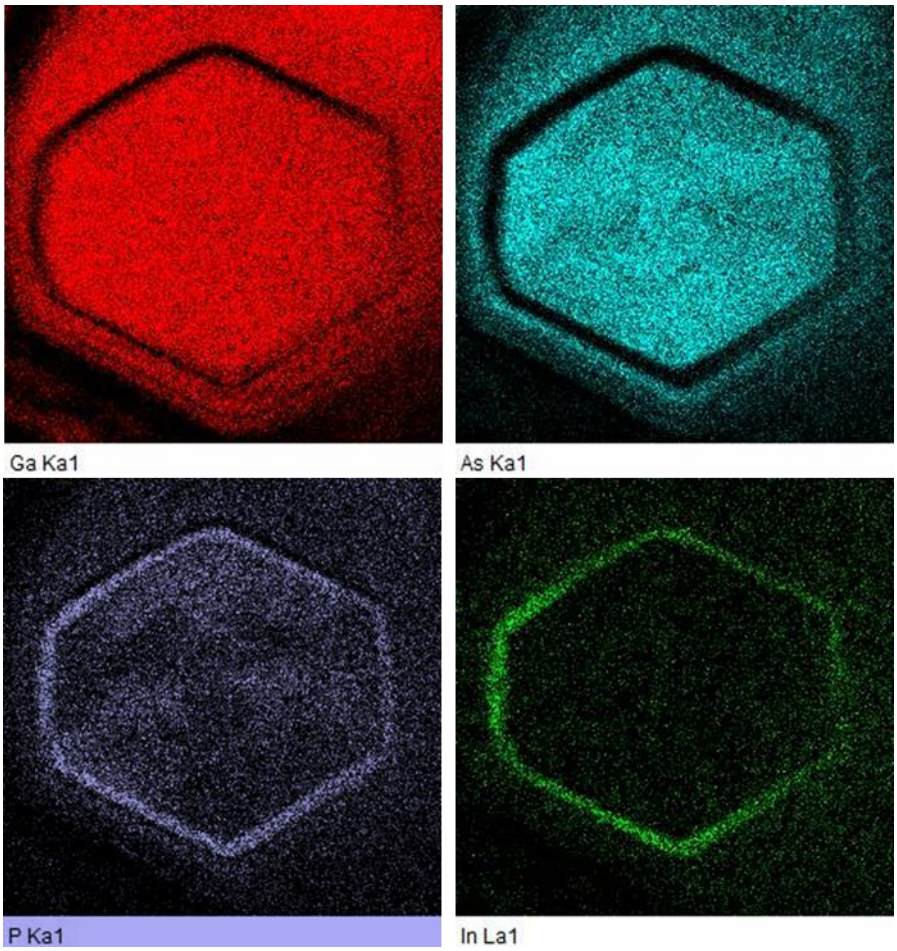

Figure 4-14. EDX maps of Ga, As, In, P in the cross section of the surface-passivated core-shell GaAsP NWs.

The optical properties of passivated and un-passivated core-shell GaAsP NWs were characterized with PL measurements. As can be seen in Fig. 4-15, the NWs show room-temperature emission with a peak-emission wavelength ~730 nm, which reveals good crystal quality of these core-shell NWs.[39,40] Therefore, the core-shell NWs fabricated by these techniques have a strong potential to be used in wide range of areas, such as photoelectrical

field. Compared with un-passivated GaAsP NWs, the passivated ones show 5 times stronger emission, which can be seen in Fig. 4-15. This indicates that the InGaP passivation layer can effectively reduce surface recombination rate.

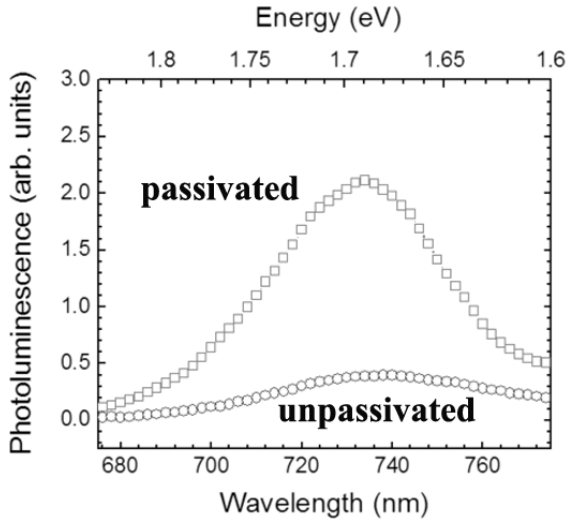

Figure 4-15. Room temperature PL spectra of passivated and un-passivated core-shell GaAsP NWs.

4.4 Conclusion

The growth of GaAsP NW shell for GaAsP NWs has been investigated in this chapter. The results suggest that slow shell growth rate is beneficial for achieving good shell morphology and crystal quality due to sufficient adatom diffusion. Good crystal quality of the core-shell NWs has been confirmed by room-temperature PL emission measurements. The compositional distribution of these core-shell structures was studied using a cross-section EDX. It is found that the curvature increase of the {112} facets can raise their surface chemical potential relative to the {110} facets. This can drive away weaker bonding elements (As) more efficiently. Hence, compositional phase segregation has been observed in the NW

shell growth with the III-V-V ternary material, GaAsP. Six P-rich bands are initiated at the outer corners of the core and extending radially along the <112> directions to the outer vertices of the shell. In addition, because the bonding energy of {112}B facets is stronger than that of the {112}A facets, the diffusion length difference between As and P is larger at the A facets. This leads to stronger phase segregation at the <112>A direction and hence higher P content. Due to alternating arrangement of the P-rich bands with high and low P content, a quasi-3-fold symmetry about the NW axis was observed in the NW cross section. Moreover, an InGaP layer was used to passivate the surface of these NWs and a four times PL intensity improvement at room temperature has been achieved when compared with the un-passivated NWs. These results provide valuable information about the NW shell growth, especially multicomponent materials shells. This theory can also be used for design and fabrication of more detailed structures inside the NW.

4.5 References

1. Caroff P, Dick K A, Johansson J, Messing M E, Deppert K and Samuelson L 2008 Nature Nanotechnology 4 50.
2. Assali S, Zardo I, Plissard S, Kriegner D, Verheijen M A, Bauer G, Meijerink A, Belabbes A, Bechstedt F, Haverkort J E M and Bakkers E P A M 2013 Nano Letters 13 1559.
3. Wilhelm C, Larrue A, Dai X and Migas, D, Soci C 2012 Nanoscale 4 1446.
4. Scofield A C, Kim S-H, Shapiro J N, Lin A, Liang B, Scherer A and Huffaker D L 2011 Nano Letters 11 5387.

5. Lopez F J, Hemesath E R and Lauhon L J 2009 Nano Letters 9 2774.
6. Parkinson P, Joyce H J, Gao Q, Tan H H, Zhang X, Zou J, Jagadish C, Herz L M and Johnston M B 2009 Nano Letters 9 3349.
7. Wallentin J, Ek M, Wallenberg L R, Samuelson L and Borgström M T 2011 Nano Letters 12 151.
8. Bao P, Wang Y, Cui X, Gao Q, Yen H, Liu H, Yeoh W K, Liao X, Du S, Tan H H, Jagadish C, Zou J, Ringer S P and Zheng R 2014 Applied Physics Letters 104 021904.
9. Wu J, Li Y, Kubota J, Domen K, Aagesen M, Ward T, Sanchez A, Beanland R, Zhang Y, Tang M, Hatch S, Seeds A and Liu H 2014 Nano Letters 14 2013.
10. LaPierre R R 2011 Journal of Applied Physics 110 014310.
11. Wu J, Zhang Y, Tutu F, Lam P, Hatch S and Liu H 2013 The Journal of the Optical Society of America RM1D-1.
12. Nguyen H P T, Zhang S, Connie A T, Kibria M G, Wang Q, Shih I and Mi Z 2013 Nano Letters 13 5437.
13. Krogstrup P, Jørgensen H I, Heiss M, Demichel O, Holm J V, Aagesen M, Nygard J and i Morral A F 2013 Nature Photonics 7 306.
14. Lauhon L J, Gudiksen M S, Wang D and Lieber C M 2002 Nature 420 57.
15. Qian F, Li Y, Gradečak S, Park H G, Dong Y, Ding Y, Wang Z L and Lieber C M 2008 Nature Materials 7 701.
16. Sköld N, Karlsson L S, Larsson M W, Pistol M E, Seifert W, Trägårdh J and Samuelson L 2005 Nano Letters 5 1943.
17. Jr Couto O D D, Sercombe D, Puebla J, Otubo L, Luxmoore I J, Sich M, Elliott T J,

Chekhovich E A, Wilson L R, Skolnick M S, Liu H Y and Tartakovskii A I 2012 Nano Letters 12 5269.

18. Xiang J, Lu W, Hu Y, Wu Y, Yan H and Lieber C M 2006 Nature 441 489.
19. Rudolph D, Funk S, Döblinger M, Morkötter S, Hertenberger S, Schweickert L, Becker J, Matich S, Bichler M, Spirkoska D, Zardo I, Finley J J, Abstreiter G and Koblmüller G 2013 Nano Letters 13 1522.
20. Jiang N, Gao Q, Parkinson P, Wong-Leung J, Mokkapati S Breuer S, Tan H H, Zheng C L, Etheridge J and Jagadish C 2013 Nano Letters 13 5135.
21. Zheng C, Wong-Leung J, Gao Q, Tan H H, Jagadish C and Etheridge J 2013 Nano Letters13 3742.
22. Fickenscher M, Shi T, Jackson H E, Smith L M, Yarrison-Rice J M, Zheng C, Miller P, Etheridge J, Wong B M, Gao Q, Deshpande S, Tan H H and Jagadish C 2013 Nano Letters 13 1016.
23. Kauko H, Zheng C L, Zhu Y, Glanvill S, Dwyer C, Munshi A M, Fimland B O, van Helvoort A T J and Etheridge J 2013 Applied Physics Letters103 232111.
24. Wagner J B, Sköld N, Reine Wallenberg L and Samuelson L 2010 Journal of Crystal Growth 312 1755.
25. Sköld N, Wagner J B, Karlsson G, Hernán T, Seifert W, Pistol M E and Samuelson L 2006 Nano Letters 6 2743.
26. Zheng C, Wong-Leung J, Gao Q, Tan H H, Jagadish C and Etheridge J 2013 Nano Letters 13 3742.
27. Guo Y N, Burgess T, Gao Q, Tan H H, Jagadish C and Zou J 2013 Nano Letters 13 5085.

28. Heiss M, Fontana Y, Gustafsson A, Wüst G, Magen C, O'Regan D D, Luo J W, Ketterer B, Conesa-Boj S, Kuhlmann A V, Houel J, Russo-Averchi E, Morante J R, Cantoni M, Marzari N, Arbiol J, Zunger A, Warburton R J and i Morral A F 2013 Nature Materials 12 439.

29. Liu H Y, Sellers I R, Badcock T J, Mowbray D J, Skolnick M S, Groom K M, Gutierrez M, Hopkinson M, Ng J S, David J P R and Beanland R 2004 Applied Physics Letters 85 704.

30. Zhang Y, Aagesen M, Holm J V, Jørgensen H I, Wu J and Liu H 2013 Nano Letters 13 3897

31. Zhang Y, Sanchez A M, Wu J, Aagesen M, Holm J, Beanland R, Ward T and Liu H 2015 Nano Letters 15 3128

32. Chadi D J J 1985 Vac. Sci. Technol., B: Microelectron. Process. Phenom. 3 1167.

33. Chadi D J 1985 Journal of Vacuum Science & Technology B 3 1167.

34. Mullins W W 1957 Journal of Applied Physics 28 333.

35. Paulus B, Fulde P and Stoll H 1996 Physical Review B 54 2556.

36. Kley A, Ruggerone P and Scheffler M 1997 Physical Review Letters 79 5278.

37. Paladugu M, Zou J, Guo Y N, Zhang X, Joyce H J, Gao Q, Tan H H, Jagadish C and Kim Y 2008 Applied Physics Letters 93 201908.

38. Zou J, Paladugu M, Wang H, Auchterlonie G J, Guo Y N, Kim Y, Gao Q, Joyce H J, Tan H H and Jagadish C 2007 Small, 3 389.

39. Couto Jr O, Sercombe D, Puebla J, Otubo L, Luxmoore I J, Sich M, Elliott T J, Chekhovich E A, Wilson L R and Skolnick M S 2012 Nano Letters 12 5269.

40. Titova L V, Hoang T B, Jackson H E, Smith L M, Yarrison-Rice J M, Kim Y, Joyce H J, Tan H H and Jagadish C 2006 Applied Physics Letters 89 173126.

41. Sun M H, Joyce H J, Gao Q, Tan H H, Jagadish C and Ning C Z 2012 Nano Letters 12 3378.

Chapter 5:

GaAsP Nanowire Growth on Patterned Si Substrates

5.1 Introduction

The NW structure has a lot of advanced properties compared with its thin film counterpart, which can provide solutions in traditional thin film epitaxial technique. Especially, the excellent strain relaxation ability can accommodate large lattice and thermal expansion mismatch. This provides a promising solution to integrate III–V materials onto the Si platform that has been pursued for more than 40 years.[1,2] Therefore great attention has been paid to the growth of III-V NWs. But most of the research is based on un-patterned substrates on which the NWs are randomly positioned due to the self-assembled growth mechanism. But for some NW applications, their positions need to be accurately controlled, such as fabricating NW photonic crystals. For example, Scofield *et al.*[3] demonstrated fabrication of GaAs/InGaAs NW photonic crystals by precisely controlling position and diameters of the NWs (Fig. 5-1). Using the NW photonic crystals, they achieved single-mode lasing at room temperature with a low threshold peak power density of~625 W/cm^2. By controlling the NW

pitch and diameter, they tuned the lasing emission from 960 to 989 nm (Fig. 5-2). These NW photonic crystal lasers can have high-Q optical cavities, small mode volume, high spontaneous emission coupling factor, and low threshold power. Therefore, they are highly desirable for photonic integrated circuits.

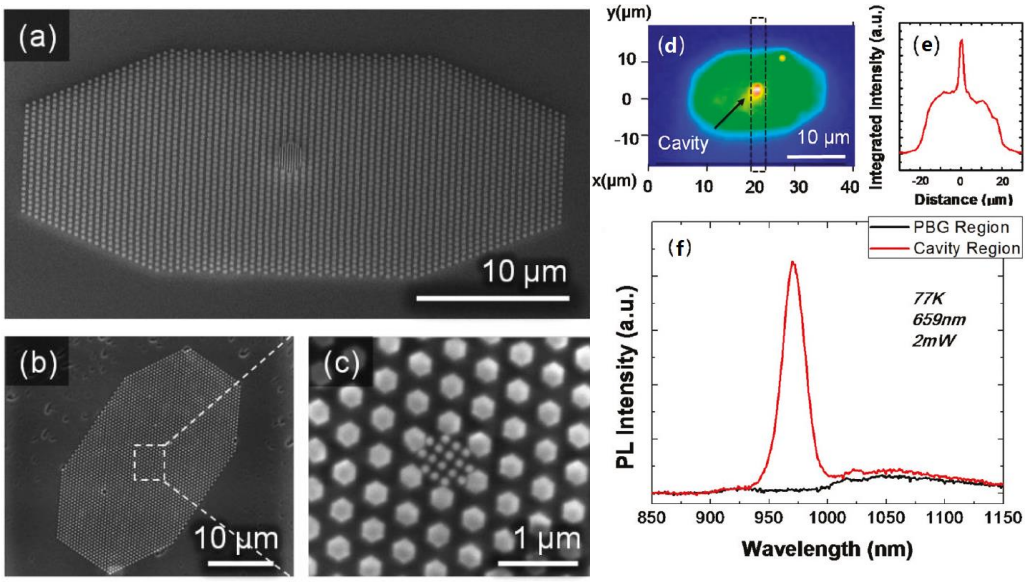

Figure 5-1 (a)~(c) SEM images of GaAs/InGaAs NW photonic crystal cavity. (d) Integrated spectrum intensity mapping of the photonic crystal device. (e) Intensity profile taken from (d). (e) Spectra of taken from cavity region and photonic band gap region. Reprinted with permission from 3. Copyright 2011 American Chemical Society.

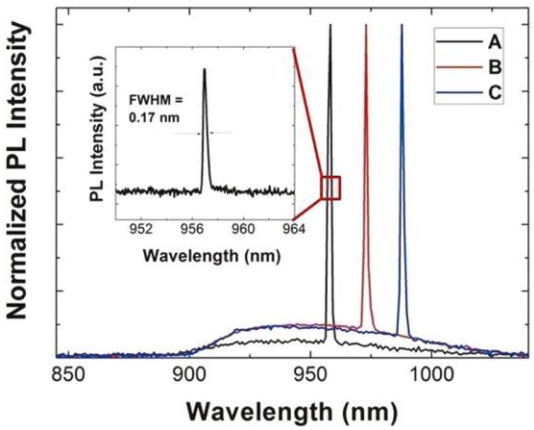

Figure 5-2 Spectra of GaAs-based NW photonic crystal lasers of different NW pitch and diameter. Reprinted with permission from 8. Copyright 2011 American Chemical Society.

For SCs patterned growth is even more important. Use of a pattern can help to improve NW uniformity, which is beneficial for achieving almost identical performance for each NW. By controlling the pitch of the patterned holes, distance between the NWs can be controlled. This can help to optimize optical absorption.[4-6] In case of multi-junction SCs, such as NW/Si double junction SC, this optical absorption adjustment is extremely useful because it can greatly facilitate current matching between junctions.[7] Moreover, because material deposition on the mask layer is not energetically favourable, the parasitic bulk (cluster) growth which often accompanies un-patterned NW growth can be suppressed. This can significantly reduce photon losses by the absorption in the clusters and hence improve the SC efficiency. During SC device fabrication, absence of clusters can facilitate material deposition/coating, making it much easier to achieve good uniformity. In SC device fabrication an insulating mask layer can also help to reduce the current leakage and hence improve performance of the device.

Due to the importance of NW position control, great attention has been paid to develop this technique. Use of dielectric material mask with specially designed pattern is the most popular method. A patterned mask can be made from SiO_x or SiN_x with nanoimprint or electron-beam lithography (EBL).[9-12] Usually the thickness of the mask is between 10~40 nm.[13,14] Dielectric mask pattern method is relatively well developed. NWs with various III-V materials have been achieved using patterned growth. However, most of them are grown homo-epitaxially on their native substrates, such as GaAs NWs on GaAs[15] substrates, InAs NWs on InAs[16] substrates and InP NWs on InP[17] substrates. In order to achieve cost reduction and integration with the Si-based technology, it is necessary to grow the NWs on patterned Si substrates. In addition, due to the advantages of the self-catalysed growth mode mentioned in

Section 1.2, it is also necessary to first develop a self-catalysed growth technique on patterned Si substrate. Therefore, great effort has been devoted to this field.[11-19] However, for quite a long period, due to some unknown reasons, patterned Si growth has been facing low-yield and low-repeatability issues.[20]

At present, most of NW research is focused on binary materials, which could be due to simpler fabrication procedures. In order to achieve larger freedom in tuning the band structure and lattice parameter, it is necessary to achieve growth of multi-element materials, such as ternary GaAsP. But growth of NWs with multi-element materials involves more than one group-III and/or group-V elements, which makes the growth mechanisms more complex and the growth parameters more difficult to be controlled. Therefore, a study of self-catalysed GaAsP NW growth on patterned Si substrate is of great importance.

In this Chapter, a self-catalysed GaAsP growth on SiO_2-patterned Si(111) substrates was developed. Presence of the Si oxide in the patterned holes was found to be one of the key factors that hinder the growth on patterned Si substrates. In order to achieve NW growth on patterned Si substrates, a high-temperature deoxidization step (HTD) and a Ga pre-deposition (GPD) step were introduced before the NW growth. With these two techniques, core-shell GaAsP NW growth on patterned Si substrates has been achieved, using the self-catalysed mode, with high yield and good repeatability.

5.2 Experiment

The substrates used in this study were Si (111), on which SiO_x mask pattern was prepared by nano-imprint lithography.[12] Before being loaded into the MBE for growth, the patterned

substrates were etched by aqueous hydrofluoric acid (HF) solution with a concentration of 5% for 2 minutes. Then, it was rinsed with deionized water for 1 minute and blow dried with nitrogen. The purpose of this was to get rid of the native oxide in the patterned holes. After these treatments, the final thickness of the mask layer was ~30 nm, which was confirmed by TEM measurements. Before being loaded into the growth chamber, the substrates were degased at 500°C for 1 hour in the buffer chamber. For the NW growth runs without the HTD step the temperature was increased directly to the growth temperature of ~630 °C. For the runs with HTD treatment, the substrates were de-oxidized at ~900 °C for 20 minutes. After that the temperature was reduced to the growth temperature of ~630 °C. During the 45 minutes NW growth , Ga flux was 1.6×10^{-7} Torr (corresponding to 0.5 ML/s); the V/III flux ratios were between 3 and 20, the P/(P+As) flux ratio was 12%.

5.3 Results and Discussion

5.3.1 Patterned Hole Cleaning by High-Temperature Deoxidization

HF is commonly used for cleaning Si surfaces, because it is widely believed that they can be passivated by H-termination after the oxide removal.[21-23] Therefore, the effects of patterned Si substrate cleaning and passivation by HF solution were studied. The Ga and group-V fluxes were opened simultaneously when growth was initiated. Fig. 5-3a, c and e were from the growths with HF solution cleaning, but without the HTD step. As can be seen, the NWs are only partially occupying the patterned holes. For the pattern with a small hole size (~85 nm), a large number of the holes are empty (5-3a). For the holes with NW growth, there is only a single NW in each hole. For holes with larger size (~185nm), all the holes are

occupied by NWs or clusters (5-3c). Besides, the NW yield is increased compared with the small hole size pattern. For holes with even larger size (0.5-1μm), there are multiple NWs in each hole. For example, in the inset in Fig. 5-3e, there are four NWs inside.

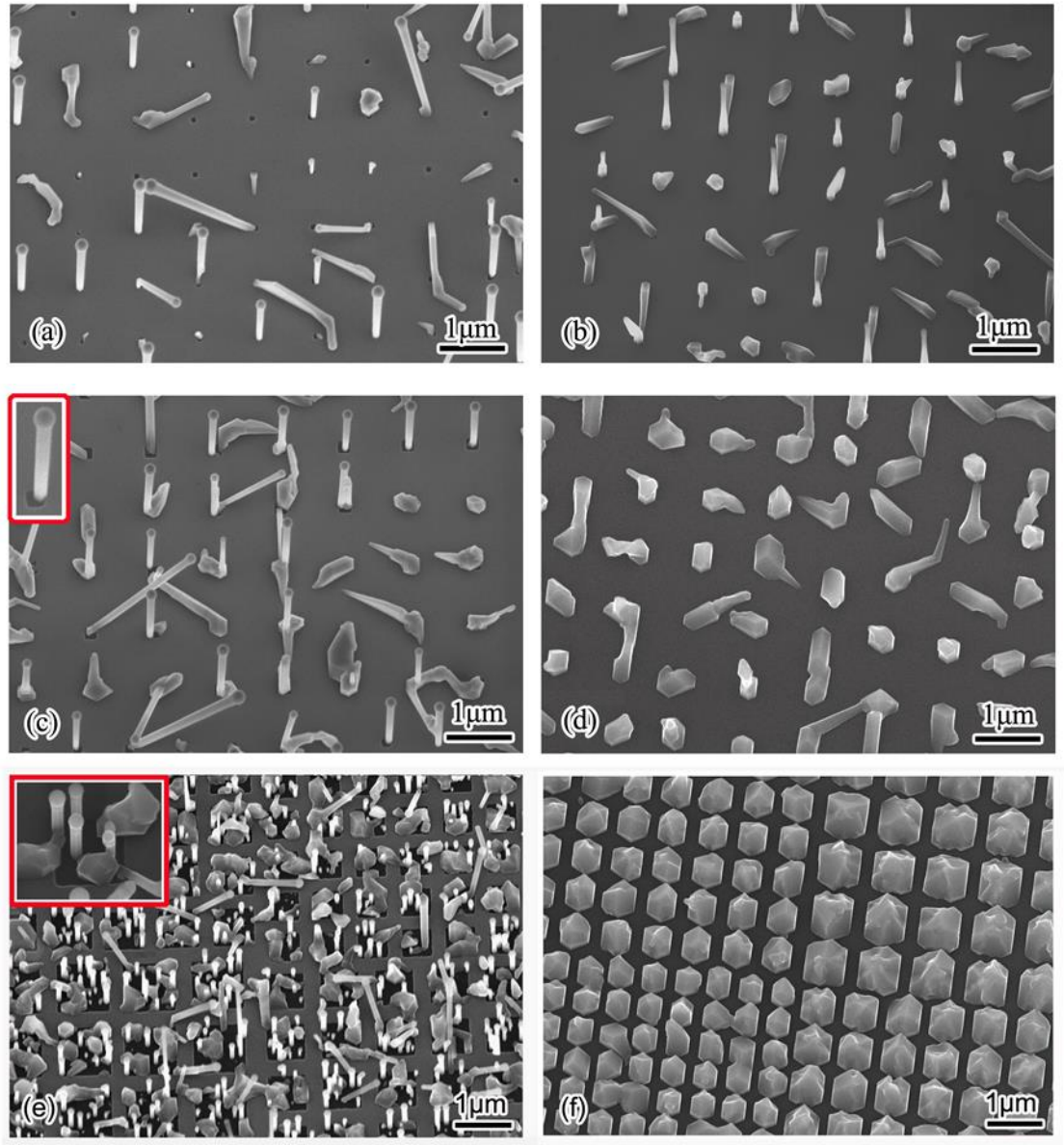

Figure 5-3. SEM images of NW growths (a), (c), (e) without and (b), (d), (f) with the HTD step. The hole size is ~85 nm for (a) (b), ~185nm for (c) (d), and 0.5~1μm for (e) (f).

These growth phenomena suggest that the patterned holes could still be covered or partially covered with native oxide and/or SiO_2 residue even after treatment with HF solution.

In order to clarify this point, the HTD step was introduced right prior to the NW growth. All other operations were kept the same for better comparison. The results are shown in Fig. 5-3b, d and f. As can be seen, all the patterned holes are completely occupied by clusters (not partially occupied), apart from some small-sized patterned holes, which have achieved the NW growth (Fig. 5-3b).

The stark contrast between growths with and without the HTD step strongly suggests that native oxide and/or SiO_2 residue remained after the HF etching. The differences between these two types of growth can be explained by the illustrations shown in Fig. 5-4. If the patterned hole is fully covered by a thin layer of oxide, it should not have NW growth. That should be why some of the patterned holes in Fig. 5-3a are empty. However, if the patterned hole size is large, there can be some pinholes inside, through which Si lattice can be exposed (Fig. 5-4a). Therefore, the oxide layer in the patterned holes can prevent too fast Ga consumption and hence allow Ga adatoms to accumulate at the pinhole sites to form droplets (Fig. 5-4b).[25,26] Because the pinholes can reach the Si lattice, this can provide a template for the NW growth (Fig. 5-4c). The number of pinholes in the patterned holes will increase with patterned-hole size. That should be why the NW number is limited to one or none when the size is small (Fig. 5-3a and b), whereas multiple NWs can grow in the large holes (Fig. 5-3c). Because material deposition on the oxide layer is inhibited, only the pinhole locations have material growth, so that the patterned holes are only partially covered, as shown in Fig. 5-3c and e. For the growths with HTD treatment, the oxide inside the patterned holes can be thoroughly removed. The effectiveness of the HTD step can be further confirmed by deoxidization of the patterned substrate at a temperature higher than that normally used. As

shown in Fig. 5-5, the SiO_2 pattern can even be damaged if the HTD temperature is too high. Therefore, right HTD temperature can make the patterned holes fully open (Fig. 5-4d and e), which leads to complete filling of patterned holes with the III-V material deposition (Fig.5-3b, d, and e). When the patterned hole size is small, the nucleation area is small even if it is fully opened by the HTD step. Because of this, the slow Ga consumption rate inside the holes can allow a significant amount of Ga atoms to accumulate into the droplets and catalyse the NW growth. That is why the NW growth is still available in these holes shown in Fig. 5-3b. But if the hole size is large, the nucleation area inside is large when it is fully opened, which leads to fast Ga adatom consumption rate. As a result, the Ga droplet formation is suppressed and only vapour-solid cluster growth is available inside the holes (Fig. 5-3d and e, Fig. 5-4e and f).

The model shown in Fig. 5-4 strongly suggests that the holes patterned on the Si substrates are not oxide free after only the HF solution cleaning. Successful NW growth in Fig. 5-3a, c and e is an indication of the presence of an oxide layer. Existence of the oxide layer inside the patterned holes could be the reason why the yield and repeatability are always low for the patterned Si growth. This model is also supported by the fact that the yield and repeatability are much higher when grown on patterned III-V substrates, such as GaAs NWs on GaAs[15] substrates, InAs NWs on InAs[16] substrates and InP NWs on InP[17] substrates. The native oxides of the III-V substrates have much lower deoxidization temperature, which makes it much easier to clean the pattern compared with that of the patterned Si substrates.

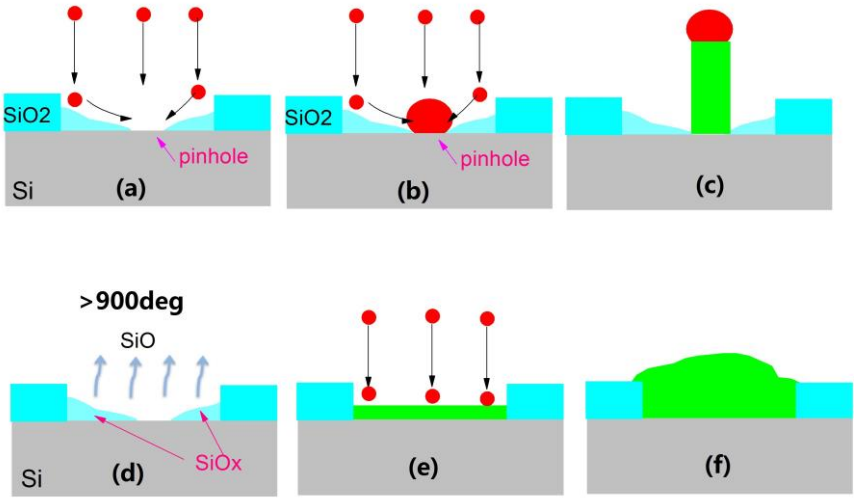

Figure 5-4. Illustration of the growth (a)~(c) without and (d)~(f) with HTD step.

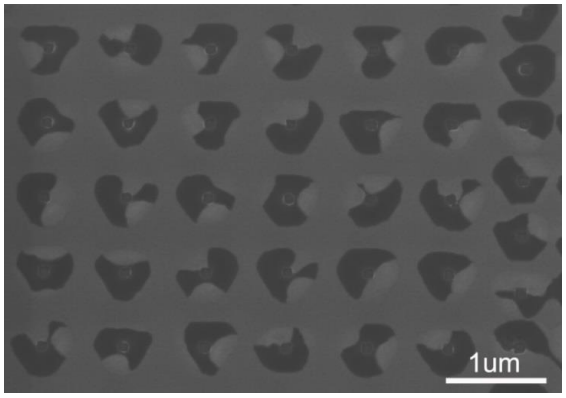

Figure 5-5. SEM image of the patterned substrate with HTD of higher temperature.

5.3.2 Ga Pre-Deposition

As indicated above, fully-opened patterned holes have a large nucleation area, which can suppress Ga droplet formation due to fast Ga atom consumption rate. But in order to achieve the VLS NW growth, droplet formation is critical. To assist the Ga droplet formation, a Ga pre-deposition (GPD) step at a Ga flux of 1.6×10^{-7} Torr for 1 minute was added after the HTD but before the introduction of the group-V fluxes for the NW growth. As can be seen in Fig.5-6, successful NW growth has been achieved on the HTD-cleaned patterns with different hole sizes, which demonstrates effectiveness of the GPD step.

5.3.3 Influence of the Patterned Hole Size

As can be seen in Fig. 5-6, morphology of the NWs is quite different if they are grown out of patterns with different hole sizes. When the patterned hole size is small (~50 nm), the NWs have uniform morphology without visible parasitic growth on the sidewalls (Fig. 5-6a). Increasing the hole size to ~75 nm, parasitic growth at the bottom of the NW can be observed (Fig. 5-6b). Further increasing the hole size to ~135 nm, parasitic crystal growth was greatly enhanced, giving the NWs a wider base and stunted length (Fig. 5-6c). As summarized in Fig.5-6d, the NW length decreases with the increase of base diameter. This demonstrates that the parasitic crystal growth has a competitive effect with the NW growth.

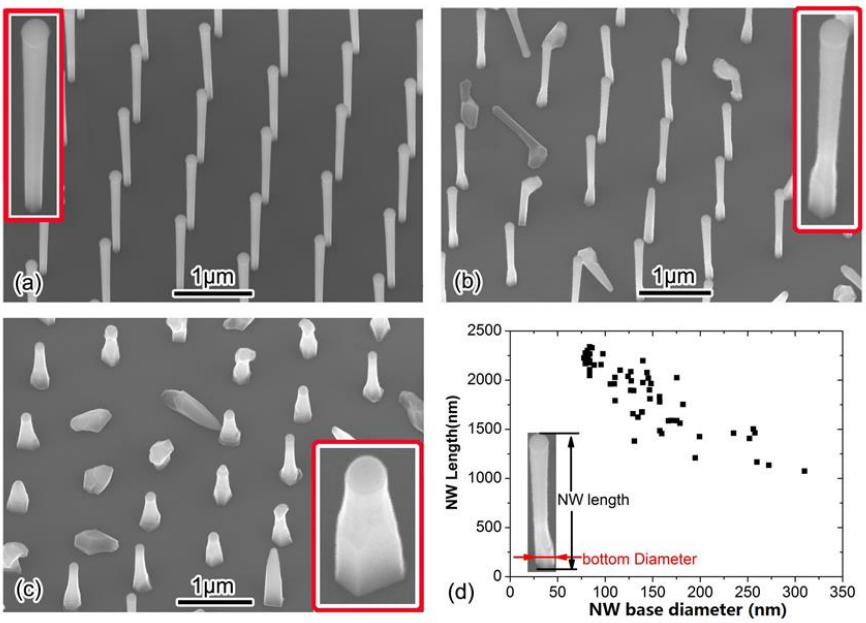

Figure 5-6. SEM images (tilt angle = 25°) of NWs grown on the patterns with a hole size of (a) ~50 nm, (b) ~75 nm, and (c) ~135 nm. (d) NW length as a function of NW base diameter.

The influence of the patterned hole size on the NW morphology could be explained by the model illustrated in Fig. 5-7. In this model, the relative size difference between the catalyst droplet and the patterned hole is the key factor. During the first stage, a Ga droplet

forms in the patterned holes, which subsequently initiates VLS growth of the NWs. For the patterns used in Fig. 5-6, there is only one droplet in each patterned hole, because the Ga adatom diffusion length is larger than the hole size at the growth temperature. If the hole size is small, it can be completely covered by the catalyst droplet (case A of stage 1 in Fig. 5-7). But for the patterned holes with a diameter (r) larger than the droplet size, some of the Si region is not occupied by the droplet, which is referred to as "vacant oxide-free area" (case B and C of stage 1 in Fig. 5-7).

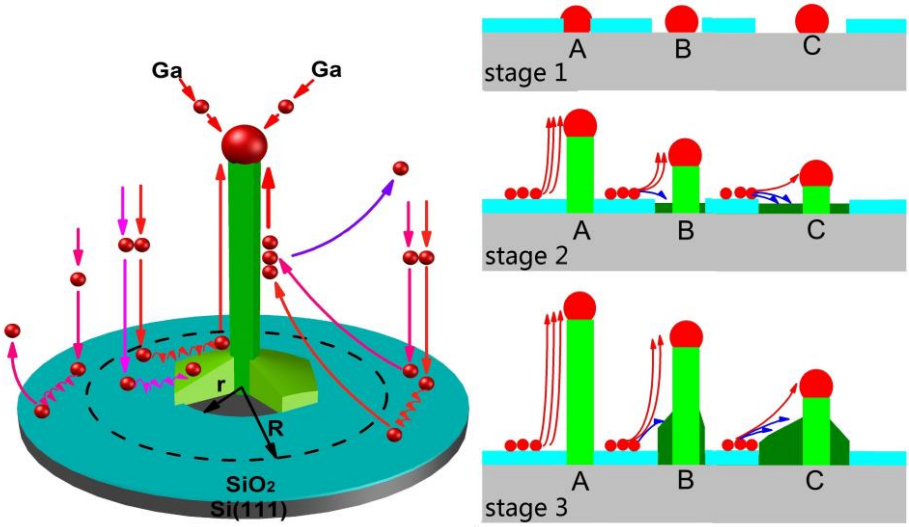

Figure 5-7. Illustration of three stages of NWs growth on patterned substrates with holes of different sizes. The three stages are: stage 1, Ga droplet formation before NW growth; stage 2, at beginning of the NW growth; stage 3, after a long period of NW growth. The hole size in (A) is equal to or less than, (B) slightly greater than, and (C) much larger than the catalytic droplet size in stage 1.

After the HTD and GPD steps, both group-III and group-V fluxes were introduced to start the NW growth. For the pattern with hole sizes comparable or smaller than that of the droplet, all Ga adatoms within the collection radius, R, are diffusing to the Ga droplet, which can provide abundant Ga replenishment for the droplet and sustain the VLS growth (Fig. 5-6a and case A in Fig. 5-7). If the hole size is slightly larger than that of the Ga droplet, things are

different. Due to presence of vacant oxide-free Si area in the hole, not all Ga adatoms are diffused to the droplet. Some of them are deposited in the vacant oxide-free area through VS growth mode. Therefore, the vacant oxide-free area can consume part of the Ga adatoms, which can reduce Ga replenishment for the droplet and hence reduce the NW length. With the NW growth proceeding, the VS epitaxial growth, started at the vacant oxide-free area, grows along the NW length and forms low energy side facets (Fig. 5-6b and case B in Fig. 5-7). If the patterned hole is very large, the vacant oxide-free area is large as well. As a result, most of Ga adatoms are consumed by the VS epitaxial growth in the vacant oxide-free area, leading to a large NW base (Fig. 5-6c and case C in Fig. 5-7). Besides, due to the significantly reduced Ga replenishment for the droplet, the NW length is greatly reduced (Fig. 5-6c and case C in Fig. 5-7). The relationship between the NW length and its base diameter is summarized in Fig. 5-6d, which shows clear decrease of the NW length with increase of the NW base diameter.

5.3.4 Nanowire Shell Growth

The shell growth on the patterned-grown NWs is critical for achieving their advanced functions, such as lateral junctions and lateral quantum wells. In order to achieve shell growth on the core NW, the Ga droplet was consumed by closing the Ga shutter with the group-V fluxes open. This operation is critical for terminating axial growth as indicated in Section 1.2. The shell growth lasted for 1 hour at a substrate temperature of ~485 °C, Ga flux of 1.6×10^{-7} Torr, a V/III flux ratio of 60 and a P/(P+As) flux ratio of 30%. The patterned-grown core-shell GaAsP NWs are shown in Fig. 5-8a. These NWs have uniform morphology with smooth sidewalls. But the tip of the NW is irregular, which is due to an un-optimized Ga droplet

consumption. The core-shell composition match can be achieved with the assistance of X-ray diffraction (XRD). As shown in Fig. 5-8a, the core-shell NWs in Fig. 5-8a have a single-peak in the XRD spectrum, the angle of which is in close proximity of that of the core NW shown in Fig. 5-6a. This is a strong indication of core-shell composition match. The optical properties of these core-shell NWs were studied by PL measurements with a 635 nm diode-pumped solid-state laser. Fig. 5-8c shows the PL spectrum obtained at room temperature with an excitation power of 500 mW/cm^2. Strong emission intensity indicates good crystal quality of the core-shell NWs arrays. The peak emission is at ~740 nm, which is highly promising for application in photovoltaics, visible emitters, and photonic crystals.

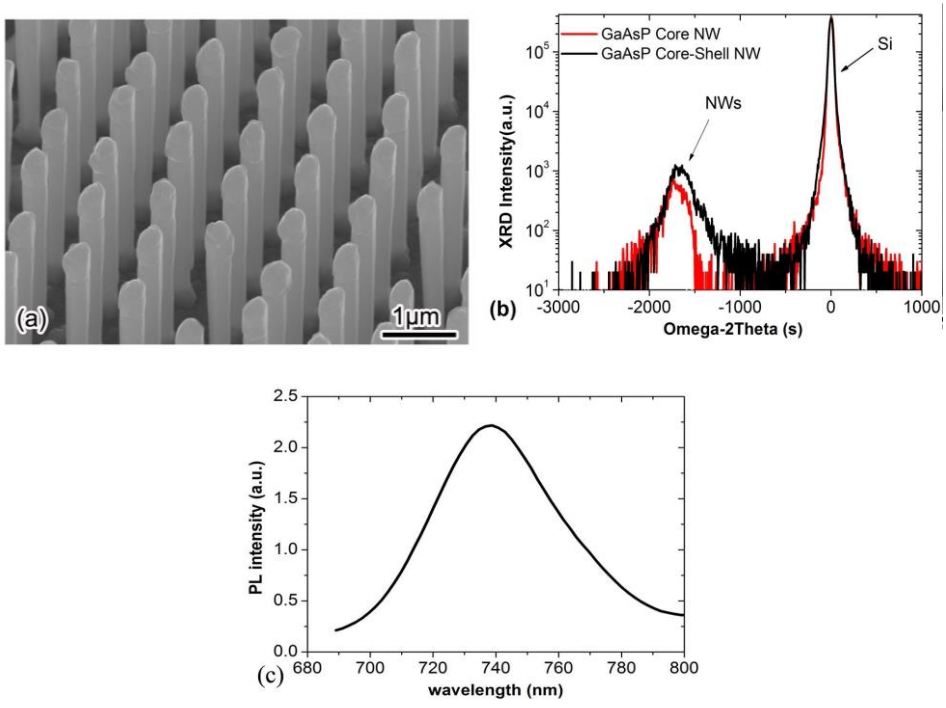

Figure 5-8. (a) SEM image of the high-yield core-shell GaAsP NW arrays grown on patterned Si substrates (25° tilted), (b) GaAsP NWs core and shell composition check by X-ray diffraction, and (c) PL spectrum of the core-shell GaAsP NW arrays measured at room-temperature.

5.3.5 Nanowire/Substrate Interface Properties

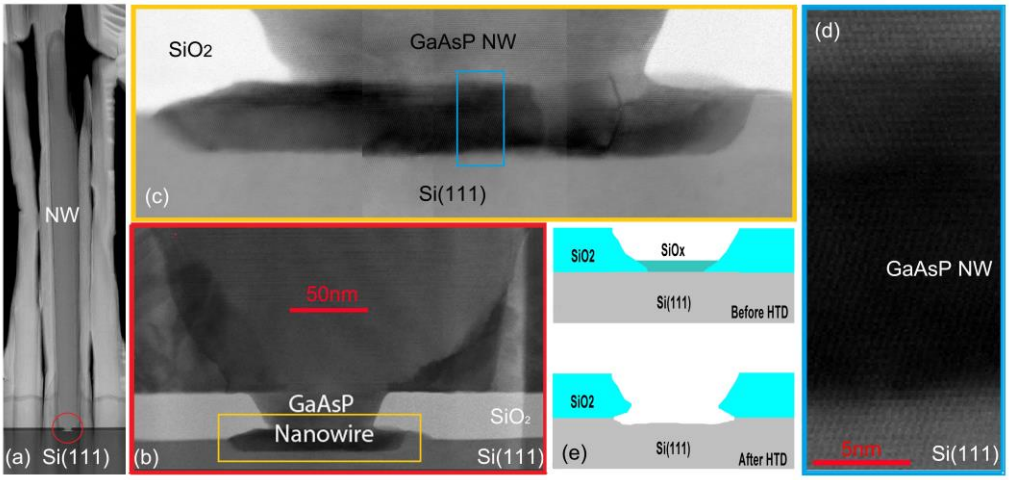

Figure 5-9. TEM image of (a) a whole core-shell NW, (b) (c) the interface between the NW and the Si substrate highlighted by the red circle in (a). (d) High-resolution TEM image that shows the interface area highlighted by the blue box in (c). (e) Illustration of the high-temperature desorption of oxide.

In order to check the NW/substrate interface quality of NWs grown with the technique described in this Chapter, TEM measurements were performed and the results are presented in Fig. 5-9. The NW is standing vertically in a patterned hole (Fig. 5-9a and b), the base of which is sunk into the Si substrate and wedged laterally into the SiO_2 mask/Si substrate interface. Lattice connection between the NW base and the Si substrate clearly shows that the interface is oxide-free. The interesting phenomenon shown in Fig. 5-9 could be due to the mechanism illustrated in Fig. 5-9e. During pattern cleaning by the HTD treatment, the oxide in the patterned holes evaporated. High temperature can also trigger a reaction between the Si and the SiO_2, the product of which is SiO that is much easier to evaporate than SiO_2 at this temperature. Therefore, the Si/SiO_2 reaction started at the pinhole sites in the patterned holes and extended laterally along the Si/SiO_2 interface. With long enough HTD treatment time, the

reaction can drill a large empty space below the pattern mask at the pattern/substrate interface. During the NW growth, this wedged empty space was filled by GaAsP. Therefore, this phenomenon strongly confirmed the effectiveness of pattern cleaning by the HTD treatment.

5.4 Conclusion

The high-yield and repeatable NW growth on patterned Si substrates has been demonstrated with self-catalysed MBE-grown GaAsP NWs. Chemical etching with HF solution was found not to be able to guarantee the cleanness of the holes on the patterned Si substrates. The presence of oxide inside the patterned holes is suggested to be the main reason for low yield and repeatability. Introduction of an in-situ high-temperature deoxidization step (~900 ^{o}C) was found to be highly effective to clean the patterned holes. In order to achieve VLS NW growth in the thoroughly cleaned patterned holes, a Ga pre-deposition step was demonstrated to be essential, because it assists catalytic droplet formation. The patterned hole size was also shown to be able to significantly affect the NW morphology. Based on this observation, it is suggested that the catalytic droplet size should be comparable or larger than the patterned hole size when doing the patterned growth with the VLS mode. Moreover, a lattice matched shell was grown on the patterned core NWs and demonstrated room-temperature PL emission, which reveals good crystal quality and indicates their potential for applications. These results solved the long-term issue of integrating III-V NWs onto patterned Si substrates via self-catalysed VLS growth mode, which paves the way for further development of Si-substrate-based III-V NW technique.

5.5 References

1. Mathine D L 1997 Selected Topics in Quantum Electronics, IEEE Journal of 3 952.
2. Roelkens G, Liu L, Liang D, Jones R, Fang A, Koch B, Bowers J 2010 Laser Photonics Review 4 751.
3. Scofield A C, Shapiro J N, Lin A, Williams A D, Wong P S, Liang B L and Huffaker D L 2011 Nano Letters 11 2242
4. Lin C and Povinelli M L 2009 Optical Express 17 19371.
5. Heiss M, Russo-Averchi E, Dalmau-Mallorquí A, Tütüncüoğlu G, Matteini F, Rüffer D, Conesa-Boj S, Demichel O, Alarcon-Lladó E and Fontcuberta i Morral A 2014 Nanotechnology 25 014015.
6. Kelzenberg M D, Boettcher S W, Petykiewicz J A, Turner-Evans D B, Putnam M C, Warren E L, Spurgeon J M, Briggs RM, Lewis N S and Atwater H A 2010 Nature Material 9 239
7. Wu P M, Anttu N, Xu H, Samuelson L and Pistol M-E 2012 Nano Letters 12 1990
8. Scofield A C, Kim S-H, Shapiro J N, Lin A, Liang B, Scherer A and Huffaker D L 2011 Nano Letters 11 5387.
9. Dick K A 2008 Progress in Crystal Growth and Characterization of Materials 54 138
10. Bauer B, Rudolph A, Soda M, i Morral A F, Zweck J, Schuh D and Reiger E 2010 Nanotechnology 21 435601
11. Conesa-Boj S, Kriegner D, Han X-L, Plissard S, Wallart X, Stangl J, Fontcuberta i Morral A and Caroff P 2014 Nano Letters 14 326
12. Munshi A M, Dheeraj D L, Fauske V T, Kim D-C, Huh J, Reinertsen J F, Ahtapodov L,

Lee K, Heidari B, Van Helvoort A, Fimland B O, and Weman H 2014 Nano Letters 14 960

13. Heurlin M, Hultin O, Storm K, Lindgren D, Borgstrom M T and Samuelson L 2014 Nano Letters 14 749
14. Plissard S, Larrieu G, Wallart X and Caroff P 2011 Nanotechnology 22 275602
15. Yao M, Huang N, Cong S, Chi C Y, Seyedi M A, Lin Y T and Zhou C 2014 Nano Letters 14 3293
16. Anttu N, Lehmann S, Storm K, Dick K A, Samuelson L, Wu P M and Pistol M E 2014 Nano Letters 14 5650
17. Heurlin M, Stankevič T, Mickevičius S, Yngman S, Lindgren D, Mikkelsen A and Samuelson L 2015 Nano Letters 15 2462
18. Plissard S, Dick K A, Larrieu G, Godey S, Addad A, Wallart X and Caroff P 2010 Nanotechnology 21 385602.
19. Gibson S J, Boulanger J P and LaPierre R R 2013 Semiconductor Science and Technology 28 105025.
20. Heiss M, Russo-Averchi E, Dalmau-Mallorquí A, Tütüncüoğlu G, Matteini F, Rüffer D, Conesa-Boj S, Demichel O, Alarcon-Lladó E and Fontcuberta i Morral A 2014 Nanotechnology 25 014015.
21. Morita Y, Miki K and Tokumoto H 1991 Applied Physics Letters 59 1347.
22. Higashi G S, Chabal Y J, Trucks G W and Raghavachari K 1990 Applied Physics Letters 56 656.
23. Ma D D D, Lee C S, Au F C K, Tong S Y and Lee S T. 2003 Science 299 1874.

24. Zhang Y, Wu J, Aagesen M, Holm J, Hatch S, Tang M, Huo S and Liu H 2014 Nano Letters 14 4542.

25. Ambrosini S, Fanetti M, Grillo V, Franciosi A and Rubini S. 2011 Journal of Applied Physics 109 094306.

26. Ambrosini S, Fanetti M, Grillo V, Franciosi A and Rubini S. 2011 AIP Advances, 1 042142.

Chapter 6:

Conclusions and Future Work

6.1 Introduction

In this Chapter, the major contributions of this thesis toward the development of self-catalysed GaAsP NWs are summarized. However, these results are far from enough to bring NWs into practical applications. More work is needed for which some suggestions are made in this Chapter.

6.2 Summary and Conclusions

In this thesis self-catalysed GaAsP NWs grown on Si substrate have been investigated by using solid source MBE.

Due to the VLS growth mode with Ga rich environment, the incorporation coefficient of P was found to be almost three times as much as that of As. Introduction of P into the growth can greatly increase nucleation rate, making the NW growth more complex. Although the growth temperature window could be smaller than 10°C, GaAsP NWs with good diameter uniformity along the NW length have been achieved over a large growth rate range by

controlling the V/III flux ratio. These NWs have almost defect-free ZB crystal structure. By controlling the P/As flux ratio, the P content in the NW can be controlled between 10% and 75%, which can cover a large range of bandgaps. Because of the VLS growth mode, Be concentration can gradually build up in the droplet during the NW growth. This can lead to change of the droplet surface energy and hence sidewall wetting of the droplet. Eventually, the VLS NW growth will cease. After the NW growth, a low-temperature Ga droplet consumption process was demonstrated to be able to reduce refilling of the Ga droplet and produce flat tips with smooth sidewalls. In addition, NW uniformity control has been achieved for the first time in self-catalysed growth by changing the chemical potential of the vapour phase (V/III flux ratio). Length deviation ranging from 5% to 22% has been demonstrated.

In order to construct more advanced NW structures for better device performance and satisfy some special requirements, growth of GaAsP shell on the core NWs was subsequently studied. NWs with good core-shell morphology and crystal quality have been achieved with a slow shell growth rate. In the cross-section of these ternary core-shell structures, compositional phase segregation was observed in form of six P-rich bands along the <112> directions. Three of them along the <112>A directions are found to be higher in P content compared with other three along the <112>B directions, forming a quasi-3-fold composition symmetry. A model involving sidewall surface chemical potential and polarity-related adatom bonding energies was proposed and successfully applied to explain this special phenomenon. By passivating these core-shell NWs with a layer of InGaP, a four-time PL intensity enhancement has been demonstrated.

The research then proceeded to SiO_2-patterned Si(111) substrates. Self-catalysed GaAsP core-shell NW growths have been achieved with high yield and good repeatability, which solved the long-term issue of low-yield and low-repeatability on patterned Si substrates. From this research, presence of Si oxide in the patterned holes was found to be one of the key factors that create obstacles for growth on patterned Si substrates. In order to achieve the NW growth, it is necessary to introduce a high-temperature deoxidization step before the NW growth to clean the pattern and then a Ga pre-deposition step to assist the catalyst droplet formation. In addition, the results also suggest that the catalytic droplet size should be comparable or larger than the patterned hole size when doing patterned growth with the VLS growth mode. Otherwise, parasitic VS growth on the base of NWs can significantly affect the NW growth.

The discoveries here not only open up new perspectives for research on the GaAsP core-shell NW devices on both un-patterned and patterned Si substrates, but also provide valuable information for development of other III-V NWs, especially those made of multi-element materials.

6.3 Future Work

Despite fast development, a lot of challenges are still present in the NW area. At present, the performance of NW devices is still lagging far behind the traditional thin film counterparts. For example, the highest NW SC efficiency is only about 13.8%.[1] In order to bring NWs into practical applications, the following obstacles need to be solved.

The doping is in urgent need to be studied. Core doping is completely different from thin

film growth.[2] The NW is following the VLS growth mechanism, making doping much more difficult.[2] Especially, as presented in Chapter 3, the doping can affect the NW growth, making the NW growth more complex. Shell doping needs to be investigated as well. Although shell growth follows the same VS growth mode as traditional thin film growth, the growth condition is much more difficult to control due to the 1-D substrate (core NWs).[3] Besides, the NW has a nanometre-sized 1-D columnar structure, making the device requirement for doping quite different from the thin film structure. Therefore, a comprehensive study of the NW core and shell doping is necessary to obtain NWs with good electrical properties.

The NW has a large density of surface states, which can act as a highly efficient non-recombination centre and degrade device performance.[4] Surface passivation is much more important compared with thin film devices. The highly-efficient long-standing surface passivation technique is still lacking. Besides, depending on the device application, different environment can add some other difficulties for the passivation. As mentioned in Section 1.5.1, the InGaP passivation of GaAsP NWs is efficient for SC,[5] but not sufficient for water splitting devices.[6] Therefore, the application-based surface passivation techniques are needed to guarantee good device performance.

The NW device design theories are quite different from thin film devices, such as requirement for layer thickness, composition and doping concentration. Therefore, great effort is needed to adapt the thin film device design theories for NW devices. In addition, the NW structure can bring a lot of novel advantages compared with the thin film structure. For example, axial material stacking can fabricate QDs without assistance of strain.[7] Application of these advantages can revolutionise present technologies.

The special 1-D NWs structure with nanometre-scale diameter makes device fabrication more difficult. For example, the NW array devices are facing shunting paths issue connecting the front electrode on top of the NWs and the rear electrode[8]. A layer of isolation medium between the NWs can prevent this issue. However, isolation medium filling is difficult, especially between NWs with long length. Use of inorganic filling materials, such as SiO_2, tend to deposit conformally, which can create voids in the filling layers and lead to delamination.[9] Spin coating with organic materials, such as polystyrene, can cause bundling of NWs due to capillary forces.[10] In some cases, fillings such as SC200 and SU8 can be successful.[11] But the subsequent treatment, such as post-deposition annealing can lead to severe cracking and delamination.[11] Therefore, the filling material and filling method need to be developed.

In addition, many of the bulk device processing methods need to be adapted, because of the small volume, tiny cross section, and large surface-to-volume ratio of NWs.

Due to large surface states density and small size, NW is much easier to be depleted. This can cause significant difficulties in ohmic contact formation. When a metal contacts with a semiconductor material, such as indium tin oxide with GaAs, the charge traps at semiconductor/metal interface can induce Fermi level pinning near midgap and cause formation of Schottky barrier as well as surface depletion in the semiconductor.[13] In bulk material contact fabrication, a layer of heavily doped material is commonly used as a contact layer to overcome these Schottky barriers, because increase in doping density can reduce the depletion width and enhance carrier tunnelling process. In case of NWs, the small dimension requires higher doping density for the contact layer compared with thin film structures.[14]

Otherwise, the depletion width will extend across the whole cross-section of the NW and will make it very difficult to establish proper band bending for carrier tunneling.[14] This issue can lead to a rapid increase in contact resistance as the NW diameter is reduced.[14] Therefore, the contact layer needs to be studied.

Also due to the small size, contact annealing procedure is more difficult to control. The diffusion length of the metals in III-V materials can be of the order of 100 nm during annealing.[13,15] Therefore, unoptimised annealing conditions can cause diffusion of contact materials across the entire diameter of a nanowire, introducing defective trap states and hence degrading performance of the device.[13,15] This issue is especially critical for sidewall contact structures. As a result, the NW contact fabrication process needs to be controlled to avoid damaging NW devices by contact material diffusion. In addition, the NW device structure needs to be designed to prevent the contact material diffusion.

6.4 References

1. Wallentin J, Anttu N, Asoli D, Huffman M, Åberg I, Magnusson M H, Siefer G, Fuss-Kailuweit P, Dimroth F and Witzigmann B 2013 Science 339 1057
2. Casadei A, Krogstrup P, Heiss M, Röhr J A, Colombo C, Ruelle T, Upadhyay S, Sørensen C B, Nygård J, i Morral A F 2013 Applied Physics Letters 102 013117.
3. Zhang Y, Aagesen M, Holm J V, Jørgensen H I, Wu J and Liu H 2013 Nano Letters 13 3897
4. Sun M H, Joyce H J, Gao Q, Tan H H, Jagadish C, Ning, C Z 2012 Nano Letters 12 3378

5. Holm J V, Jørgensen H I, Krogstrup P, Nygård J, Liu H and Aagesen M 2013 Nature communications 4 1498

6. Wu J, Li Y, Kubota J, Domen K, Aagesen M, Ward T, Sanchez A, Beanland R, Zhang Y and Tang M 2014 Nano Letters 14 2013

7. Heiss M, Fontana Y, Gustafsson A, Wüst G, Magen C, O'Regan, D D, Luo J W, Ketterer B, Conesa-Boj S, Kuhlmann A V, Houel J, Russo-Averchi E, Morante J R, Cantoni M, Marzari N, Arbiol J, Zunger A, Warburton R J, i Morral A F 2013 Nature Materials 12 439.

8. Tsakalakos L, Balch J, Fronheiser J, Korevaar B, Sulima O and Rand J 2007 Applied Physics Letters 91 233117

9. Latu-Romain E, Gilet P, Noel P, Garcia J, Ferret P, Rosina M, Feuillet G, Levy F and Chelnokov A 2008 Nanotechnology 19 345304

10. Xu C, Wang X and Wang Z L 2009 Journal of the American Chemical Society 131 5866

11. Chia A C E and LaPierre R R 2011 Nanotechnology 22 245304.

12. Stelzner T, Pietsch M, Andra G, Falk F, Ose E and Christiansen S 2008 Nanotechnology 19 295203

13. Kim T J and Holloway P H 1977 Critical Reviews in Solid State and Materials Sciences 22 239.

14. Léonard F and Talin A A 2011 Nature nanotechnology 6 773.

15. Lapierre R R 2011 Journal of Applied Physics 109 034311.